

AD-A156 079

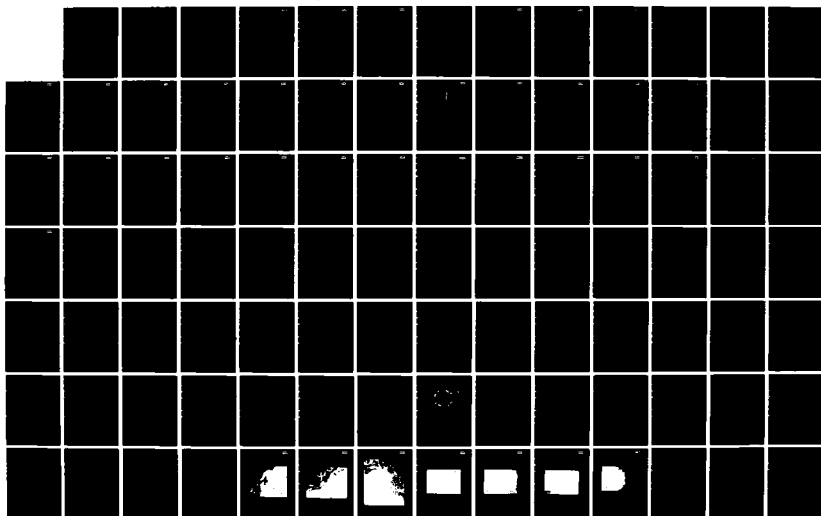
HGCDTE SURFACE AND DEFECT STUDY PROGRAM(U) SANTA
BARBARA RESEARCH CENTER GOLETA CALIF J A WILSON ET AL.
01 JUL 84 RPT50220 MDA903-83-C-0108

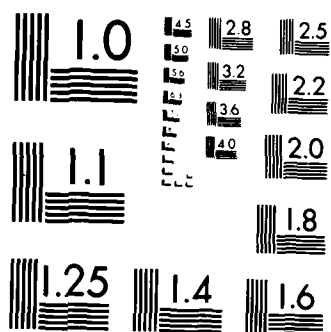
1/2

UNCLASSIFIED

F/G 20/12

NL





MICROCOPY RESOLUTION TEST CHART
NATIONAL BUREAU OF STANDARDS-1963-A

AD-A156 079

2

HgCdTe SURFACE AND DEFECT STUDY PROGRAM

V.A Cotton and J. A. Wilson
Santa Barbara Research Center
Goleta, CA 93117

J. A. Silberman, G. Carey, A. B. Chen, C. Shih
D. J. Friedman, I. Lindau, and W. E. Spicer
Stanford Electronics Laboratories
Stanford, CA 94305

A. Sher
SRI International
Menlo Park, CA

R. G. Wilson
Hughes Research Laboratories
Malibu, CA

July 1984

THIRD INTERIM TECHNICAL REPORT

CONTRACT No. MDA-903-83-C-0108

The views, opinions, and findings contained in this report are those of the authors and should not be construed as an official Department of Defense position, policy, or decision, unless so designated by other official documentation

Prepared for:

DARPA
1400 Wilson Blvd.
Arlington, Virginia 22209
Attention: Dr. Richard A. Reynolds
Defense Systems Office

JUN 27 1985

A

DTIC FILE COPY

85 6 10 012

UNCLASSIFIED

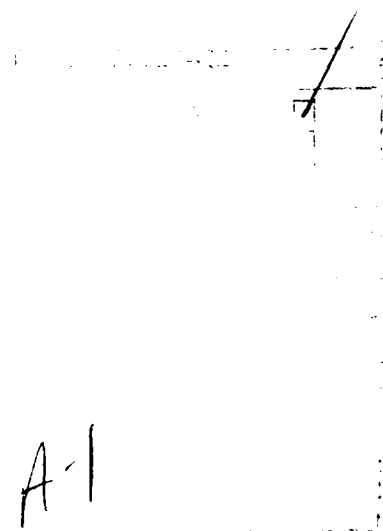
SECURITY CLASSIFICATION OF THIS PAGE

REPORT DOCUMENTATION PAGE

1a. REPORT SECURITY CLASSIFICATION UNCLASSIFIED			1b. RESTRICTIVE MARKINGS		
2a. SECURITY CLASSIFICATION AUTHORITY DARPA			3. DISTRIBUTION/AVAILABILITY OF REPORT Approved for Public Release Distribution is Unlimited (A)		
2b. DECLASSIFICATION/DOWNGRADING SCHEDULE					
4. PERFORMING ORGANIZATION REPORT NUMBER(S) RPT50220			5. MONITORING ORGANIZATION REPORT NUMBER(S)		
6a. NAME OF PERFORMING ORGANIZATION Santa Barbara Research Center		6b. OFFICE SYMBOL (If applicable)	7a. NAME OF MONITORING ORGANIZATION		
6c. ADDRESS (City, State and ZIP Code) 75 Coromar Drive Goleta, CA 93117			7b. ADDRESS (City, State and ZIP Code)		
8a. NAME OF FUNDING/SPONSORING ORGANIZATION DARPA		8b. OFFICE SYMBOL (If applicable)	9. PROCUREMENT INSTRUMENT IDENTIFICATION NUMBER MDA-903-83-C-108		
8c. ADDRESS (City, State and ZIP Code) 1400 Wilson Blvd. Arlington, CA 22209			10. SOURCE OF FUNDING NOS.		
11. TITLE (Include Security Classification) HgCdTe Surface and Defect Study Program			PROGRAM ELEMENT NO.	PROJECT NO.	TASK NO.
12. PERSONAL AUTHOR(S) J.A. Wilson, V.A. Cotton, J.A. Silberman, G.P. Carey, C.K. Shih, (cont. on reverse)			WORK UNIT NO.		
13a. TYPE OF REPORT Interim Technical		13b. TIME COVERED FROM 1/84 TO 7/84	14. DATE OF REPORT (Yr., Mo., Day) 840701		15. PAGE COUNT 160
16. SUPPLEMENTARY NOTATION					
17. COSATI CODES			18. SUBJECT TERMS (Continue on reverse if necessary and identify by block number)		
FIELD	GROUP	SUB. GR.			
			HgCdTe, HgTe, CdTe, II-VI alloys, photoemission spectroscopy, surfaces, defects, electronic structure, interface		
19. ABSTRACT (Continue on reverse if necessary and identify by block number)					
<p>This report presents program results for the six-month period ending July 1, 1984. The results presented include determination of the sources of charge at the Photox™/HgCdTe interface; measurement and comparison of atomic concentration vs. depth and electrical activity due to nuclear stopping for random and channeled implants using SIMS and C-V techniques respectively; evaluation of changes in bulk trapping levels near the processing altered interface by DLTS; identification and evaluation of new trap levels introduced by implantation damage by DLTS; measurement of surface band structure; continued bond length calculations; results of TEM examination of the CdTe/HgCdTe interface; and finally calculations of dislocation energy and hardness.</p>					
20. DISTRIBUTION/AVAILABILITY OF ABSTRACT UNCLASSIFIED/UNLIMITED <input type="checkbox"/> SAME AS RPT <input type="checkbox"/> NOTIC USERS <input type="checkbox"/>			21. ABSTRACT SECURITY CLASSIFICATION		
22a. NAME OF RESPONSIBLE INDIVIDUAL			22b. TELEPHONE NUMBER (Include Area Code)		22c. OFFICE SYMBOL

CONTENTS

<u>Section</u>	<u>Page</u>
SUMMARY.....	iv
INTRODUCTION.....	1
I INTERFACE STUDY.....	5
II CHANNLED IMPLANTS.....	31
III SURFACE STUDY.....	37
IV ALLOY BONDING.....	105
ACKNOWLEDGEMENTS.....	153



A-1



Summary

Previously reported studies of the HgCdTe/Photox[™] SiO₂ interface on MIS devices have shown that the net charge of this interface depends on pre-passivation surface treatments, water content and surface fermi energy. Studies in this report have predicted that the charge contribution due to interface traps will be different for n and p type material and demonstrated this effect on both diodes and MIS devices. Admittance spectroscopy and quasistatic C-V measurements have shown the slow state contribution to charge to be due to states communicating with the oxide in the 10⁻² Hz range. Charge instability of the interface was demonstrated to be due to charge injection in contrast to mobile ions as in the Si/SiO₂ system. Capacitance-voltage measurements at low temperature have revealed a discreteness of inversion layer formation or trap levels. Pre-passivation surface treatments have a serious impact on interface traps as well as bulk trap characteristics. Polished and etched surfaces have shown a redistribution of a mid-gap bulk trap level as seen by deep level transient spectroscopy. The concentration of this trap will strongly affect G-R current and diode RoA.

The implantation task has shown that electrical activity due to implant damage follows the random portion of the atomic profile, but raised an order of magnitude, for both random and channeled samples of B, P and Cl. Channeled hydrogen shows distinctly n type damage but with no direct correlation to the channeled profile obtained from SIMS. Damage in randomly implanted samples was found to create a weakly repulsive trap at $\approx E_c - 0.20$ eV ($E_g = 0.27$ eV) with a large barrier height. The concentration of this trap scales linearly with the implant species concentration. Continuing use of angle resolved photoemission spectroscopy to observe the surface and bulk electronic band structure has been applied to samples with X=1.0, 0.31, 0.23 and 0.00. The dispersion and polarization dependences seen are similar to those for CdTe. There is some divergence of theory and data but the general agreement validates the assumption of a nearly free electron final state.

Calculations showing unusual bond length relaxation characteristics of HgCdTe predict a weak HgTe bond which leads to the mechanical instability of the lattice. This simple radial force model agrees with the trend predicted by Mikkelsen and Boyce for InAs-GaAs. The effects of this unusual bonding

behavior on the thermodynamics and kinetics of interfaces has been studied. Ion milling of HgCdTe LPE heterojunctions resulted in HgCdTe exhibiting a more metallic-type recovery than CdTe. This results in lower defect densities and narrower stacking faults. This also supports the theoretical predictions of a weakened HgTe bond and ease of Hg vacancy formation.

Soft x-ray photoemission spectroscopy was used to monitor the kinetics of activated oxygen uptake on the cleaved (110) face. The oxides grown were composed of Cd and Te oxides. Hg was shown to be lost from the surface during the initial stages of oxide formation but no Hg was found in the final oxide. Monitoring of the growth rate on samples of various x-values showed the growth of the first two monolayers to scale with the number of Hg-Te bonds.

Using an extension of Harrison's method, dislocation energies per unit length were calculated to be proportional to d^{-3} to d^{-9} and hardness proportional to d^{-5} to d^{-11} where d is the bond length. These calculations are confirmed by experiment. Hardness was found to be related to the interaction energies among dislocations. It is proposed that an alloy with a second constituent of a shorter bond length will improve crystal strength. Experimental verification of this has been seen on GaP in GaAs and 4% Zn in CdTe. Calculations show the already weak HgTe bond to be further destabilized by adjacent CdTe, HgS or HgSe but to be stabilized by ZnTe. This leads to the conclusion that HgZnTe will have a structural advantage over HgCdTe.

(This Page Intentionally Left Blank)

Introduction

This report summarizes results obtained on the study of the HgCdTe surface for the six-month period ending July 1, 1984. The purpose of the study is to develop a microscopic picture of the surface and near surface regions of HgCdTe, particularly the defect structure, which play a direct role in the surface passivation of IR detectors.

Successful passivation of detectors, particularly photovoltaics, is of critical importance for the smaller size elements found in large, high-performance arrays. Here the volume to surface area ratio has decreased sufficiently so that it is no longer adequate to optimize bulk junction parameters to achieve high performance. Phenomena determined by the surface properties come to completely limit device operation. These effects are not predictable from bulk diode modeling and it is now necessary to design and model surface properties in conjunction with bulk properties. These surface properties cannot be inferred from bulk properties but must be measured separately in a system which incorporates the passivation to be used.

The effectiveness of HgCdTe passivation with Photox™ SiO₂ has been shown to depend most strongly on the interface charge.¹ Under the right conditions, this charge can induce significant leakage current at the surface in a region that would otherwise be depleted of carriers, effectively shunting the bulk junction R₀A. The effects of interface charge on the surface of an n⁺ on p junction is schematically represented in Figure 1. The transition from n to p type and hence the junction is represented by the vertical solid lines with the depletion region limits for reverse bias shown by the dashed lines. The p side depletion region is wider since this is the lower doped side. This figure illustrates in (a), that for net positive interface charge the p side is depleted at the surface while the n side is accumulated; and (b), for net negative charge the p side is accumulated while the n side is now depleted. For the large difference in doping from n⁺ to p sides as is common for implanted junctions, for example, the depletion region on the n⁺ side is very much narrower so that when this side is accumulated the effective decrease in the surface junction depletion width is insignificant in comparison to accumulating the p side. Pinching off the depletion region at the surface for negative net interface charge, in this case, can increase the surface trap tunneling, in the presence of appropriate surface states. This simplest and

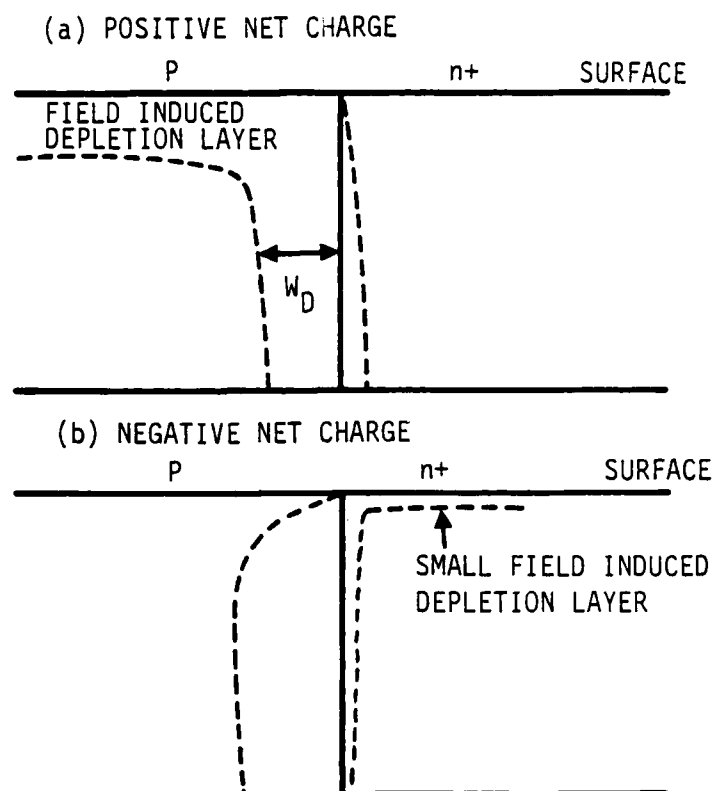


Figure 1. Schematic illustration of the effects of interface charge on surface of n^+p junction.

straightforward scenario does appear to be a significant mechanism of surface leakage in many MWIR double layer heterojunction (DLHJ) devices. There are however many complications on this once we consider implanted junctions, LWIR devices or even the more complicated barrier junctions which are produced.

Since net interface charge is contributed to by fixed insulator charge and charged interface states in about equal proportion, it is not at all accurate to model surface leakage based on the same charge affecting both the n and p sides. The surface Fermi energy, E_{fs} , is different at n and p interfaces so that interface traps are filled to different levels resulting in different interface trap charge components. The actual value of E_{fs} is, of course, affected by the field induced junction and therefore must be determined in a self-consistent manner accounting for the value of Q_{it} , rather than being assumed from the bulk value of E_f . In general the interface trap contributions are expected to be negative on the n side and positive on the p side.

The passivated surface region can be further complicated by surface processes which may alter the composition at the surface to a different x -value or produce a non-stoichiometric region by depletion of Hg and/or Cd. This of course will affect atomic or crystal bonding (and therefore interface state density) as well as doping density and band gap. These latter also have a direct effect on E_{fs} . Surface damage due to processing is of fundamental importance to HgCdTe because of the low binding energy of Hg in the alloy.² This has motivated the fundamental studies of alloy hardness and bonding discussed in Section IV.

It is also of course necessary that the passivation layer be a good insulator; have good adhesion and be chemically inert. These latter properties are not considered in this study since, although practically important, they are not the principal determinant of surface electronic structure.

To characterize the structure of the interface region with respect to charge distribution, electronic states, and crystal defects, the study (and this report) are divided into four principal tasks: (1) electronic structure of the passivated interface (Photox[™] SiO₂ on HgCdTe); (2) surface and bulk defects at interfaces with ion implanted HgCdTe; (3) electronic structure of the bare surface (cleaved in vacuum) as well as its oxidation chemistry; and (4) theoretical modeling of the defect structure of HgCdTe, particularly the Hg vacancy, its activation energy, and energy levels.

(This Page Intentionally Left Blank)

Section I

Interface Study

This section presents results of the continuing characterization of the passivated HgCdTe interface. The effort is focused on studying the interface charge, interface trap structure, and alteration of the bulk structure at the surface by pre-passivation processing.

The net charge affecting the state of the surface has three contributors which are each distinctly important due to the difference in their response times to changes in applied gate bias. These are: (1) fixed charge (Q_{fix}) in the insulator which does not respond to bias changes; (2) slow states (Q_{slow}) which are viewed as oxide traps communicating with the interface and which respond on the order of 1 Hz or less; and (3) interface trap charge which responds very quickly. These charges sum to give the net interface charge which determines whether the passivated surface is accumulated, depleted or inverted.

The "fixed" charge contribution is due to the work function difference between the applied gate metal and the HgCdTe substrate in addition to immobile ions in the oxide. These ions arise either during formation of the Photox™ layer or by diffusion after the layer is deposited. The Photox™ SiO₂ used as a passivation on HgCdTe is inherently porous and permits diffusion of ions in to the oxide. Fast diffusing metals, such as indium, have been seen to alter the amount of fixed charge as well as the effective dielectric constant of the layer. Titanium is commonly used for gates in our devices because it does not show such diffusion, and hence does not contribute to fixed charge.

Net charge of the HgCdTe/SiO₂ system has been found to be localized in a layer at the interface.¹ Water, arising from the deposition or from later absorption of atmospheric water, has been shown to have a large impact on this charge.³ Water is a natural by-product of the silane-nitrous oxide reaction used to obtain SiO₂. The amount of water (and SiOH and SiH) created will depend on deposition parameters such as temperature, gas flow rates, and gas mixture ratios. In a study to determine the location of charge in the system it was found that less charge was present in samples which had 1500 Å of SiO₂ deposited in 500Å increments, as opposed to a single deposition. In this case the incrementally deposited sample sees a fifteen minute 100°C bake between

layers which may minimize water content. It is also expected that the "interface" between SiO_2 layers will act as a barrier preventing diffusion of water to the interface. In the case of absorption of water from the atmosphere, possible surface states are created at 0.06 eV and 0.14 eV which have been seen to contribute up to 0.08V to flat band bias measure by C-V. This water does not appear to make any fixed charge contribution since the surface potential shift occurs abruptly as the surface states are seen. Water affects the interface charge through the trap charge component.

At interfaces where D_{it} is large enough that trap charge is a significant contributor to net interface charge it is expected that the interface charge will be different at similar interfaces with either n or p type HgCdTe. The density of interface traps, seen as a U-shaped distribution in the semiconductor band gap with C-V techniques, is believed to be made up primarily of scattering induced tailing of valence and conduction band states into the band gap. This is illustrated in Figure 2 where an experimentally determined distribution (solid line) is shown with the band tailing contributions necessary to produce the distribution. States arising from conduction band tailing are most likely acceptor like and those from the valence band donor like. (This was incorrectly reversed in the previous interim report). Recall that acceptor like states are neutral when empty and negative when filled while donor like over are neutral when filled and positive when empty. These states are filled according to Fermi-dirac statistics so that the expected total trap charge, from those two types of states in a symmetrical distribution, is negative at an n type interface and positive at a p type interface. (This result was correctly stated in the previous report). The drop-off of D_{it} in Figure 3 near each band edge is not real but an artifact of the measurement technique.

EXPERIMENT

Wafers of $\text{Hg}_{0.7}\text{Cd}_{0.3}\text{Te}$ were cut from ingots grown by the horizontal zone melt technique. These wafers are slightly polycrystalline and of random orientation. Isothermal annealing in Hg vapor at 250°C gave n-type material with $N_D - N_A \sim 7 \times 10^{14} \text{ cm}^{-3}$. Capacitors were then fabricated by deposition of 1500\AA of PHOTOXTM SiO_2 and thermal evaporation of 400\AA of Ti, followed by 4000\AA of Au. The metals were delineated by use of a shadow mask during evaporation. An indium contact soldered to the HgCdTe provided the ground.

High frequency (1 MHz) capacitance-voltage measurements at 80K (the mid-range of temperature scanned by DLTS) provided information on flatband voltage, depletion width and accumulation voltage needed to select DLTS measurement biases. The values measured were: flatband voltage of $+0.1\text{V} \pm 0.05\text{V}$, $N_D - N_A = 7 \times 10^{14} \text{ cm}^{-3} \pm 3 \times 10^{14} \text{ cm}^{-3}$, depending on the individual device, and a maximum depletion width of $\sim 1.0 \mu\text{m}$. Thus $+1.0$ or $+0.5\text{V}$ was sufficient to accumulate the surface and fill traps and -3 volts or more would create the maximum depletion region width.

DLTS was then used to probe trap activation energies and response times. Measurements were taken with a signal frequency of 10 MHz, 50 mV amplitude and fill pulse duration of 1 ms. Peaks were observed over a range at temperatures between 15K and 200K. Fill pulse and measurement pulse heights were varied between $+1.0\text{V}$ and -4.0V in 0.25 to 1.0V increments to profile the depletion region (maximum width $\sim 1.0 \mu\text{m}$).

The trap emission rate (e) is given by:

$$e = 1/\tau \text{ where } \tau = (t_1 - t_2)/\ln(t_1 - t_2)$$

in which t_1 and t_2 are the sampling times measured from the end of the fill pulse. Arrhenius plots of e versus $1000/T$ yield then the activation energy, E_{DLTS} .

INTRODUCTION

Electron and hole traps in HgCdTe have been of interest due to their effect on generation-recombination rates and the attendant adverse impact on lifetime (and, therefore, device performance). Work has been done to characterize these traps for p-type $\text{Hg}_{1-x}\text{Cd}_x\text{Te}$ for various x-values.¹ Two hole traps were seen which possibly correlate with the mercury vacancy levels. Electron capture characteristics of this trap have also been evaluated,² as well as theoretical and empirical investigation of this trap's effect on diode performance.³

To date, work in HgCdTe has focused on trap levels in the bulk of the material. However, it has been seen that defect formation at the surface, particularly compositionally significant cation removal, is unavoidably associated with the chemical and mechanical treatments used in surface preparation.⁴ This can cause a significant variation in electronic properties, including trap activation energies, capture cross sections, and populations between the material surface and the bulk. There is also the possibility that shallow level traps in the bulk may become deeper states at the interface (as proposed by Allen, Buisson, and Dow⁵) thus creating surface states with a unique activation energy but due to the same impurity. It is important, then, from the point of view of device surface passivation, to examine traps near the material surface. Surface state populations and activation energies have been characterized on the Si/SiO₂ interface⁶⁻⁹ with constant capacitance DLTS; however, this has not previously been done on the on HgCdTe/SiO₂ interface.

This work investigates for the first time electron traps near the HgCdTe/SiO₂ interface using DLTS on n-type $\text{Hg}_{0.7}\text{Cd}_{0.3}\text{Te}$ MIS structures in the temperature range from 15K to 200K. Three states were found and characterized, providing activation energy, capture cross section, and depth profile information.

Appendix A

Section I

DEEP ELECTRON TRAPS NEAR THE PASSIVATED
INTERFACE OF HgCdTe*

V. A. Cotton, J. A. Wilson, and C. E. Jones

Santa Barbara Research Center

Goleta, CA 93117

ABSTRACT

Electron traps in bulk n-type $\text{Hg}_{0.7}\text{Cd}_{0.3}\text{Te}$ were investigated near the $\text{HgCdTe}/\text{SiO}_2$ interface by use of deep level transient spectroscopy (DLTS) on Metal-Insulator-Semiconductor (MIS) structures [D.V. Lang, J. Appl. Phys., 3022 (1974)]. Three electron traps are found with activation energies (relative to the conduction band edge) of 0.12, 0.172 and 0.079 eV, and corresponding capture cross sections of 3.5×10^{-18} , 1.1×10^{-16} , and $1.2 \times 10^{-18} \text{ cm}^2$. Depth profiles from the surface to $\sim 1.0 \text{ } \mu\text{m}$ show the concentration of the 0.172 eV trap to be uniform while the 0.12 eV trap shows a strong depth dependence. It is undetectable at the surface, rising in concentration to twice its bulk value at $\sim 0.5 \text{ } \mu\text{m}$ depth then falling to a value comparable with that of the 0.172 eV trap in the bulk ($1 \text{ } \mu\text{m}$). Divalent trapping behavior has also been detected. In this case, the deeper state significantly depopulates, enabling a shallower state to then depopulate [J.S. Blakemore, Semiconductor Statistics 156 (1962), Pergamon Press, London].

* Supported by DARPA contract MDA-903-83-C-0108.

"ideal" quasistatic curve (solid line) to obtain the D_{it} distribution of Figure 12. The inversion side of the measured quasistatic is widened compared to the ideal resulting in higher values from -0.10V to -0.17V of surface potential. It is not possible from this measurement to discriminate between real interface states and charge nonuniformities. Admittance spectroscopy (discussed earlier) and deep level transient spectroscopy (DLTS) are not usually affected by these nonuniformities due to their observation of a specific response time. When nonuniformities are a factor in admittance measurements it is easily discernable from other effects.

DLTS is additionally valuable as a tool for fully characterizing trapping sites (activation energy capture, cross section, and trap concentration) and profiling their distribution in energy and concentration with depth into the material. This has also been used to evaluate how bulk properties are altered in the region of a processed surface or interface. Results of this preliminary DLTS study are discussed in Appendix I to this Section.

References:

1. Proceedings 1984 MCT Workshop, Journal of Vacuum Science and Technology A, Vol. 3, No. 1, p. 199
2. Microelectronics-Applications, Materials and Technology, Vol. 3
3. 'Effects of H_2O on the $SiO_2/HgCdTe$ Interface' to be published, Journal of Applied Physics, March 15, 1985
4. Proceedings 1983 MCT Workshop, Journal of Vac. Science and Technology A, Vol. 1, No. 3, p. 1719

only in ramping from accumulation to inversion, however, and a very interesting effect is seen as we monitor the opposing ramp with temperature. As we begin our observation at 7K, there is a wide depletion dip within which there are two very distinct peaks. As we increase temperature these peaks become less pronounced, the depletion dip is narrowed and deepened and by the time we reach 90 to 100K we have only the familiar single dip representing a well behaved quasistatic curve. Among the possible causes for this phenomena are discrete inversion layer energy levels. More detailed analysis is underway.

An important consideration in all of the C-V measurements discussed is the effect of charge nonuniformities on the device parameters thus extracted, most notably on effective interface trap density (D_{it}). When these nonuniformities occur with distribution lengths on the order of a depletion region width ($<1\mu m$) of the MIS device measured, which in our case has an area of $2 \times 10^{-3} cm^2$, the device will behave equivalently to many smaller capacitors in parallel each with a slightly different V_{FB} . This will cause the transition into depletion to be dispersed along the voltage axis and lead to an incorrectly high determination of interface trap density. The dotted lines in Figure 12 are actual quasistatic and 1 MHz data which are compared to a calculated

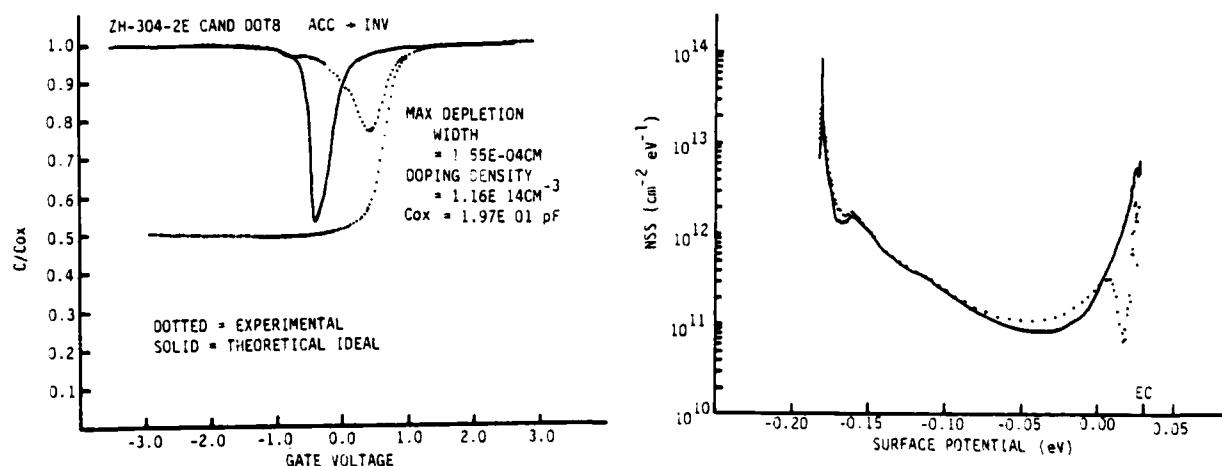


Figure 12. Effect of surface potential nonuniformities on (a) quasistatic C-V and (b) Calculated D_{it}

depletion) and in some of these cases the polarity of hysteresis is changed for one of the steps. The strong flatband shift is caused by charge injection into the oxide and much of this charge is mobile as witnessed by the increased hysteresis. A tentative explanation for the steps into depletion is that charge is now available to fill and empty previously unoccupied oxide states farther from the interface. This could also account for the occasional shift in hysteresis polarity by contributing mobile ions (or charges) to the oxide.

Monitoring C-V characteristics versus temperature produced results that are still being analyzed, however some preliminary conclusions can be drawn. Figure 11 shows a 1 MHz C-V curve taken at 77K and quasistatic C-V curves taken at four temperatures on a fairly good quality MIS structure ($D_{it} = 1 \times 10^{11} \text{ cm}^{-2}$ at 80K). At the lower temperatures (<40K) we see the widened depletion dip and the inversion spike indicative of the nonequilibrium measurement of an interface dominated by slow insulator traps. This occurs

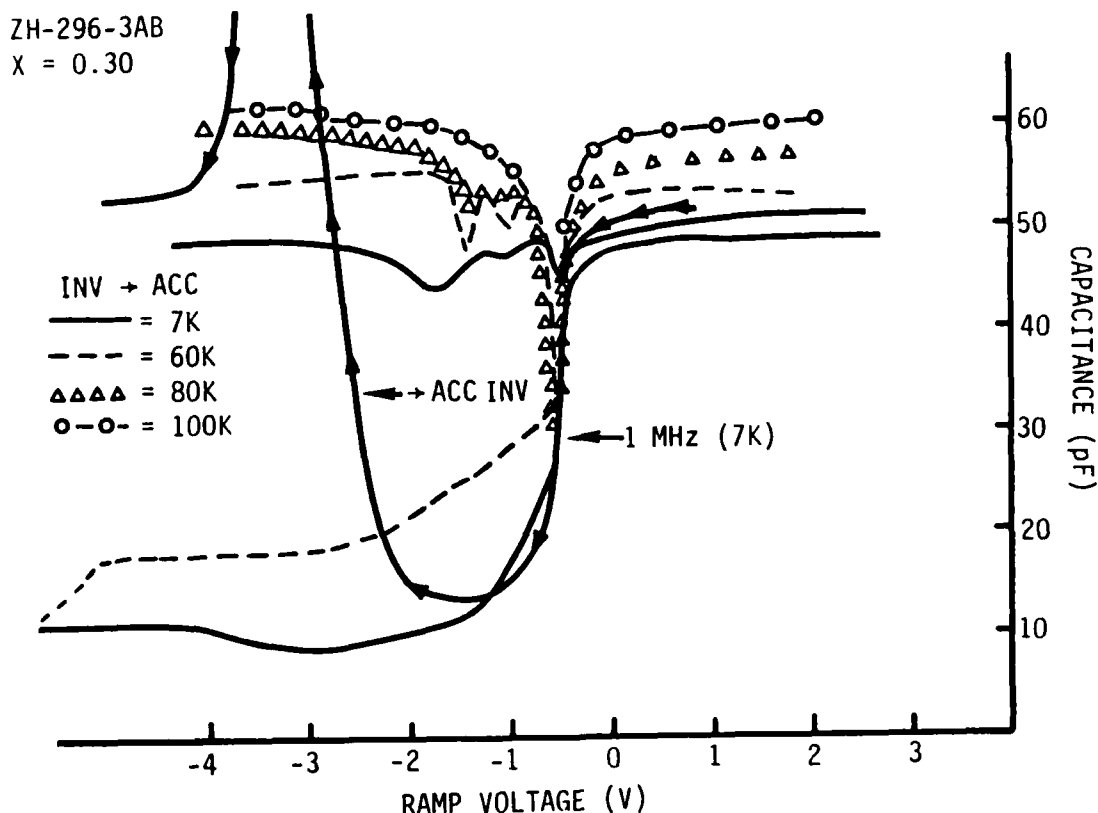


Figure 11. 1 MHz and quasistatic at 7K. Quasistatic ramped from inversion to accumulation versus temperature showing discrete states at onset of inversion.

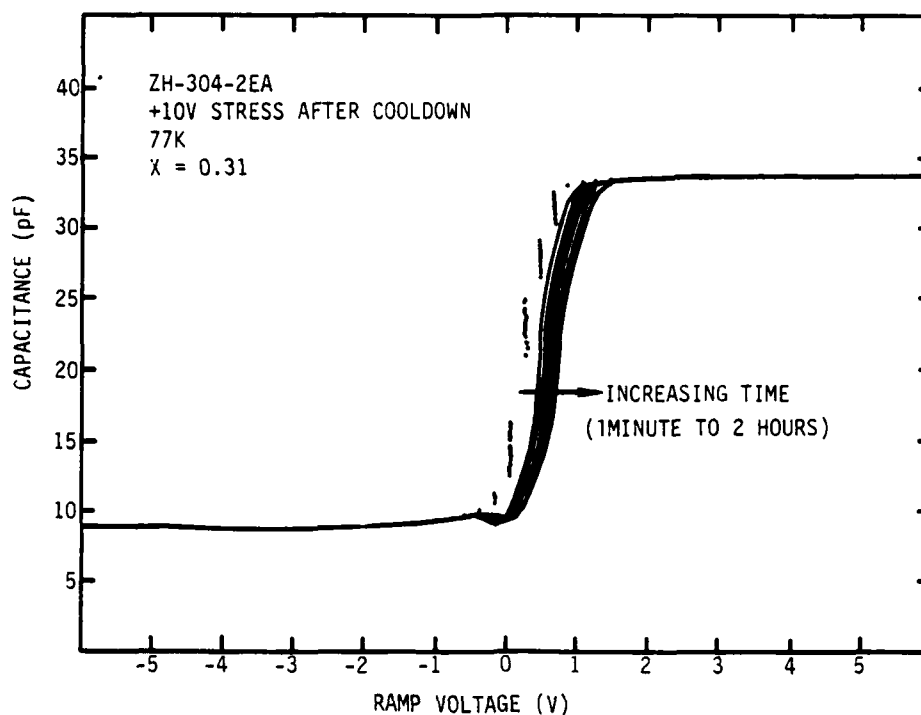


Figure 9. Positive bias with time. V_{FS} follows bias indicative of charge injection from accumulation layer.

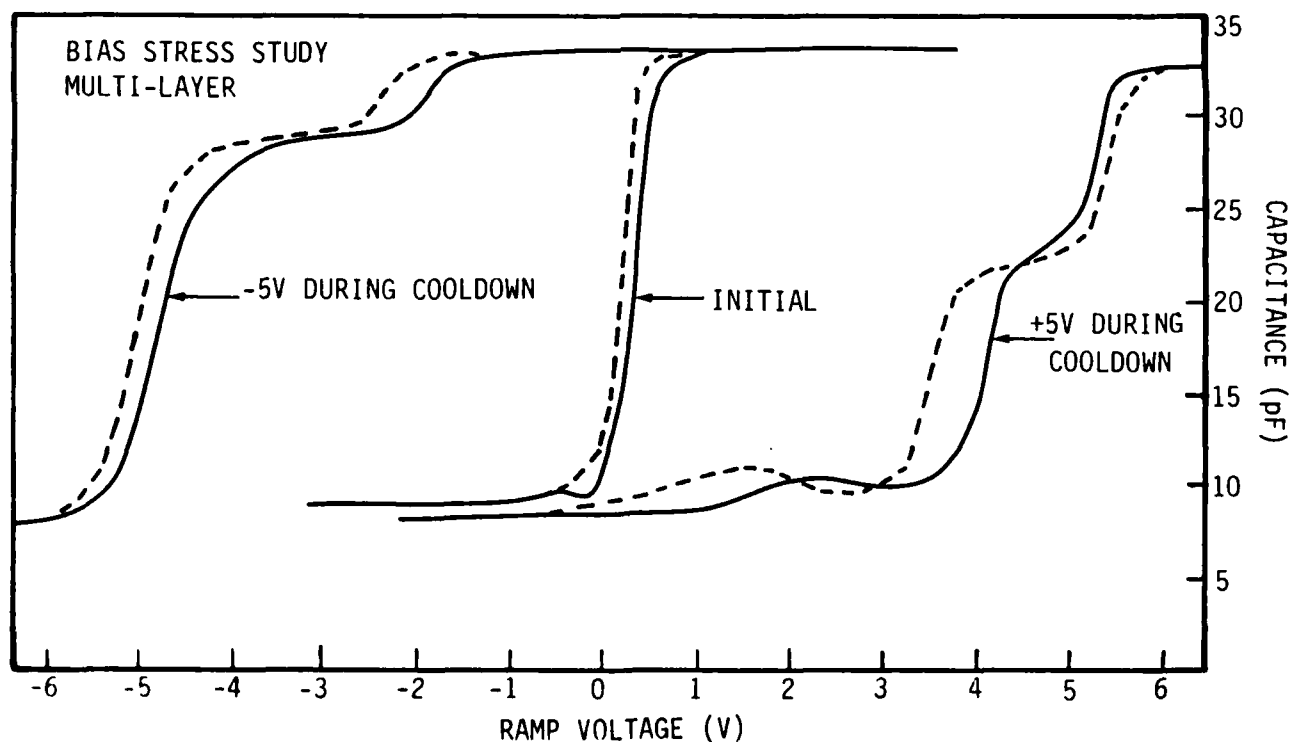


Figure 10. C-V change with bias during cool down. Note hysteresis polarity change in 4 to 6V range of +5V bias and "Steps" in depletion possibly due to oxide trap occupation.

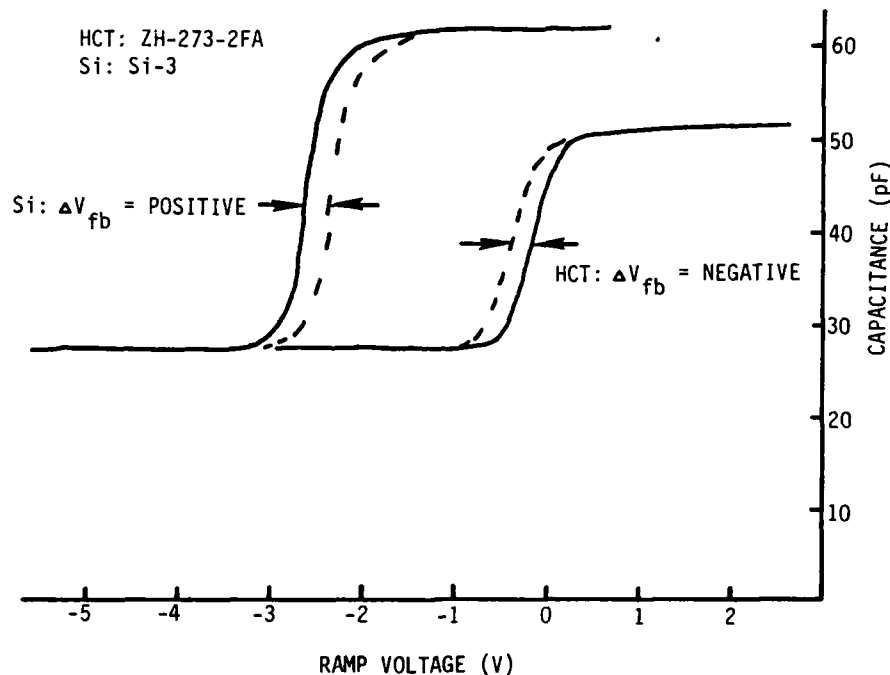


Figure 8. 1 MHz C-V curves on Si and HCT. Ramp started at positive bias. Si hysteresis opposed to bias, HCT hysteresis follows bias indicative of mobile ions and charge injection, respectively, as the major contributors.

Bias-stress measurements have been used to evaluate the stability of this charge under prolonged bias and at elevated temperatures. Standard HgCdTe/Photox™ SiO₂/Ti-Au MIS devices were tested with the following sequence: cooled to 77K at 0V gate bias; biased to ±5V and ±10V for up to two hours with C-V curves taken at regular intervals; warmed to 300K; cooled to 77K with applied biases of ±5V; and again monitored at regular intervals. The overall shift seen in the case of biasing after cool down was in the direction of applied bias and occurred mostly in the first five to ten minutes, as the data in Figure 9 shows. Very small shifts opposed to the applied bias were sometimes seen in the initial two or three minutes. Thus charge injection is still predominant under prolonged bias stress but is reasonably stable at device operating temperatures. The resulting total flatband voltage changed only 0.3V in two hours. Applying bias at room temperature however, produced dramatic changes in the C-V curves subsequently taken at 77K. As shown in Figure 10, flatband voltages were shifted strongly (4 to 5V) in the direction of applied bias, the magnitude of the hysteresis increased a factor of 2 or 3, "steps" appeared (apparently indicative of an incremented transition into full

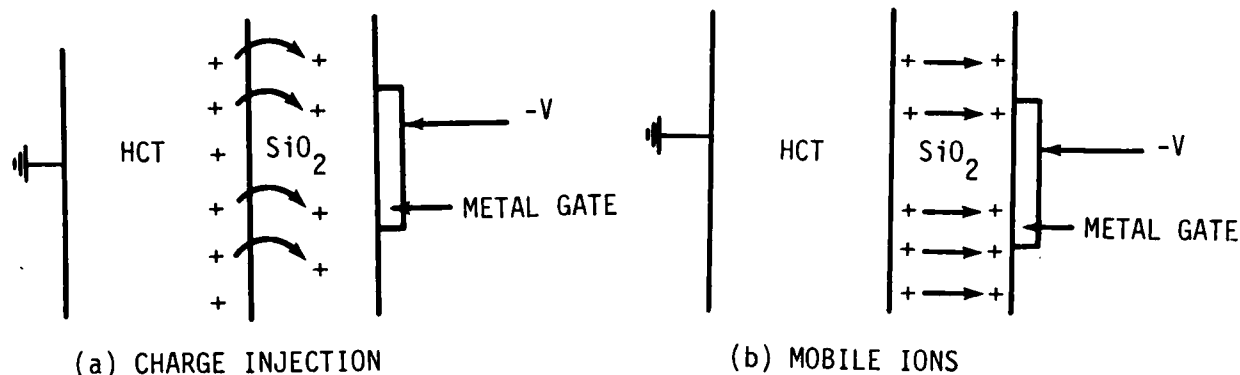


Figure 7. Motion of charge giving rise to C-V hysteresis. (a) positive charge is injected into oxide requiring stronger negative bias (b) positive charge moves closer to gate requiring less negative bias.

Upon the return ramp to positive bias, these charges will be compensated at a less negative bias than was previously required resulting in a positive flatband shift. Charge injection on the other hand, will result in a negative flatband shift due to positive charge injection into a previously uncharged oxide requiring a more negative bias for compensation. This logic applies to both positive and negative ions and biases. The result is that C-V hysteresis is opposed to the bias for mobile ions and follows the bias for charge injection. C-V measurements, with the voltage ramp initially at positive bias, are shown in Figure 8 for both silicon and HgCdTe. Hysteresis are of opposite polarities indicating mobile ions dominate in silicon and charge injection dominates in HgCdTe. The amount of hysteresis is not substantially different.

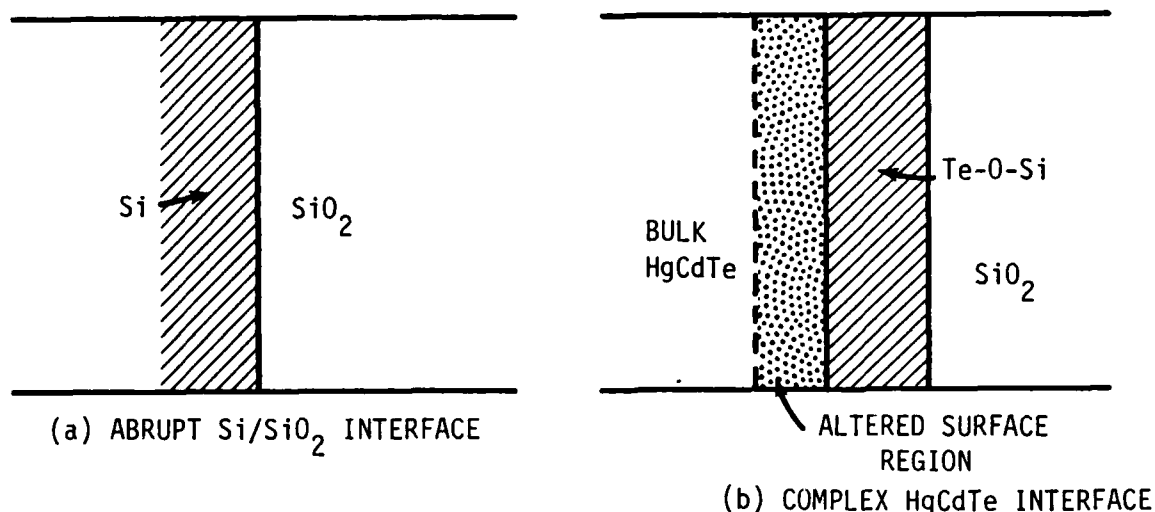


Figure 6. Diagram shows comparison of abrupt Si/SiO₂ interface with HgCdTe/SiO₂ interface which has altered (process-induced) surface region and a reduced native oxide layer. Origin of different surface and oxide trapping sites.

Electrical consequences of the differences between the two systems are apparent in trapping characteristics and predominant charge distributions. Thermal oxidation of the silicon creates fixed and mobile charge in the oxide to which various treatments, such as HCl during oxide growth, have been applied as remedies. Mobile charge in the oxide is still the dominant source of instability. Charge injection, however, is dominant in the HgCdTe system, as can be seen by a comparison of hysteresis in C-V measurements. (Hysteresis is the shift in the C-V curve along the voltage axis after biasing positively or negatively. Figure 7 indicates the motion of charge under negative bias with (a) charge injection, and (b) mobile ions as the source. In the case of positive ions in Figure 7(b), ions be moved closer to the negatively biased electrode.

spike at the onset of inversion. Both effects are lessened as ramp rate is decreased, indicating that equilibrium has not been reached. It is of course, possible to sit at each voltage until equilibrium is obtained. However, use of low frequency admittance spectroscopy will give a more complete picture of these slow states. Whereas C-V measurements use a fixed frequency and scan in voltage, admittance spectroscopy selects a particular voltage and scans the frequency range. This gives the technique the added advantage of being in equilibrium and enables measurement both of trap (or state) distribution across the bandgap as well as unique response time determination. Admittance measurements using equipment at SRI International, capable of frequencies as low as 10^{-4} Hz, reveal a significant trap density responding in the 10^{-2} Hz region.

Interfaces between Photox™ and HgCdTe which show significant concentrations of these slow states have been measured earlier on the surface study contract and reported in the proposal for this study. These are interpreted to be states in the insulator which communicate with the HgCdTe via a tunneling mechanism.

Further characterization of interface traps, oxide states and their interactions have been carried out in bias-stress measurements and C-V versus temperature. Bias-stress measurements will indicate sources of mobile charge and their degree of mobility.

It is instructive to compare the emerging picture of the Photox™/HgCdTe interface to that of SiO₂ on Si. On a physical basis, these interfaces differ dramatically. A schematic of the two systems is shown in Figure 6. As mentioned previously, the HgCdTe surface region is substantially altered stoichiometrically from the bulk by polishes and etches employed in surface preparation. This surface then, on exposure to air, grows a native oxide ≈20Å thick. The ensuing passivation of the surface with Photox™ SiO₂ exposes the surface initially to Silane which reduces the native oxide to the layer of Si, Te and O found in the final device.⁴ Silicon, on the other hand, is a substantially harder material with only one constituent and hence essentially maintains bulk crystallinity up to the surface. When thermal oxidation is performed, a clean interface between the silicon and the SiO₂ passivation results with no intermediate layer. The nature of the SiO₂ layers are also significantly different as discussed in a previous report.

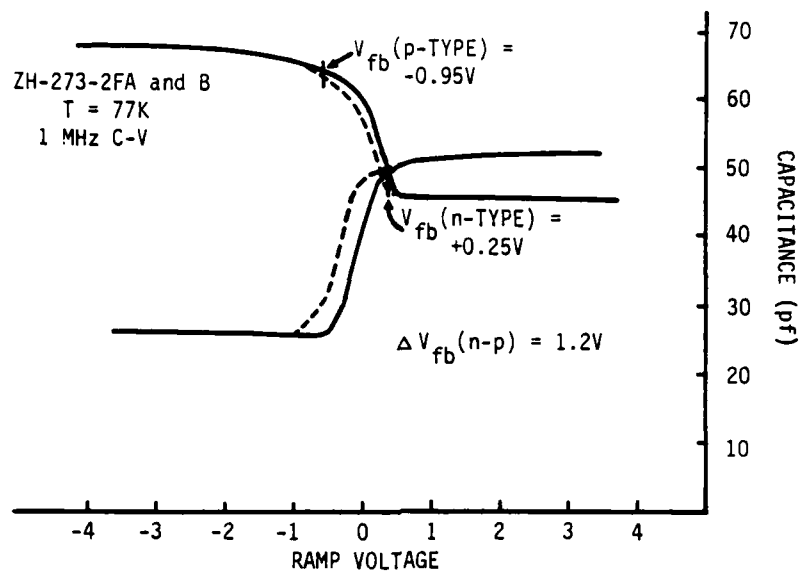


Figure 4. 1 MHz curves showing flatband voltage difference between n and p type material.

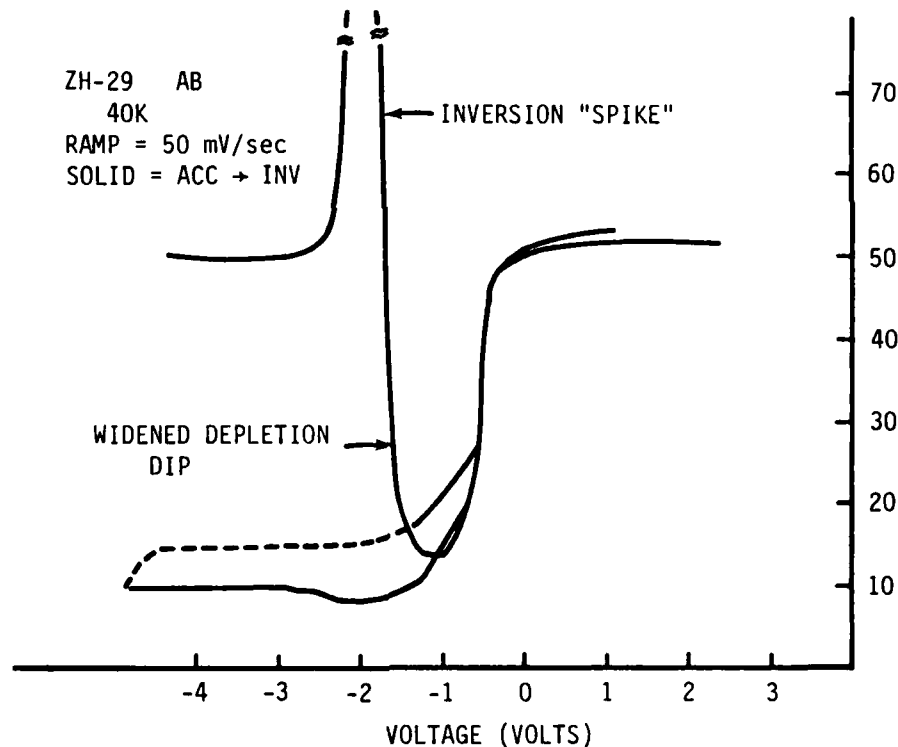


Figure 5. Quasistatic C-V curve with ramp rate faster than required for equilibrium. The widened depletion dip gives an artificially Low value for N_{ss} across the bandgap. The peak at the onset of inversion will not occur under equilibrium and hence makes data reduction here meaningless.

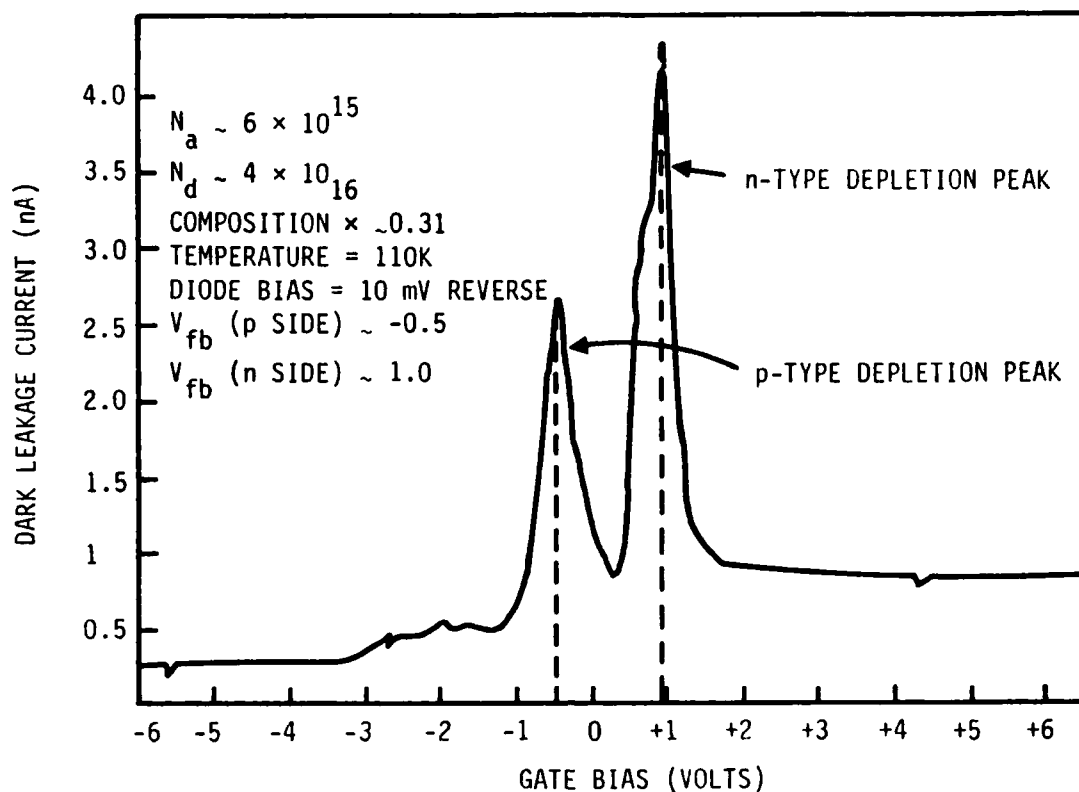


Figure 3. Measurement of dark current versus gate bias for gated diode (Gate overlaps both n and p sides showing a difference in the voltage at which depletion occurs for n and p type material. After J.P. Rosbeck et al.

In addition to the fixed charge and interface trap charge discussed above, the existence of very slow states has been detected indirectly through quasistatic C-V measurements and now, seen directly with admittance spectroscopy. Measurement of D_{it} is typically done by comparison of high and low frequency C-V measurements and use of Berglund Integration to convert gate bias to surface potential (ψ_s). This requires that the low frequency (or quasistatic) sufficiently approximates an equilibrium condition. Typical ramp rates used are 10-50 mV/sec resulting in an equivalent frequency on the order of 1 Hz. Figure 5 shows such a measurement on a high quality MIS device. Seen here are an artificially wide depletion dip and a capacitance

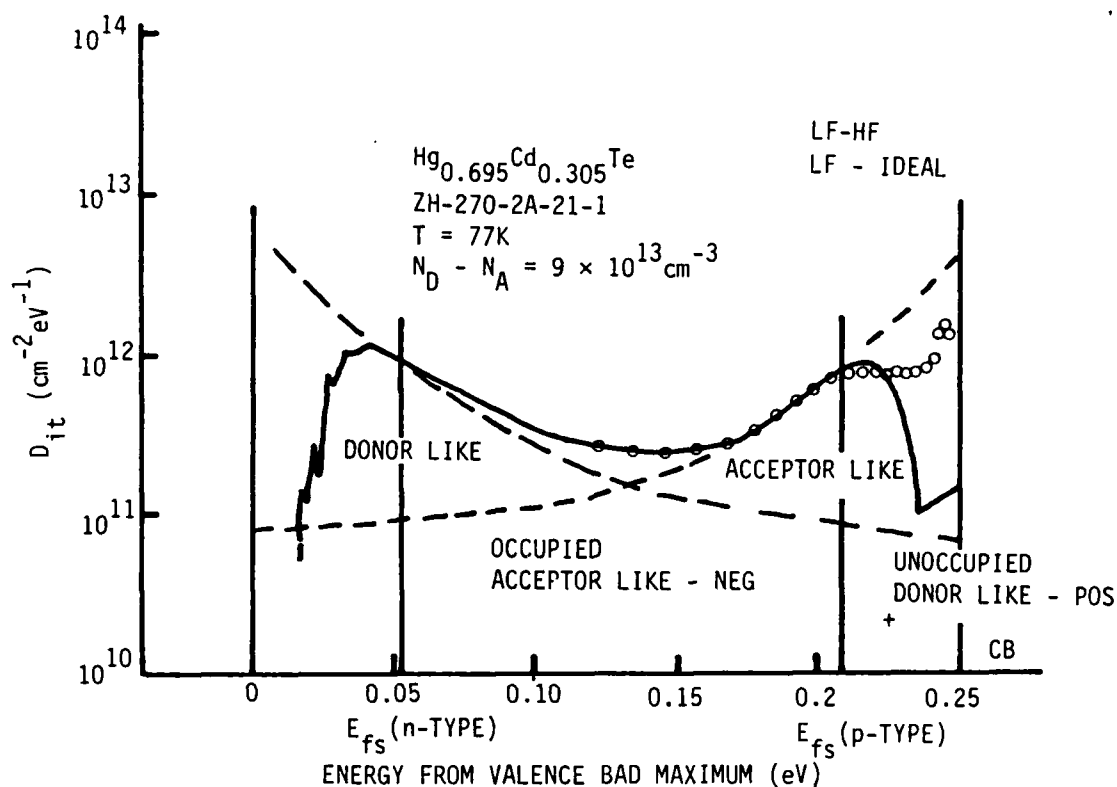


Figure 2. Density of interface traps (D_{it}) derived from low frequency measurements and calculated response (ideal) and low frequency and high frequency measurements. Superimposed are estimated components due to valence and conduction band tailing. Shaded areas show charged contributions.

This effect has been seen in two types of devices, DLHJ detectors and MIS capacitors. Figure 3 shows the effect on dark current of changes in gate bias for a gated photovoltaic detector. Dark current generation from interface states will increase as the change in surface potential (via changing gate bias) causes depletion on the p or n side. The bias at which this occurs for the two sides of the junction differs by nearly 1.5V in this case, as seen by the two peaks in dark current. Shown in Figure 4 are capacitance-voltage characteristics for capacitors fabricated on adjacent wafer sections annealed to comparable doping densities of n and p type. Again, more than a 1V difference is seen in the onset of depletion, represented here as the flatband voltage (V_{FB}). The difference in E_{fs} also causes a difference in the work function for the two material types. However this effect only contributes $\approx 0.2V$, leaving the major contributor to be the different interface trap charge.

Capture cross sections were measured by selecting the capacitor bias, temperature, and rate window (τ) which gave the peak position corresponding to the trap of interest. Gradually shortening the fill pulse duration (τ_{fill}) enabled measurement of the trap fill time as the slope of a plot of τ_{fill} versus signal amplitude.¹⁰

RESULTS

The DLTS spectra showed three peaks (Figure 1). Two were very prominent and well characterized while the third was less pronounced. Obtaining the activation energies of the trap required separating the capture cross section activation energy (E_σ) from the DLTS value (E_{DLTS}) with $E_{DLTS} = E_T + E_\sigma$ where E_T is the actual trap activation energy; E_σ may be determined from the capture cross section values and fill pulse variation data. Trap activation energies were determined to be 0.12 eV, 0.172 eV, and 0.079 eV. These are electron traps since only majority carrier traps are detected; thus, activation energies quoted are measured from the conduction band edge. The above energies are in general agreement with those reported for traps seen in bulk HgCdTe.¹

The activation energies for the two prominent peaks, at 0.172 eV and 0.12 eV, were constant at lower biases and then decreased as bias increased due to the Poole-Frankel effect. The 0.12 eV trap activation energy dropped to a value of ≈ 0.05 eV at fields of 10^4 V/cm. The activation energies quoted were determined from low bias and hence are independent of electric field so that correction for the Poole-Frankel effects is not required. The 0.079 eV activation energy, is also reported in the low field limit and is assumed to be field independent.

Selecting the experimental parameters listed earlier for capture cross section measurement resulted in a capacitance decay curve for the 0.12 eV peak which has two slopes, indicative of two traps emptying at different rates. These capture cross sections are $3.5 \times 10^{-18} \text{ cm}^2$ and $1.1 \times 10^{-16} \text{ cm}^2$. The same method applied to the 0.079 eV peak also showed two traps. One capture cross section is very close to the $1.1 \times 10^{-16} \text{ cm}^2$ obtained previously while the second showed a smaller value of $1.2 \times 10^{-18} \text{ cm}^2$. As can be seen from the DLTS spectra of Figure 1, there is some overlap of the peaks. It can be inferred therefore, that values for capture cross sections obtained from the 0.12 eV peak correspond to the 0.12 eV and 0.172 eV peaks and those from the 0.172 eV peak correspond to the 0.172 eV and 0.079 eV peaks. Due to the similarity of the $1.1 \times 10^{-16} \text{ cm}^2$ value obtained in both measurements this was assigned to the 0.079 eV peak. This leads to capture cross sections for the 0.12 eV and 0.079 eV peaks of $3.5 \times 10^{-18} \text{ cm}^2$ and $1.2 \times 10^{-18} \text{ cm}^2$, respectively. (See Table 1 for summary.) These values indicate the 0.12 eV trap to be neutral, the 0.172 eV trap neutral or attractive and the 0.079 eV state to be neutral or repulsive.^{9,11} The capture cross-sections quoted were measured at 66K and 102K for the 0.172 eV and 0.12 eV traps respectively. A temperature dependence of $\sigma = \sigma_{\infty} \alpha^{-E\sigma/KT}$ is assumed in this region but has not been experimentally verified.

Choosing a bias and temperature range which reveals the 0.079 eV peak and plotting the capacitance transient logarithmically showed three slopes (Figure 2), revealing three distinct decay rates. Plotting a family of curves with temperature as the parameter showed a dependence indicative of real traps as opposed to instrumental effect. The third segment, however, shows an increased slope in the 1,000 to 2,000 μs region. This mandates that initiation of trap decay is delayed until this time. Divalent traps may explain

this behavior, with one trap level's decay dependent on another's emptying. Actual details of the trapping mechanism remain to be determined.

Depth profiling showed the 0.172 eV trap to have a fairly constant concentration from the maximum depletion width up to the surface. The 0.12 eV trap is not present at the surface, but rises in concentration to a level slightly greater than that for the 0.172 eV trap at 0.5 μm , dropping to a nearly equal level in the bulk approximation at 1.0 μm , as shown in Figure 3. Due to the very low relative concentration of the 0.079 eV trap, as well as its proximity to the 0.172 eV trap, an accurate profile could not be determined.

Since DLTS for MIS structures simultaneously profiles two trap distributions; one in energy at the interface and the other spatially from the interface. Each observed peak could, in general, represent a bulk trap or a surface state. To differentiate the energy from the spatial distribution we can examine the energy profile for surface states as determined by C-V analysis. This U-shaped energy distribution of states is not observed in these data, either as a set of discrete states or as two state distributions from the conduction and valence bands. A single discrete surface state, on the other hand, would be observed only when the band bending caused the Fermi level to cross this energy level. The measured activation energies of 0.12 eV and 0.172 eV (again measured from E_c), and the biases which reveal them, are therefore not consistent with the interpretation of surface states; these are taken to be trap levels within the bulk material. The 0.079 eV peak profiles were not complete enough to be able to differentiate between bulk trap and surface state.

CONCLUSIONS

For the first time we have been able to examine HgCdTe electronic properties near its interface with SiO₂. Three distinct trap levels have been observed, as compared to only two seen previously in the bulk material. Bulk trap levels reported¹ were at $1/2E_g$ and $3/4E_g$ with capture cross-sections of $3.5 \times 10^{-17} \text{ cm}^2$ and $6.3 \times 10^{-13} \text{ cm}^2$. Within the limits of error for the two sets of experiments it is likely that these are the same traps as seen in this work at 0.12 eV and 0.172 eV. The non-uniform distribution with depth of one trap and the alteration of its bulk activation energy indicate that surface treatments effect bulk trap levels. The third peak detected (0.079 eV) may be a surface state to which DLTS measurement of diodes is not sensitive. The information obtainable through this technique represents a significant increase in sensitivity over previously reported techniques such as EER and AES.¹²

Acknowledgements:

The authors would like to thank M.E. Boyd for his assistance in software development and one author, V.A. Cotton, would like to thank Professor James Merz (UCSB) for his conversations and support of this work.

REFERENCES

1. C.E. Jones, V. Nair, and D.L. Polla, Appl. Phys. Lett., 39, 248 (1981).
2. D.L. Polla and C. E. Jones, J. Appl. Phys., 52, 5118 (1981).
3. D.L. Polla, M.B. Reine, and C.E. Jones, J. Appl. Phys., 52, 5132 (1981).
4. P.M. Raccach, U. Lee J.A. Silberman, W.E. Spicer and J.A. Wilson, Appl. Phys. Lett. 42, 374 (1983).
5. R.E. Allen, J.P. Buisson, and J.D. Dow, Appl. Phys. Lett., 39, 975 (1981).
6. T.J. Tredwell and C.R. Visvanathan, Appl. Phys. Lett., 36, 462 (1980).
7. N.M. Johnson, D.J. Bartelink, and J.P. McVittie, J. Vac. Sci. Tech., 16, 1407 (1979).
8. M. Schulz and E. Klausmann, Appl. Phys., 18, 169 (1979).
9. M. Schulz and N.M. Johnson, Appl. Phys. Lett., 31, 622 (1977).
10. J.S. Blakemore, Semiconductor Statistics 264 (1962), Pergamon Press, London.
11. J.S. Blakemore, Semiconductor Statistics 156 (1962) Pergamon Press, London
12. A. Lastras-Martinez, U. Lee, P.M. Raccach, and V. Zender, J. Vac. Sci. Technol., 21, 157 (1982).

Table I. Values of Capture Cross Sections

TRAP	$E_T(\text{eV})$	$E_G(\text{eV})$	$\sigma_n(\text{cm}^2)$	PROFILE
1	0.12	0.07	3.5×10^{-18}	Not present at surface rises in concentration comparable to #2 at 1 μm
2	0.172	0.02	1.1×10^{-16}	Fairly constant concentration across depletion region
3	0.079	0.019	1.2×10^{-18}	Low concentration not profiled

Figure Captions

Figure 1. DLTS Spectra

Figure 2. Capacitance Transient with Temperature as Parameter

Figure 3. Relative Trap Concentrations from Depth Profiling

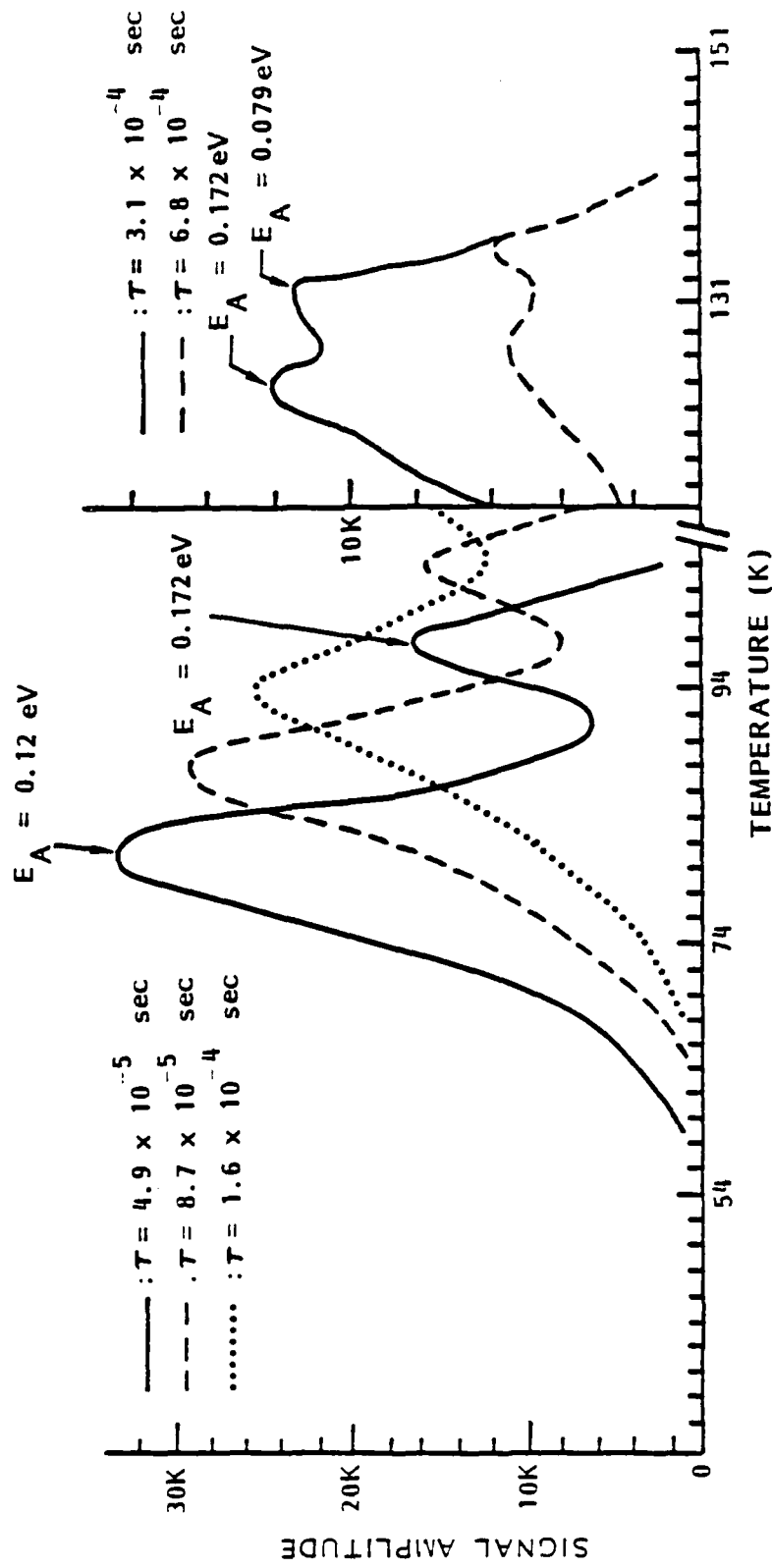


Figure 1. DLTS Spectra.

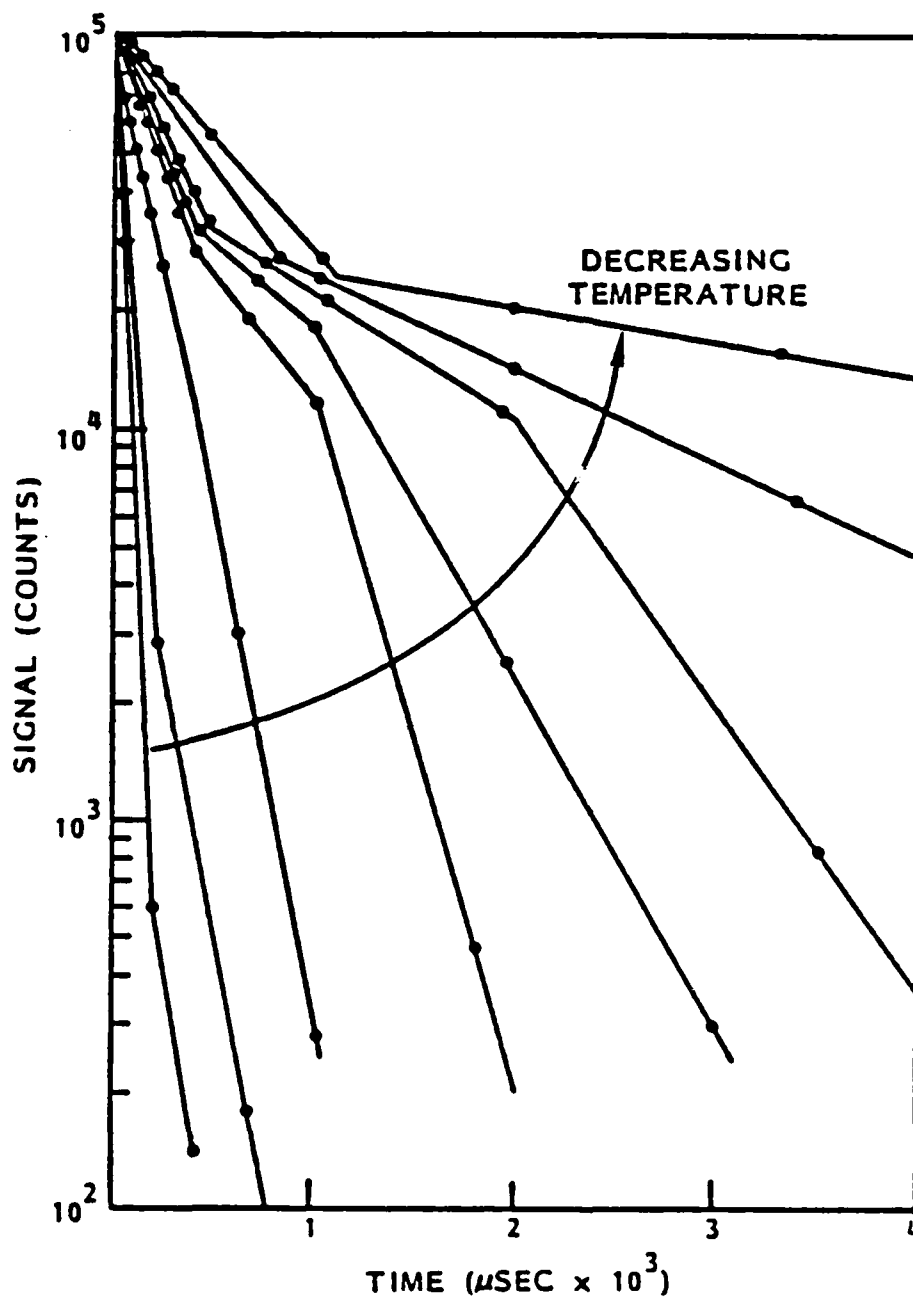


Figure 2. Capacitance Transient with Temperature as Parameter

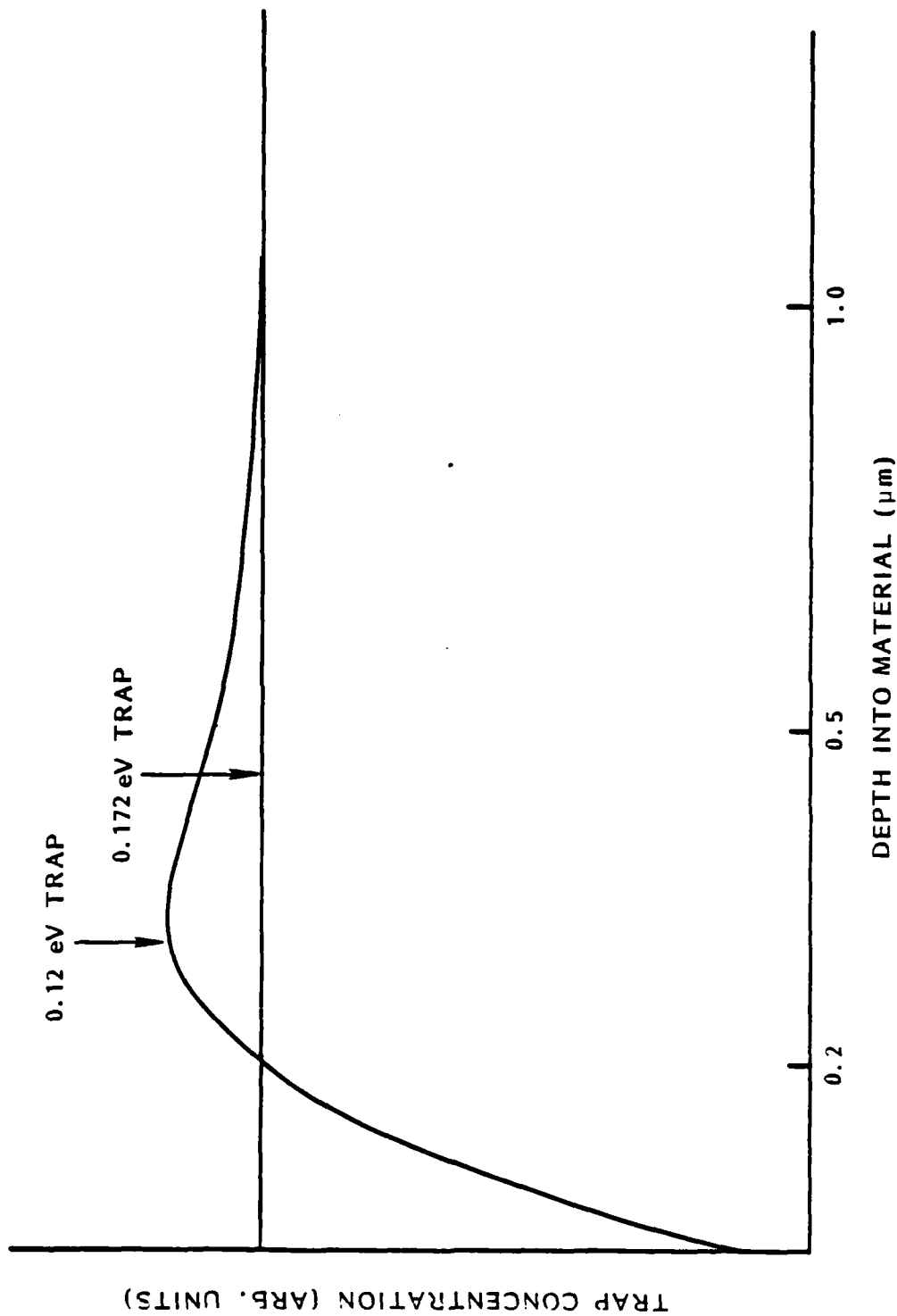


Figure 3. Relative Trap Concentrations from Depth Profiling

Section II

Channeled Implants

Channeled implantation of HgCdTe is being pursued in the interest of producing implanted regions where the doping is determined by the implanted ion concentration and not by the resulting lattice damage. Currently, diodes fabricated using ion implantation are limited to n+ on p due to the high level of n type damage caused by the nuclear stopping component of random implants. No satisfactory method of annealing out this damage has yet been developed.

Atomic profiles of channeled implants are expected to have a random peak at the surface caused by ions which are not channeled on initial impact with the surface, followed by a longer "tail" of atoms which are channeled and hence penetrate more deeply into the material.

Evaluation of these profiles, their variation with mass and their corresponding electrical activity is the purpose of this task. The techniques used are secondary ion mass spectroscopy (SIMS) to obtain the implanted species atomic profile, and capacitance-voltage (C-V) measurements for the corresponding electrical activity. Preliminary evaluation of traps created in the damage process has been carried out using DLTS.

Samples for channeled implant are grown by the solid-state recrystallization method (SSR), which produces single crystal sections of HgCdTe. These are then oriented to the <110> direction and sliced into wafers parallel to this face. Saw damage is removed by a Br/DMF chemo-mechanical polish. Annealing at 240°C in Hg vapor for four weeks results in a doping density of $1 \times 10^{15} \text{cm}^{-3}$ n type to a depth of three to four mils. Several ions were looked at including Na, Cu and As. Implant energies ranged from 90 to 200 keV with doses of $1 \times 10^{11} \text{cm}^{-2}$ to $5 \times 10^{13} \text{cm}^{-2}$. Preparation for C-V analysis utilized the standard polish and etch followed by an additional etch to remove the desired amount of material for depth profiling. MIS devices were made with Photox™ and Ti/Au gates.

In order to have a baseline comparison, random implants were made using unoriented horizontal zone melt material at similar doses and energies. These wafers were also evaluated using SIMS and C-V.

The SIMS profiles of channeled implants made with a range of atomic masses show a clear trend of the peak position moving closer to the surface with increased ion mass. This is shown in Figure 13. For the same dose and energy, the amplitude of this peak also increases with increasing mass. This is the expected result as atomic size increases relative to the available channel cross section more ions will impact the lattice and be implanted randomly. Also seen is the corresponding decrease in amplitude of the channeled "tail" as fewer ions are available for channeling.

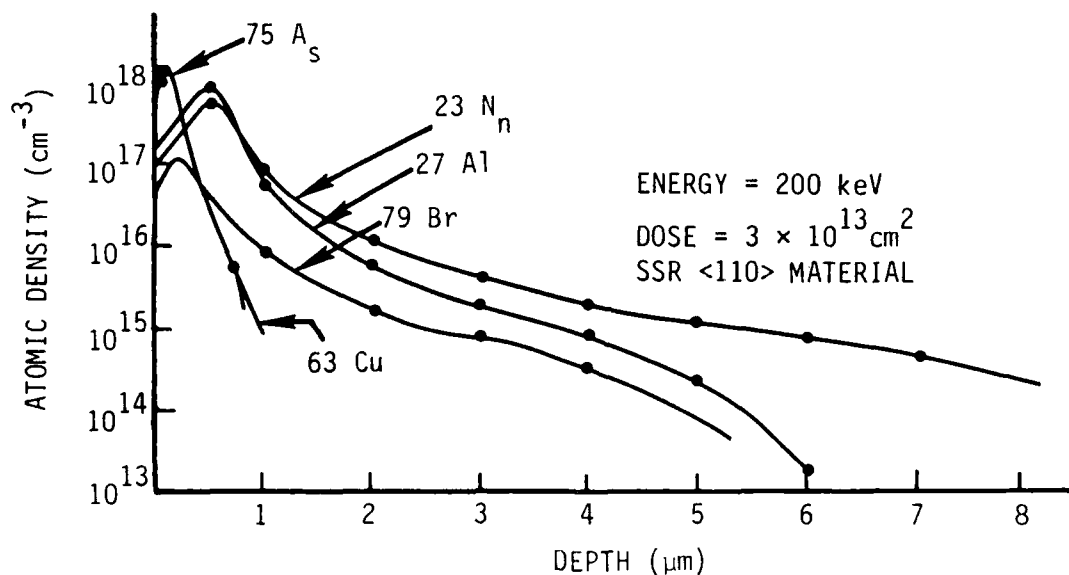


Figure 13. Atomic density profile from SIMS showing change in distribution with atomic size.

A comparison of random and channeled SIMS profiles is shown in Figure 14(a) for Boron. Here the peak positions are at the same depth, with the amplitude somewhat higher for the random case, in agreement with the assumption that this portion of the channeled profile represents a random component. This may be enhanced in our case by the polish which the wafers receive prior to implant which results in a damaged surface, effectively plugging the lattice channels.

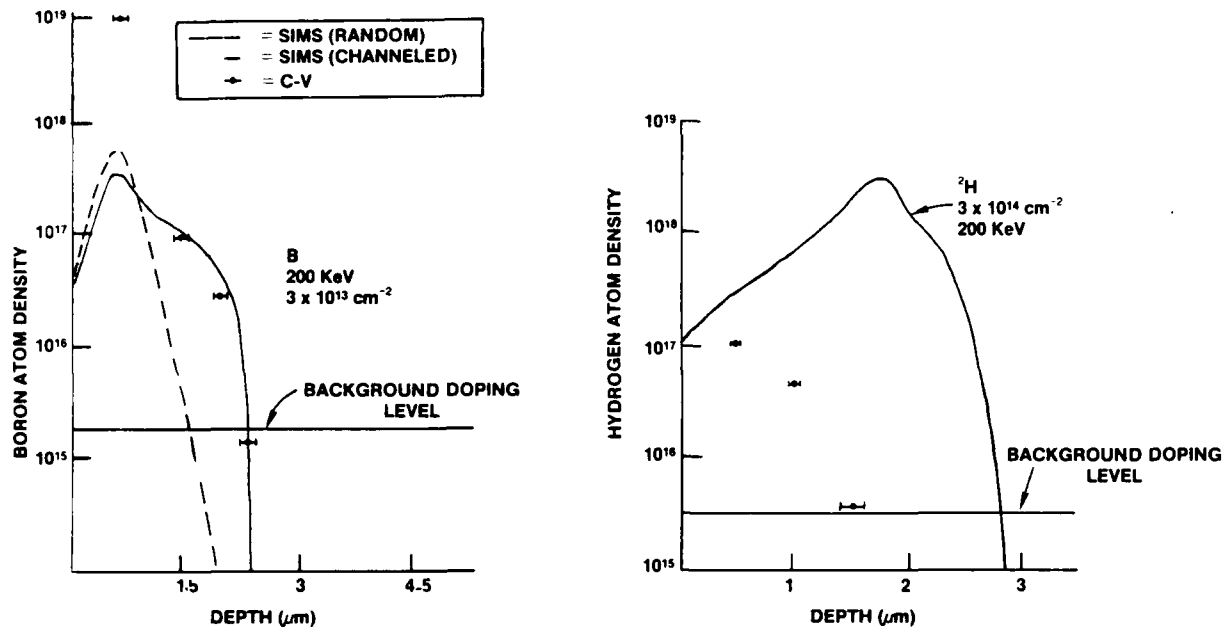


Figure 14. Comparison of electrical activity and atomic concentration profiles (a) for Boron (b) for Hydrogen.

The component of electrical activity measured is n type doping concentration (N_D) obtained from 1 MHz C-V measurements. At this frequency interface traps do not contribute to the capacitance in accumulation or strong inversion and we may use

$$\frac{N_D}{\ln(N_D/n_i) + 1/2 \ln[2\ln(N_D/n_i)-1]} = \frac{4kT\epsilon_{ox}^2}{q^2\epsilon_s x_o^2} \frac{C_{ox}}{C_{HF}(\text{min})} - 1 \quad -2$$

where C_{ox} is the oxide capacitance measured in accumulation, $C_{HF}(\text{min})$ is the minimum capacitance measured in strong inversion, x_o is the oxide thickness, ϵ_o and ϵ_s are the dielectric functions for the oxide and semiconductor respectively and n_i is the intrinsic carrier concentration. This equation assumes uniform doping, hence in our case it yields an average value across the depletion region. This width, combined with depth uniformity and measurement errors, are reflected in the error bars for Figure 14 for the C-V data. The error in the SIMS measurement is $\approx \pm 10\%$ of the final sputter depth, about 0.23 μm in this case.

Electrical activity in the case of moderate masses such as boron and phosphorous appears to follow the random component of the profile with an activity level about an order of magnitude higher than the atomic concentration. This is shown for boron in Figure 14(a). The implication then is that to first order that electronic stopping does not contribute any significant electrical activity. Profiling the electrical activity of random implants appears to follow a similar trend with a slightly shallower distribution. Due to the difference in doping due to residual impurity levels resulting from the two growth methods (SSR and ZH) for these samples, higher doses were used for the SSR material to insure electrical activity above the background level.

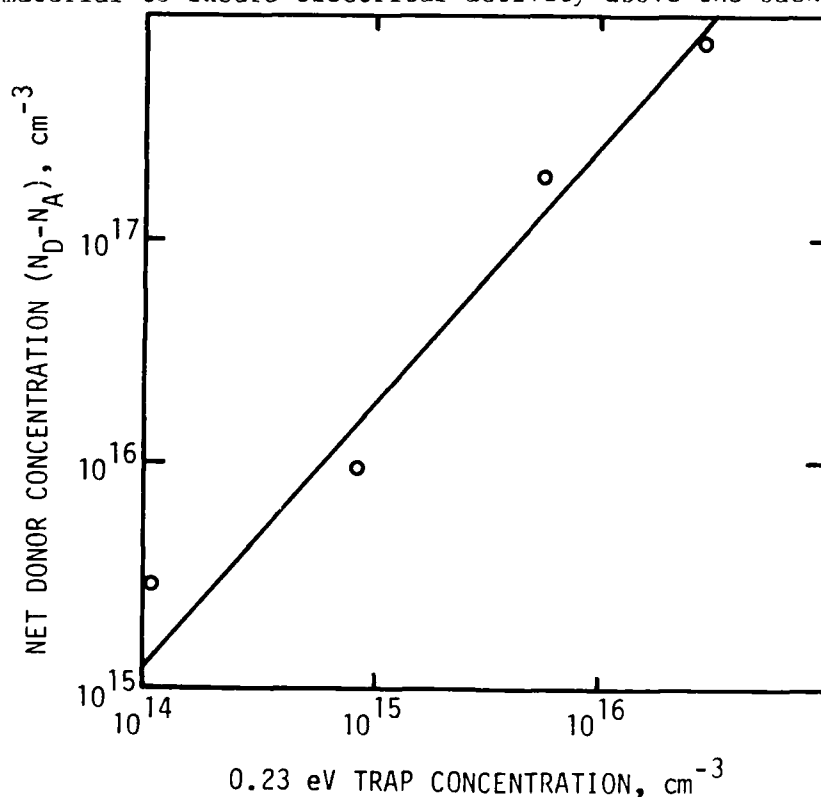


Figure 15. Donor concentration due to implant damage scales linearly with 0.23 eV trap concentration.

It is possible to reliably scale atomic concentration for changes in dose and energy using LSS theory. The mechanism causing damage and electrical activity, however, is not well understood rendering extrapolation impossible in this case. Hence, a direct comparison of doping profiles between channeled and random implants at the same dose and energy is not straightforward, though some data can be scaled for comparison.

direct.

All of the prominent structure in Figure 1 shows some dispersion with photon energy in the normal emission geometry and, as indicated above, can reasonably be accounted for in the bulk band structure of CdTe. Thus, the measurements are not sensitive to a state of distinctly surface origin. The lowest binding energy peak in He I (21.2 eV) spectra of (110) CdTe has been previously assigned to surface state emission [13,14]. The observation of dispersion of this peak (peak 6 in Figure 1) in the data indicates the feature has a substantial bulk contribution. At the lowest photon energies, structure 6 has shifted far from the VBM; a surface state within 0.5 eV of the VBM may account for the nonzero emission seen in the curve, but the possibility of optical transitions from near the band edge to lower lying conduction bands must also be examined.

B. HgCdTe

The result of assuming a free electron final state band with $G = \frac{4\pi}{a}$ (110) and the same value of V_0 as was used for CdTe to analyze data from $\text{Hg}_{0.69}\text{Cd}_{0.31}\text{Te}$ is shown in Figure 5 together with the initial states derived for CdTe in this way and the CdTe bands of Ref. 22. While the value of V_0 appropriate to $\text{Hg}_{1-x}\text{Cd}_x\text{Te}$ may be different from 3.7 eV in the final analysis, use of the same inner potential facilitates a preliminary examination of the composition dependence. As indicated in Figure 2, the initial state structure of the two materials is highly similar, with features in the alloy occurring at increasingly higher binding energy as the measurement probes further from the VBM. This is a consequence of the increasing s-electron content lower in the bands and the greater binding energy of the Hg 6s level compared to Cd. When the data from the $x = 0.31$ sample is compared to that of the $x = 0.23$ alloy the lowest observed state (near -5.4 eV) and bands within 3.0 eV of the VBM are found to be fairly insensitive to the added Hg content while the structure corresponding to the one labelled 3 in Fig. 4 continues to move to higher binding energy. In many cases, the data for the alloy appears

bands, other values of G may contribute [19]. Using the above relation of k and E_f together with the fact that the initial state has the same value of k and an energy lower than E_f by $h\nu$, the initial state bands may be derived from the measured final state energies for the free electron parabola with $G = \frac{4\pi}{a} (110)$. These results are given in Figure 4 together with the calculated valence bands of Chelikowsky and Cohen [22]. The value of V_0 used was 3.7 eV. A similar value, 4 eV, has been obtained from an analysis of the primary beam energy dependence of LEED spot intensities [23].

The correspondence between the experimental initial states and the calculation is generally good, suggesting the theoretical band structure correctly predicts most of the observed features in the ARPES spectra. Refinement of the analysis may further improve the comparison. The shift in the experimental points in structure 5 in Figure 4 from near the lower of the two split bands toward the upper one, for example, results from a change in the relative intensity of emission from the two bands; while the peak position was selected in Figure 1, there are clearly two contributions to the spectra near structure 5 between $h\nu = 16$ and 18 eV (Figure 1). Proper separation of these components would give additional detail to the comparison in Figure 4. The most important correction to the analysis to produce Figure 4 is the use of more realistic final state bands. The structure labeled 2, the portion of structure 1 from $k = 0.5$ to 0.7, and structure 3 and 5 for $k > 0.7$ are likely the result of transitions to final states which may be modeled by free electron parabolas with G vectors other than $\frac{4\pi}{a} (110)$. The increase in intensity in the peak labeled 3 in Figure 1 as the final state changes to the $\frac{4\pi}{a} (110)$ parabola between $h\nu = 17.5$ and 21 eV corresponding to $0.6 \geq k \geq 0.35$ in Figure 4) supports this explanation. The dispersionless portion of structure 1 between 0.15 and 0.5 also involves final states other than the $G = \frac{4\pi}{a} (110)$ parabola, but these transitions may not be

IV. Discussion

The uncertainty in k_{\perp} [8] renders incomplete the determination of the quantum numbers for electron states in a solid; k_{\parallel} is determined by the experimental geometry, but k_{\perp} must be obtained by analysis. If calculated valence bands and conduction bands of sufficiently high energy are available, comparison of the measured initial and final state energy with theory along the appropriate line in reciprocal space can give k_{\perp} . When the initial state dispersion only is known, the measured peak positions can be used to map the conduction bands [17,18]. To derive the valence band E versus k relation when the final state structure is also not known, on the other hand, approximate conduction bands such as free electron parabolas may prove successful [19]. Electronic structure calculations for CdTe in the (110) direction have been performed; [20-22] however, final states of sufficient energy are not available. The present ARPES data can be compared with calculation if a free electron final state is assumed. By such a procedure, the accuracy of the initial state calculations can be studied, and deviations from a free electron parabola for the high lying conduction bands examined. Preliminary results for the alloy samples can be obtained from similar analysis.

A. CdTe

In the case where the final states lie on a free electron parabola, $E_f(k)$ is given by

$$E_f = \frac{\hbar^2}{2m} (k + G)^2 - V_0$$

where G is a reciprocal lattice vector and V_0 , the energy difference between the bottom of the free electron parabola and the valence band maximum, is the inner potential [8]. The strongest contribution to the photocurrent should come from the final state band with $G = 0$ in the extended zone scheme or the portion of the parabola translated to the first Brillouin zone by $G = \frac{4\pi}{a}$ (110) [19] for the range of photon energies used. Because of the complexity of the true final state

The similarity observed, however, suggests that complete comprehension for CdTe or an alloy of a given composition will greatly aid analysis for alloys with different x value.

In addition to location of the electron states in a solid by means of analysis of the position and movement of peaks in the spectra, information as to the symmetry of the states can be obtained from the polarization dependence of the peak intensity. Figure 3, spectra of CdTe and $\text{Hg}_{0.77}\text{Cd}_{0.23}\text{Te}$ for the three polarizations used and $h\nu = 16$ eV, illustrates this sensitivity. (The data has been normalized to the incident flux and corrected for differing backgrounds in the region of interest.) For s-polarization along the $[001]$ direction, one observes considerable enhancement of the peak near -2.7 eV in both cases but particularly in CdTe, while the structure closest to the VBM is not strongly excited for this polarization. When oriented in the $[001]$ direction, the polarization vector is even upon reflection in the $(\bar{1}10)$ mirror plane of the crystal. Since in normal emission the final state wavefunction is similarly even, a nonzero matrix element for optical excitation requires the initial state to also have even reflection symmetry [12]. Thus the valence band state contributing near -2.7 eV must be even upon reflection in the $(\bar{1}10)$ plane while the states contributing nearest the VBM at this photon energy are of odd character. While the trends observed with changing polarization reflect the overall similarity of the electronic structure of the alloy for all compositions studied, the detailed behavior depends on the initial states involved for a given photon energy and the wavelength dependent optical properties of each material, which determine the electric field direction inside the crystal and thus the excitation [8]. The symmetry of the states contributing to the ARPES measurement as determined by the polarization dependence of the spectra can be used as an important test of the comparison of the experimental electronic structure to theory.

previously reported normal emission data from (110) CdTe [13,14] recorded with the He I resonance line (21.2 eV) indicated reasonable agreement, particularly given differences in the polarization of the exciting radiation. Dispersion of the observed structure with the exception of the highest binding energy peak near -4.6 eV was similarly reported in ARPES studies of fixed $h\nu$ and variable emission angle [14] as well as in angle integrated experiments with variable $h\nu$ [5].

The dispersion with photon energy of features in the electron energy distribution curves from CdTe seen in Figure 1 is characteristic of all samples studied. Although the general features in the spectra from HgTe are the same as found for CdTe, the dispersion is somewhat less pronounced most likely as a result of the rougher surface produced by a poorer cleave [15]. (Time did not permit additional cleaves to be made in an effort to improve the surface quality.) Indeed, a correspondence of the structure observed for CdTe and the alloys in terms of relative location and polarization and photon energy dependence can be found in each case. A comparison of the emission along the sample normal for p-polarization of $h\nu = 18$ eV for the four samples studied is given in Figure 2. For the crystals containing Hg, the highest binding energy feature is found near -5.5 eV independent of composition. (If the virtual crystal description of the electronic structure held for these states, a monotonic change in energy would be expected [15].) The intense peak in the curve for CdTe near -3.5 eV is observed at smoothly increasing binding energy in the alloys and HgTe. Similarly the two peaks or peak and shoulder near the VBM are replicated for each composition, while structure between -2 and -3.5 eV apparently increases in strength as the Hg content increases. Because the energy and intensity of features in the data depend on the final state energy and dispersion as well as that of the initial states, analysis of the final state bands for each compound must be performed in order to fully understand the composition dependence of the curves at a given photon energy.

and constant wavelength resolution $\Delta\lambda = 8.7 \text{ \AA}$. Samples of CdTe (II-VI, Inc.) and solid state recrystallized $\text{Hg}_{1-x}\text{Cd}_x\text{Te}$ ($x = 0.00, 0.23, \text{ and } 0.31$) were introduced into the vacuum chamber following bakeout through an air lock. Clean (110) surfaces of the $5 \times 5 \times \sim 15 \text{ mm}^3$ bars were exposed by cleaving across the square faces in vacuum ($p \sim 2 \times 10^{-10} \text{ Torr}$). The cleaved surfaces of the alloy were found to be n-type by determination of the Fermi level position. Departure from the bulk stoichiometry was not resolved in UPS spectra; the ratio of Hg 5d to Cd 4d emission in the data for the alloys scaled with bulk composition in the expected way. Prior to ARPES measurements, the crystal axes were oriented using the Low Energy Electron Diffraction (LEED) pattern.

III. Results

Electron energy distribution curves for normal emission from (110) CdTe under p-polarized irradiation (26° from normal along $[\bar{1}10]$) are presented in Figure 1 as a function of initial state energy relative to the VBM for 0.5 eV increments of the photon energy. Prominent peaks in the data are marked and are observed to shift in binding energy and modulate strongly in intensity as the photon energy is varied. Such peaks occur when valence band and conduction band states of the same value of k in the reduced Brillouin zone scheme are separated in energy by the photon energy. As $h\nu$ is varied, the values of k and initial state energy for which these conditions are met change in a way characteristic of the dispersion of the initial and final state bands involved. An exception to this type of behavior is seen in the peak near -4.6 eV (structure 1) at the higher photon energies. This apparently stationary peak arises from the mainly cation s-electron derived states which have little dispersion deep in the valence bands and near the zone boundary. The characteristic motion of the peaks marked in Figure 1 will be used to compare the measured electronic structure to calculation in Section IV. Comparison of spectra for photon energies of 21.0 or 21.5 eV to

the symmetry line through the points $\Gamma K X$ in the Brillouin zone of the face centered cubic lattice [11]. A second geometry was used to restrict emission from the mainly s-electron derived state 3.5 to 6 eV below the VBM (where the nonperiodic potential effects are strongest) to the hexagonal face of the Brillouin zone along the WLW line [11]. This data, which bears on the breakdown at the virtual crystal approximation at the zone boundary, will appear in a later publication.

Measurements in these geometrics were carried out in an ADES 400 (VG Scientific) angle-resolving system. The μ -metal chamber is pumped by a 400 l/s triode ion pump and titanium sublimation pumping. Electron energy analysis is accomplished by a moveable hemispherical electrostatic analyzer with channeltron electron multiplier detector and pulse counting electronics. The analyzer acceptance cone, 2° degree in half angle, can be freely oriented relative to the sample by rotating the analyzer from 5° above to 90° below the horizontal plane and by rotating the analyzer through 360° about the vertical chamber axis. Operating with the pass energy fixed provided a constant energy resolution of 0.2 eV.

Linearly polarized radiation with $13 \leq h\nu \leq 27$ eV from the 8° beam line (I-1) at the Stanford Synchrotron Radiation Laboratory served to excite the photoelectrons. By varying the angle of incidence of the photon beam and rotating the sample about the surface normal, the direction of polarization could be controlled. The orientation of the polarization influences the spectrum through symmetry dependent optical selection rules [12] governing the transition from initial to final state. Measurements were made in the normal emission geometry with increments in the photon energy of 0.5 or 1.0 eV for the vector potential oriented 70° from the sample normal (stronger s-polarization) along both the $[001]$ and $[\bar{1}10]$ directions and 26° from the normal (stronger p-polarization) toward $[\bar{1}10]$. The choice of monochromator slit settings gave a $2 \times 2 \text{ mm}^2$ spot

bond [6]. Based on evidence of the binding energy shifts of the Hg 5d and Cd 4d core levels between the alloy and the binary compounds, the disparity in the bond strength of the two metal atoms increases upon alloy formation, with important implications in areas such as heterojunction formation and dislocation creation and motion [7].

To probe the dependence of the electronic structure on composition and explore the effects of the disorder in the cation potential on the valence bands in the alloy, angle-resolved photoemission spectroscopy (ARPES) [8] is a particularly well-suited technique. The anisotropy of the allowed electron states of a solid in reciprocal space is reflected in the spatial variation of the photoexcited electron emission. By measurement of the energy distribution of the electrons photoemitted into a small solid angle in a particular direction relative to axes in the crystal, information on both the energy and crystal momentum, k , of the valence and conduction band states in the solid can be obtained. ARPES has been used in this way to map the valence and high lying conduction band states in a range of materials [9] including metal alloys such as CuNi [10], which, like HgCdTe, exhibits strong potential disorder. In the present study, ARPES has been used to examine the electronic structure mainly along the (110) symmetry line of CdTe and HgTe as well as $\text{Hg}_{1-x}\text{Cd}_x\text{Te}$ alloys with $x = 0.23$ and $x = 0.31$. The spectra obtained are presented in section III and a comparison of the valence electronic structure of the materials is given in section IV.

II. Experimental

The electron states to which one is sensitive in an angle-resolved experiment are a function of the photon beam energy and polarization and the position of the electron detector. The spectra reported here were recorded with the electron analyzer along the normal to the (110) cleavage face of the samples studied. In this configuration, k_{\parallel} is required to be zero and all initial states lie along

I. Introduction

Accurate knowledge of the band structure of a material provides the means to estimate properties ranging from the ease of dislocation formation to the conduction band effective mass. The HgTe-CdTe superlattice system is a case in point: electronic [1] and optical [2] properties of the material have been predicted theoretically prior to observation which may make the superlattice of technological interest. The accuracy of the quantities derived from the electronic structure depends on how well the band structure is known, motivating study of the electron states in a given material.

The relation between the electronic structure and materials properties is particularly evident in $\text{Hg}_{1-x}\text{Cd}_x\text{Te}$. The strong relativistic interactions between the nucleus and the valence s-electrons in atomic Hg coupled with the influence of the just completed d-electron shell serve to increase the binding energy of the Hg 6s electrons by 1.4 eV [3] compared to the lighter Cd, where these effects are smaller. As a result of the shift in the valence electron binding energy, the conduction band minimum in HgCdTe, which is cation s-electron derived, moves closer to the valence band maximum (VBM) as Hg is substituted for Cd in the lattice [4]. At the same time, the VBM is comprised of Te p-derived states and is fairly insensitive to the composition change. Thus the ability to tune the alloy bandgap by varying the composition follows from the valence electronic properties of the constituents [5,6,7].

A second immediate consequence of the alloy electronic structure relates to the bonding of Cd and Hg in the lattice. The disorder in the potential in the cation sublattice introduced by the differing strength of the interaction of the s-electrons with the cation nuclei results in distinct contributions to the alloy valence electronic structure from Hg and Cd [5]. Consequently, the Cd bond to Te in the alloy differs from that of Hg. In the respective binaries, the Hg-Te bond is considerably more metallic and weaker than the Cd-Te

ANGLE-RESOLVED PHOTOEMISSION SPECTROSCOPY OF $\text{Hg}_{1-x}\text{Cd}_x\text{Te}$

J. A. Silberman^a, D. Laser^b, C. K. Shih, D. J. Friedman, I. Lindau
and W. E. Spicer^c

Stanford Electronics Laboratory
Stanford University, Stanford, CA 94305

J. A. Wilson
Santa Barbara Research Center, Goleta, CA 93017

ABSTRACT

Angle-resolved photoemission spectroscopy, a technique which provides direct information on the quantum numbers k and E which characterize the electron states in a periodic solid, has been used to study the electronic structure of the alloy $\text{Hg}_{1-x}\text{Cd}_x\text{Te}$ for $x = 1.0, 0.31, 0.23$ and 0.0 . Data were collected mainly for emission along the normal to the cleaved (110) face of these crystals as a function of photon energy with various directions of polarization. The structure observed in the spectra of the alloy are similar in dispersion and polarization dependence to that obtained for CdTe. Preliminary analysis of the observed features using a free electron final state reveals the bulk origin of the measured transitions by comparison to calculated valence bands and elucidates aspects of the composition dependence of the valence band states involved in the optical excitation.

a) Fannie and John Hertz Foundation Fellow

b) Present address: Ministry of Defense, P. O. Box 2250, Haifa, Israel

c) Stanford Ascherman Professor of Engineering

The unusual bond length relaxation exhibited in HgCdTe is discussed in section III. The weak Hg-Te bond leads to mechanical instability of the HgCdTe lattice; the trends predicted for the bond length relaxation in this alloy should exacerbate this instability. In order to test our overall theoretical approach, the theoretical model presented in this section is shown to predict the trend observed experimentally by Mikkelsen and Boyce [3] for the pseudobinary alloy InAs-GaAs. This work is included as an appendix to section III.

The effects of this unusual bonding behavior on the thermodynamics and kinetics governing growth at interfaces are seen experimentally in the last two sections. The heterojunction between LPE HgCdTe is studied in the fourth section, where it is seen that HgCdTe exhibits a more metallic-like recovery behavior than CdTe when bombarded with ions. The observations also support the weakness of the Hg-Te bond and the consequent ease of formation of a vacancy attributed to Hg. The kinetics of the activated oxygen uptake on the surface of the HgCdTe are investigated in section V. The uptake of oxygen for the first two monolayers appears to scale with the number of Hg-Te bonds in the alloy. Hence, the breaking of this bond and the subsequent removal of Hg from the lattice appears to play an important role in the beginning stages of oxidation.

References:

1. W. E. Spicer, J. A. Silberman, I. Lindau, A. Sher, A.-B. Chen, J. Vac. Sci. Technol. A 1 (1983) 1735.
2. W. A. Harrison, J. Vac. Sci. Technol., A 1 (1983) 1672.
3. J. C. Mikkelsen, Jr., and T. B. Boyce, Phys. Rev. B 28 (1983) 7130.

Section III-I

SEMIANNUAL TECHNICAL REPORT

July 1, 1984

J. A. Silberman, G. P. Carey, C. K. Shih, D. J. Friedman
I. Lindau and W. E. Spicer

I. Introduction

The underlying theme brought forth in our fundamental studies of the HgCdTe surface, interface, and bulk regions is the unusual nature of the bonding in the alloy. The differences in the cation bonding [1] in the alloy are manifest in the electronic structure and mechanical behavior of the material. Theoretical calculations [2] reveal that not only does the Hg-Te bond exhibit more metallic-like behavior than is typically observed in tetrahedrally bonded covalent semiconductor systems, but that Hg-Te and Cd-Te bond length relaxation in the alloy exhibits unusual trends as well. The trend is for the already shorter Hg-Te bond to shorten as Hg is added to CdTe and the longer Cd-Te bond to lengthen as Cd is added to HgTe. This suggests that an unusual micro-mechanical behavior exists in the alloy that may markedly affect the bulk thermodynamic properties of the material. This should therefore produce significant effects in growth processes. For example, those that govern materials growth at LPE interfaces as well as in bulk regions.

Studying the electronic structure of HgCdTe yields valuable insights into bonding nature and electronic behavior. Once the band structure is understood, many properties of the alloy may be calculated. Section II discusses the experimental determination and our current knowledge of the electronic structure of HgCdTe.

(This Page Intentionally Left Blank)

In the case of hydrogen, Figure 14(b), the electrical activity is distinctly n type and well above the background level due to residual impurities, however there is no apparent correlation between atomic and electrical profiles of channeled samples. SIMS of random Hydrogen implants is not yet available.

DLTS measurements on samples implanted with Cl at a range of doping densities (due to implant damage) show a new trap with an activation energy of 0.20 eV ($E_g = 0.27$ eV at 200K where the DLTS peak is found) measured from the conduction band edge. The capture cross section of $9.6 \times 10^{-20} \text{ cm}^2$ is indicative of a weak repulsive trap. As shown in Fig 16 the concentration of this trap decreases almost linearly as doping density decreases, which is to be expected if it is due to damage created by the implant. The concentration of this trap is an order of magnitude lower than the doping density which gives it a nearly one-to-one correspondence with implant species concentration. Another trap is also seen with $E_A = 0.053$ eV and $\sigma_n = 2 \times 10^{-18} \text{ cm}^2$ which becomes more dominant as doping density approaches the background level. This trap is most likely the same as the 0.079 eV level seen in unimplanted material. Neither of the prominent traps as seen in unimplanted material at 0.12 eV and 0.172 eV have been detected in these implanted samples.

to show less dispersion than observed for CdTe (see Figure 5); this may be an effect of the non-periodic alloy potential.

As is evident in Figure 5, all peaks in the data from $\text{Hg}_{0.61}\text{Cd}_{0.39}\text{Te}$ (and the other samples as well) can be accounted for by the bulk rather than surface electronic structure in analogy to the assignments of these features to the valence bands of CdTe. Of the published band structures for HgCdTe, those which give the valence bands in the (110) direction [20,24,25] predict band widths which are generally less than observed. Recent calculations performed in the coherent potential approximation [26,27] are the most suitable for comparison to the experimental data; however, the valence bands in the (110) direction are not given.

V. Summary

The utility of ARPES lies in the sensitivity of this technique to the quantum numbers k and E which characterize the electron states of a periodic solid. ARPES data collected normal to the (110) face of CdTe and HgCdTe alloys have been examined by assuming a free electron final state. The true final states in these materials are clearly more complex, as illustrated by the divergence of experiment and a calculated band structure for some features in the data. Still, much of the observed initial state dispersion corresponds to prediction, tentatively confirming the accuracy of the calculation as well as the nearly free electron nature of some final states. Refinement of the comparison to theory by incorporation of additional final states and consideration of the photon beam polarization dependence will allow greater accuracy in the determination of the correctness of calculation and, ultimately, of predicted materials parameters derived from the electronic structure.

VI. Acknowledgements

We express our appreciation to Roger A. Cole of SBRC for crystal growth. The work reported was supported by DARPA contract 916610-85 and performed at the Stanford Synchrotron Radiation Laboratory, which is supported by the Department of Energy, Office of Basic Energy Sciences; and the National Science Foundation, Division of Materials Research.

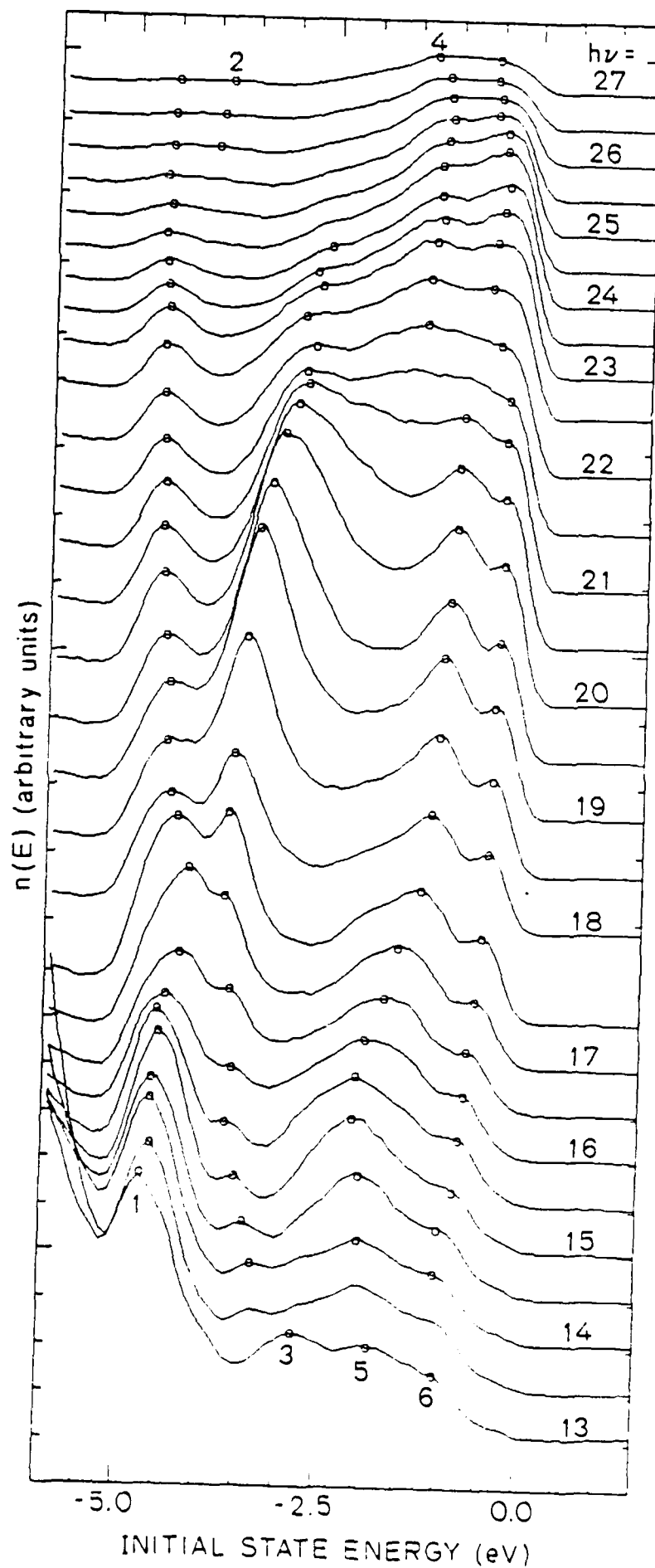
References

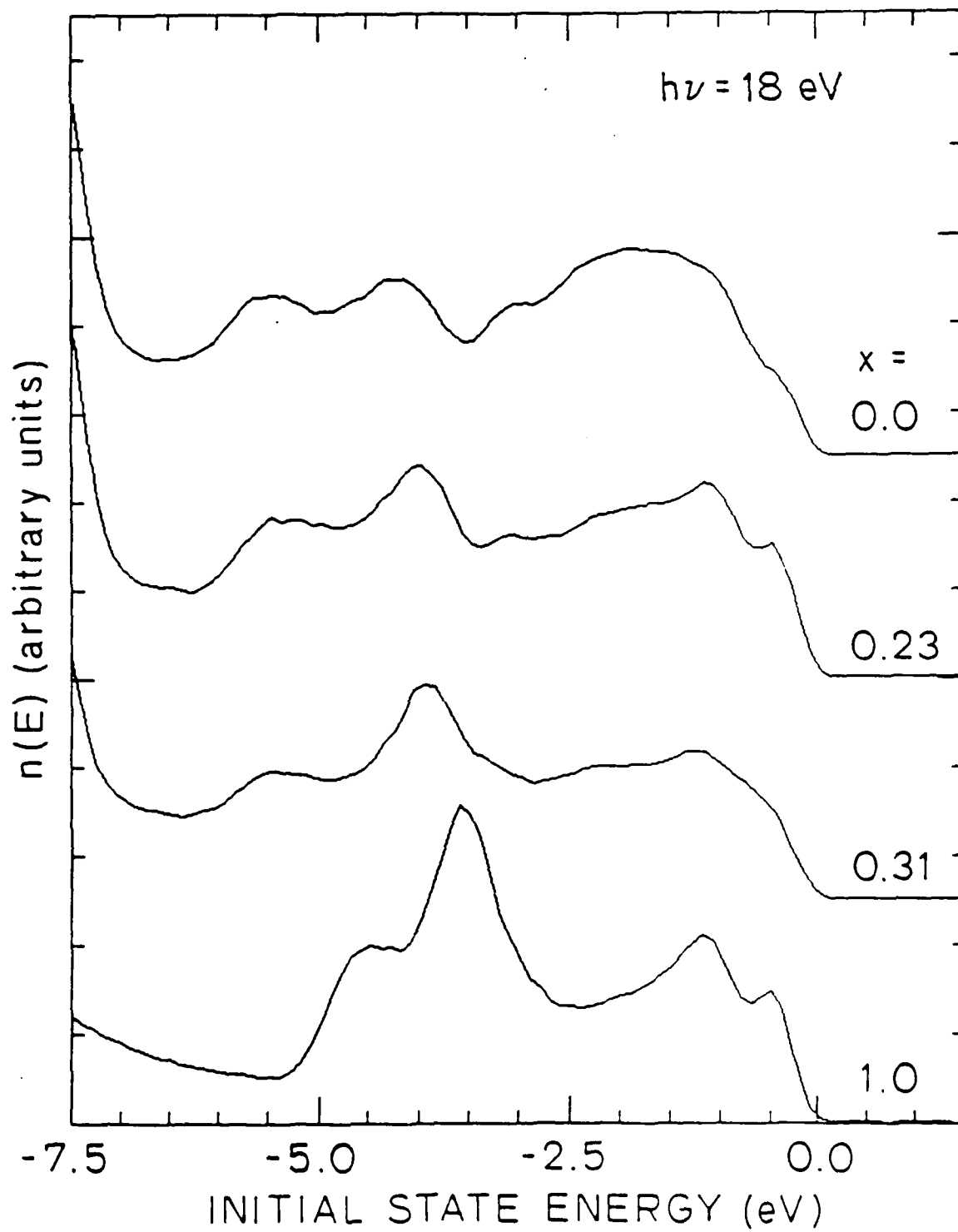
1. D. L. Smith, T. C. McGill, and J. W. Schulman, Appl. Phys. Lett. 43 (1983) 180.
2. C. Mailhot, Y. G. Wu, and T. C. McGill, presented Eleventh Annual Physics and Chemistry of Semiconductor Interfaces Conference, Pinehurst, N. C., Jan. 31-Feb. 2, 1984.
3. C. E. Moore, Atomic Energy Levels, Nat. Bur. Stand. (U.S. Cir. No. 467 U. S. G.P.O., Washington D. C.) 1949.
4. A. Kisiel and P. M. Lee, J. Phys. F 2 (1972) 395.
5. J. A. Silberman, P. Morgen, I. Lindau, W. E. Spicer, and J. A. Wilson, J. Vac. Sci. Technol. 21 (1982) 142.
6. W. A. Harrison, J. Vac. Sci. Technol. A1 (1983) 1672.
7. W. E. Spicer, J. A. Silberman, I. Lindau, A.-B. Chen, A. Sher, and J. A. Wilson, J. Vac. Sci. Technol. A 1 (1983) 1735.
8. Recent Reviews of ARPES are given by E. W. Plummer and W. Eberhardt, Adv. Chem. Phys. 49 (1982) 533; and F. J. Himpsel, Adv. in Physics 32 (1983)1.
9. Several examples of studies of metals and semiconductors are given in Refs. 8.
10. N. K. Allen, P. J. Durham, B. L. Gyorffy and R. G. Jordan, J. Phys. F 13 (1983) 223.
11. See for example, W. A. Harrison, Solid State Theory, Dover Publications, Inc. (New York, 1980) p. 90.
12. W. Eberhardt and F. J. Himpsel, Phys. Rev. B 21 (1980) 5592.
13. A. Ebina and T. Tokahashi, J. Cryst. Growth 59 (1982) 51.
14. M. Pessa, P. Huttunen, and M. A. Herman, J. Appl. Phys. 54 (1983) 6047.
15. F. Cerrina, J. R. Myron, and G. J. Lapeyre, Phys. Rev. B 29 (1984) 1798.
16. W. E. Spicer, J. A. Silberman, P. Morgen, I. Lindau, A.-B. Chen, A. Sher, and J. A. Wilson, Phys. Rev. Lett. 49 (1983) 948.
17. K. C. Mills, D. Denley, P. Perfetti, and D. A. Shirley, Sol. State. Comm. 30 (1979) 743.

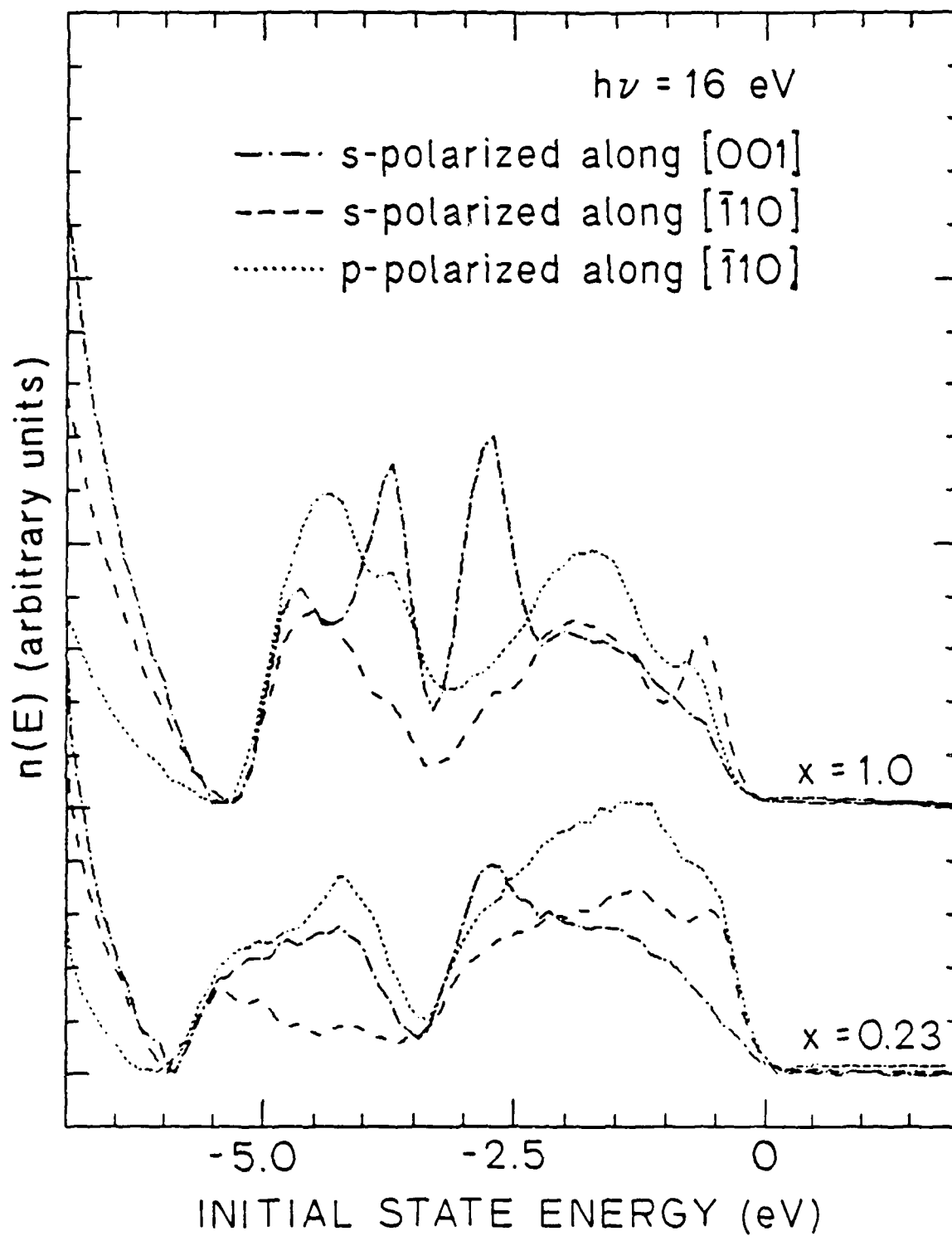
18. J. G. Nelson, W. J. Gignac, R. S. Williams, S. W. Robey, J. G. Tobin, and D. A. Shirley Surf. Sci. 131 (1983) 290.
19. T. C. Chiang, J. A. Knapp, M. Aono, and D. E. Eastman, Phys. Rev. B 15 (1980) 3513.
20. Shun-ichi Katsuki and Makoto Kunitmura, J. Phys. Soc. Jap. 31 (1971) 415.
21. H. Overhof, Phys. Stat. Sol. B 45 (1971) 395.
22. James R. Chelikowsky and Marvin L. Cohen, Phys. Rev. B 14 (1976) 556.
23. C. B. Duke, A. Paton, W. K. Ford, A. Kahn, and G. Scott, Phys. Rev. B 24 (1981) 3310.
24. M. Podgorny and M. T. Czyzyk, Solid State Comm. 32 (1979) 413.
25. Akiko Kubayashi, Otto F. Sankey, and John D. Dow, Phys. Rev. B 25 (1982) 6367.
26. A.-B. Chen and A. Sher, J. Vac. Sci. Technol. 21 (1982) 138.
27. K. C. Hass, H. Ehrenreich, and B. Velicky, Phys. Rev. B 27 (1983) 1088.

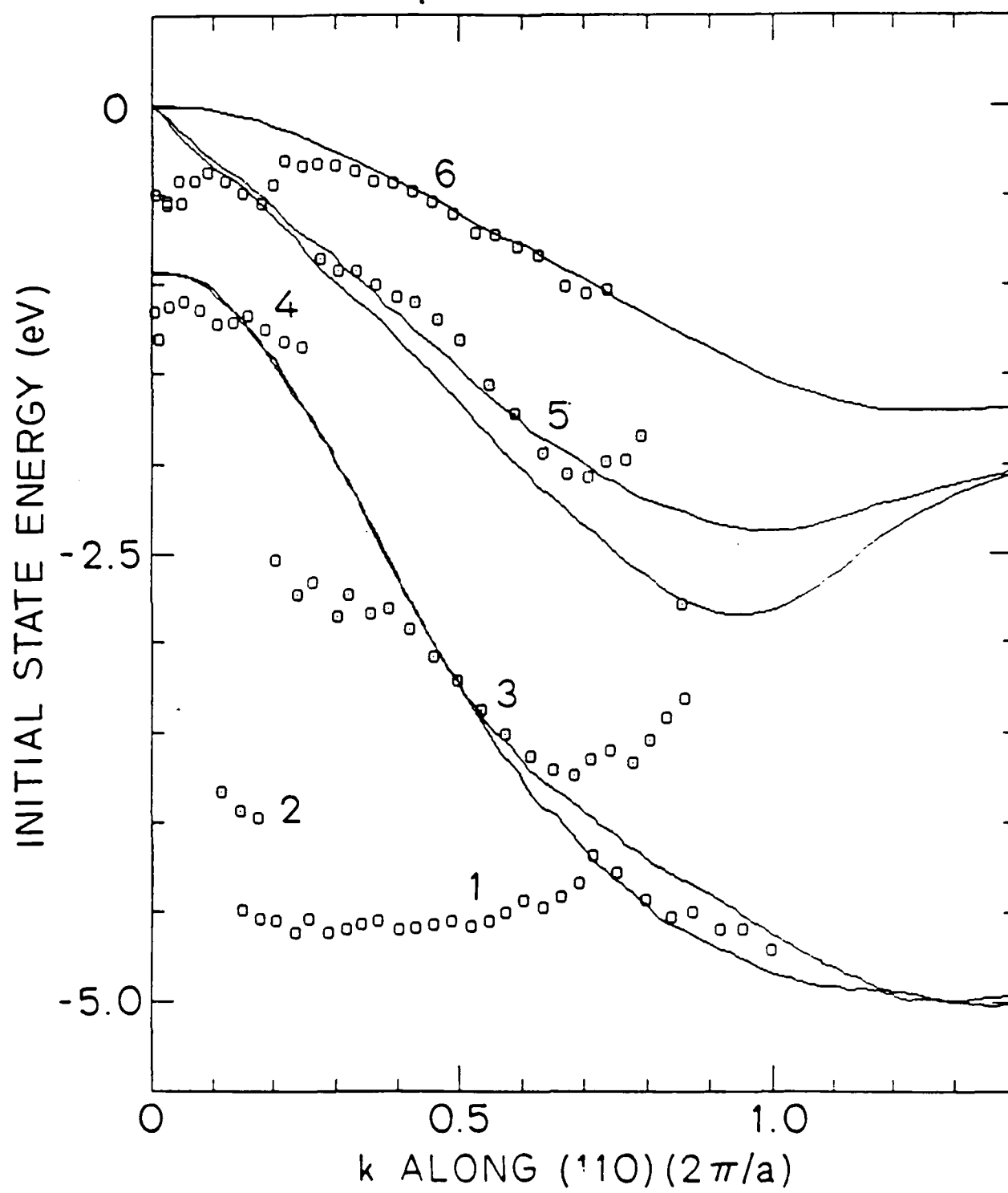
Figure Captions

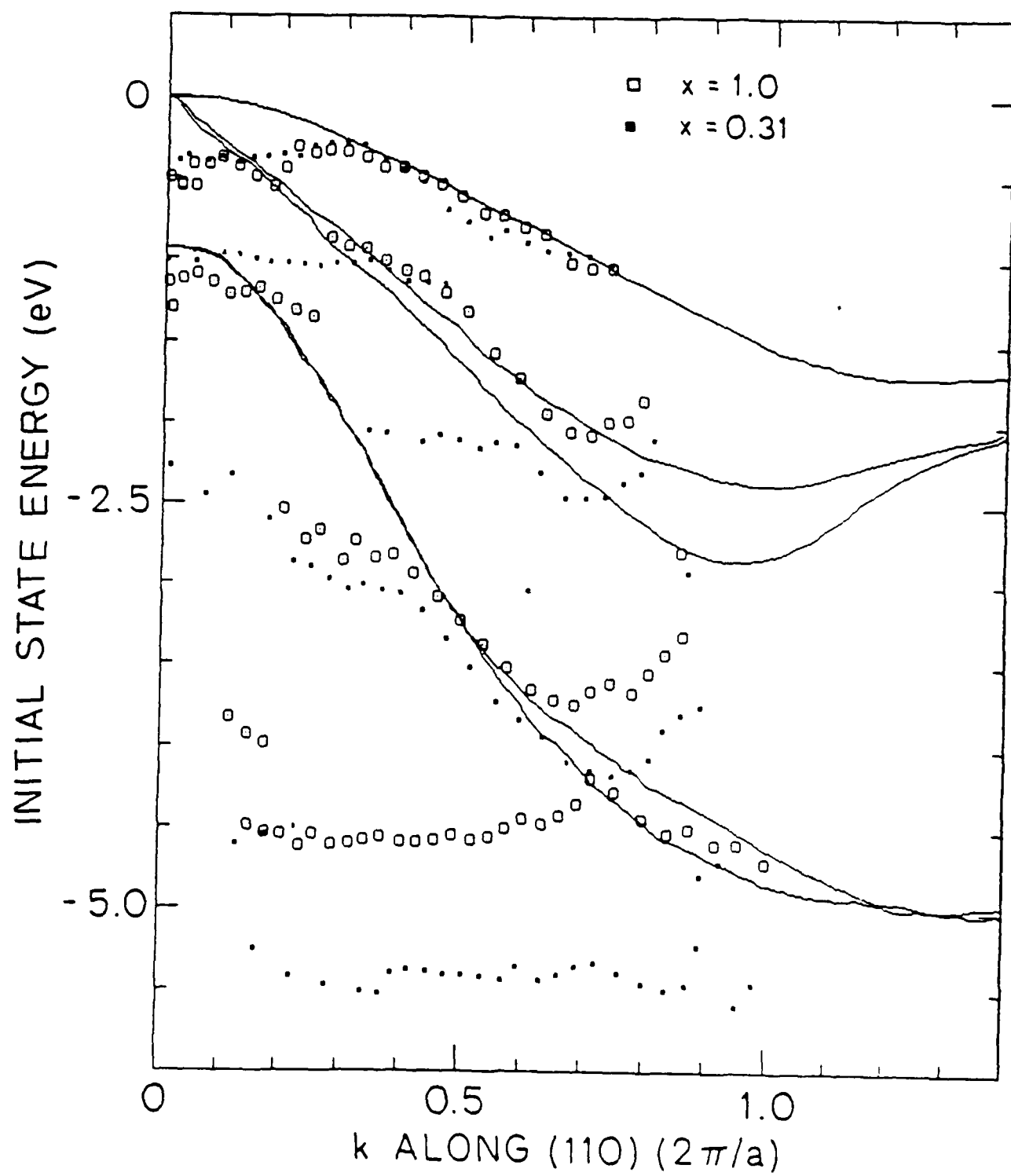
- Figure 1 ARPES spectra recorded along the normal to the (110) face of CdTe with $13 \leq h\nu \leq 27$ eV in 0.5 eV steps. The radiation was incident at 64° to the normal (stronger p-polarization) with the electric field direction along $[\bar{1}10]$.
- Figure 2 Comparison of normal emission spectra (p-polarization) taken at $h\nu = 18$ eV for the four $\text{Hg}_{1-x}\text{Cd}_x\text{Te}$ compounds studied. The curves show highly similar structure which tends toward higher binding energy with increasing Hg content.
- Figure 3 The symmetry of the initial states is reflected in the polarization dependence of the structure in the normal emission spectra at a given photon energy (16 eV). The enhancement of the peak near -2.7 eV and suppression of emission near the VBM with $h\nu$ polarized parallel to $[001]$ is observed in all samples (CdTe and $\text{Hg}_{0.77}\text{Cd}_{0.23}\text{Te}$ are shown.)
- Figure 4 Initial state dispersion relations for the normal emission data from CdTe derived assuming a free electron final state (points) are compared to the calculated bands of Ref. 22 (solid) in the (110) direction. See text for discussion of comparison.
- Figure 5 Initial state dispersion relations derived from the experimental features for CdTe (open points) and $\text{Hg}_{0.69}\text{Cd}_{0.31}\text{Te}$ (filled points) and, as a guide, the calculated bands for CdTe (Ref. 22). The addition of Hg increases the binding energy of most features; and the alloy potential disorder may reduce the measured dispersion of some peaks.











Section III-III

BOND-LENGTH RELAXATION IN $\text{Hg}_{1-x}\text{Cd}_x\text{Te}$ ALLOY

The alloy system $\text{Hg}_{1-x}\text{Cd}_x\text{Te}$ (MCT) exhibits unusual bond-length relaxation behavior. In most of the pseudo-binary alloys in which the bond-length difference of the two components is fairly large, such as $\text{Ga}_{1-x}\text{In}_x\text{As}$ or $\text{ZnSe}_{1-x}\text{Te}_x$, the behavior of the bond-length relaxation can be predicted by a simple radial force model (Appendix 1). In that model the bond-length relaxation is determined by minimizing the distortion energy which results from the deviation of the bonds from their "natural bond-lengths", where the "natural bond-lengths" are defined as the bond-lengths of the pure components. However, in the case of MCT in which the bond-lengths of the two components are nearly the same (within 0.3%), the effect considered in the previous model is small; the dominating factor comes from the coupling of the bonding state and the neighboring anti-bonding states, which is termed "metallization" in Harrison's bonding theory [1].

Harrison [2] showed that in calculating the bond energy of HgTe and CdTe , the metallization term which is neglected in the Bond Orbital Approximation is no longer small and cannot be neglected. In the MCT alloy the bonds have different local environments, and the metallization terms change depending on the neighboring atoms. We will show that the changes of the metallization terms are responsible for the behavior of the bond-length relaxation in MCT.

In Harrison's theory [1] the bond tension T is defined as the first derivative with respect to internuclear distance of all terms contributing to the bond energy excluding the overlap interaction. The bond-length is determined by the balance of the tension and the repulsion force.

Now let us consider an alloy $\text{Hg}_{1-x}\text{Cd}_x\text{Te}$ with x near 1. This is a dilute solution of Hg-Te in a CdTe host (Figure 1a). We will compare this with the Hg-Te bond in pure HgTe , (Figure 1b) and investigate the effect of the variation

of the metallization term with environment. The metallization terms contributing to the bond tension of the Hg-Te come from the couplings between the Hg-Te bonding state and its neighboring anti-bonding states; and the couplings between the neighboring bonding states and the Hg-Te anti-bonding state. In the alloy (Figure 1), the couplings through the Hg cation are identical to the case in the pure HgTe, and the couplings through the Te anions are different from the pure HgTe case. In pure HgTe the tension terms on the Hg-Te bond which arise from the couplings through the Te anion are: $3T_{ma11}$ [3], which is the coupling between the Hg-Te bonding state and the three neighboring Hg-Te antibonding states; and $3T_{ma1'1}$ which is the coupling between the neighboring Hg-Te bonding states and the Hg-Te anti-bonding state. Whereas in the MCT the tension terms on the Hg-Te bond which arise through the Te anion are: $3T_{ma12}$, the couplings between the Hg-Te bonding state and the neighboring Cd-Te anti-bonding states; and $3T_{ma1'2}$ which is the coupling between the neighboring Cd-Te bonding states and the Hg-Te antibonding state. Therefore, the change in the tension on the Hg-Te bond in MCT with respect to the pure HgTe is

$$\Delta T_m = 3 (T_{ma12} - T_{ma11} + T_{ma1'2} - T_{ma1'1})$$

These tension terms can be obtained by taking the first derivative of the coupling energies with respect to the Hg-Te bond length. These are given by:

$$T_{ma11} = -1/2 V_1^2 (1 - \alpha_{p2}) * \left\{ \frac{2 \alpha_{p1} \alpha_{c1}^2}{\epsilon_{a1} - \epsilon_{b1}} + \frac{2(1 + \alpha_{p1}) \alpha_{c1}^2 (V_2^2 + V_3^2)^{1/2}}{(\epsilon_{a1} - \epsilon_{b1})^2} \right\}$$

$$T_{ma12} = -1/2 V_1^2 (1 - \alpha_{p2}) * \left\{ \frac{2 \alpha_{p1} \alpha_{c1}^2}{\epsilon_{a2} - \epsilon_{b1}} + \frac{2(1 + \alpha_{p1}) \alpha_{c1}^2 (V_2^2 + V_3^2)^{1/2}}{(\epsilon_{a2} - \epsilon_{b1})^2} \right\}$$

$$T_{ma1'1} = -1/2 V_1^2 (1 + \alpha_{p1}) * \left\{ \frac{-2 \alpha_{p1} \alpha_{c1}^2}{\epsilon_{a1} - \epsilon_{b1}} + \frac{2(1 - \alpha_{p1}) \alpha_{c1}^2 (V_2^2 + V_3^2)^{1/2}}{(\epsilon_{a1} - \epsilon_{b1})^2} \right\}$$

$$T_{ma1}^{-2} = -1/2 V_{1-}^2 (1 + \alpha_{p2}) * \left\{ \frac{-2 \alpha_{p1} \alpha_{c1}^2}{\epsilon_{a1} - \epsilon_{b2}} + \frac{2(1 - \alpha_{p1}) \alpha_{c1}^2 (V_2^2 + V_3^2)^{1/2}}{(\epsilon_{a1} - \epsilon_{b2})^2} \right\}$$

where α_{pn} and α_{cn} are defined as the polarity and covalency for bond n ; ϵ_{an} and ϵ_{bn} are energy levels of anti-bonding state and bonding states of bond n ; V_2 and V_3 are covalent energy and polar energy of Hg-Te; and V_{1-} is the metallic energy of Te.

When we examine these formulae, we find that the behavior of ΔT_m is predominantly determined by the α_p 's. The polarity of Hg-Te is smaller than that of Cd-Te, i.e. $\alpha_{p1} < \alpha_{p2}$. One then finds $T_{ma11} < T_{ma12}$ and $T_{ma11} < T_{ma12}$ hence $\Delta T_m > 0$ for Hg-Te in the alloy. Similarly we will find that $\Delta T_m < 0$ for Cd-Te in the alloy. A positive ΔT_m for Hg-Te in the alloy predicts the bond-length will decrease from that in the pure Hg-Te. The opposite trend is predicted for Cd-Te in the alloy.

To calculate a numerical value of ΔT_m , precise atomic term values are needed. Once the value of ΔT_m is obtained, the final bond-length can be obtained in one of the following ways:

- (1) Use the experimental spring constant K of the bond. In this case

$$\Delta d = -\Delta T_m / k.$$
- (2) Plug the ΔT_m back into the balance equation $V_o(d) = T_d/4$ [1], where $V_o(d)$ is the overlap repulsion energy and proportional to d^{-4} .
- (3) Use numerical methods to find the bond energy vs. interatomic distance.

The bond-length and bond energy in the alloy can thus be obtained simultaneously.

The first method is only semiempirical. The second method does not require the experimental spring constant, and it results in a self-consistent theory. However, an expression for all the tension terms including the overlap repulsion

is required, and besides being computationally more tedious, only yields correct trends rather than accurate values. In the third method, expressions for each term contributing to the bond energy and use of a computer are required. On the other hand, this technique yields other useful bonding properties. Sher et al [4] have used the third method and obtained the result that for the case of dilute Hg-Te in the Cd-Te host, the bond-length of Hg-Te decreases by 0.02 Å ; for dilute CdTe in the HgTe host, the bond-length of Cd-Te increases by 0.02 Å .

The calculated numerical value of the bond-length variation suffers from difficulties in obtaining precise atomic term values. However, by understanding the physical terms which are responsible for the bond-length relaxation, we can predict the trend in MCT. The important result is that the shorter Hg-Te bonds become shorter and the already longer Cd-Te bonds are lengthened. This trend is opposite to that observed in III-V systems such as InGaAs, where the effects of metallization can be ignored. Future work will concentrate on the implications of the bond-length relaxation on the lattice stability and the bonding of a heterojunction interface.

References

1. W. A. Harrison, Phys. Rev. B, 27, 6 (1983) 3592.
2. W. A. Harrison, J. Vac. Sci. Technol. A 1, (1983) 1672.
3. In T_{ma11} 'the 'm' stands for this tension come from the metallization the 'a' stands for the coupling through the anion.
4. A. Sher, A-B Chen, W. E. Spicer, C-K Shih, Proceedings of the 1984 U.S. Workshop on the Physics and Chemistry of Mercury Cadmium Telluride to appear in J. Vac. Sci. Technol., Feb., 1985.

is shown in Figure 2a, where a high density of extrinsic stacking faults (ESF) is evident. Examination of the HgCdTe side of the heterojunction reveals a significant difference in damage behavior when compared to that of the CdTe. At this higher magnification, the defects in the HgCdTe were much harder to locate than in the CdTe. Very few defects are exhibited on this side of the heterojunction, where a representative area of the HgCdTe reveals no defects as shown in Figure 2b. The defects studied in the HgCdTe generally had little or no dissociation of the $1/6\langle 112 \rangle$ Shockley partials. Figure 2c shows an almost perfect 60° dislocation in the HgCdTe, where the arrow points down the extra $\{111\}$ half-plane. To the best of our knowledge, perfect 60° dislocations have not been observed in CdTe. ESF are also observed in the HgCdTe, a typical fault is shown in Figure 2d, but the separation between the two Shockley partial dislocations is always much smaller in this material than is observed in CdTe.

IV. Discussion

These results obtained from the TEM examination of ion beam milled HgCdTe and CdTe are unexpected and, at first glance, surprising. Because of its mechanical instability compared to CdTe, one might predict that the HgCdTe would exhibit higher defect densities than CdTe after being subject to identical milling conditions. In addition, the CdTe stacking fault energy (calculated to be $\approx 10\text{mJ/m}^2$ [14]) is predicated to be greater than that of HgCdTe on the basis of the usual effect of alloying on stacking fault energy in metals [15]. That there is a difference in the cation-Te bonding in the CdTe and HgCdTe as is indicated by experimental [7] and theoretical considerations [16,17] is supported by these observations.

The extremely high defect density in the ion milled CdTe is not surprising since this magnitude of damage is typically observed by Yamashita

general distribution of native and induced defects in the two materials was examined at low magnification using conventional 2-beam imaging. Since the HgCdTe and CdTe are ion milled under identical conditions during the final thinning step, a direct comparison of the density, distribution and nature of the ion bombardment induced defects can be made between HgCdTe and CdTe. In addition, the HgCdTe/CdTe heterojunction can be examined. Figure 1 shows typical defect structures in the HgCdTe, CdTe, and interfacial region, respectively. These micrographs reveal a quite surprising result: under identical ion beam milling conditions, the CdTe contains a much higher density of defects (2-3 orders of magnitude) than the adjacent HgCdTe. Figure 1a reveals that the defects in the HgCdTe side of the heterojunction consist of single-line dislocations (located at A) and occasional dislocation loops (located at B). The defect density increases over several microns to the heterojunction where it abruptly increases in the interfacial region, as seen in Figure 1c. The long line dislocations are seen to pile up at the interface on the HgCdTe side of the metallurgical junction, and the damage induced defect loops increase in density from the HgCdTe towards the junction. In the interfacial region, these loops greatly increase in density and become smaller. This high density stays approximately constant into the CdTe substrate, as shown in Figure 1b.

Invaluable insight into the nature of the ion beam induced defects can be obtained from high resolution images taken from these regions. Lattice images of the heterojunction region taken normal to the {110} plane and looking down the {111} planes are shown in Figure 2. Inspection of the CdTe side of the heterojunction reveals a very high density of dissociated 60° dislocations and interstitial loops, consistent with the above observations on their density. A representative area of the CdTe

nique should be feasible for HgCdTe if low ion beam energies are employed and the sample is cooled to liquid nitrogen temperatures [11]. With such TEM samples, investigations into native defect distribution and elemental composition profiles in epitaxial HgCdTe grown on CdTe and alternate substrates may be performed. It is hoped that additional bonding information can be obtained in these studies. This paper will report on a preliminary TEM investigation supplementing our ongoing study of the bonding nature of HgCdTe.

II. EXPERIMENTAL

Cross-sectional TEM (XTEM) specimens were prepared from a sample of HgCdTe ($x = 0.3$) grown by LPE on a {111} CdTe substrate. The LPE material was grown from a Te melt to a layer thickness of $14.3 \mu\text{m}$. Most of the material used in this study was supplied by Santa Barbara Research Center (SBRC); however, studies in Rockwell samples give similar results. Employing a XTEM specimen technique similar to that of Yamashita on samples of thin films grown on CdTe [12], XTEM specimens suitable for viewing down the plane of the heterojunction interface were prepared. The samples were oriented such that a $\langle 110 \rangle$ direction lay normal to the plane of sample, so that little tilting was needed to align the electron beam with the $\langle 110 \rangle$ zone axis for high resolution lattice imaging [13]. Final thinning was achieved by ion milling at room temperature to perforation using Ar^+ at 4 keV with a $35 \mu\text{A-mm}^{-2}$ beam current incident at 15° for several hours. Examination of the samples was made using a Philips EM400ST having a high resolution objective lens.

III. Results

Using the Energy dispersive analysis of X-rays (EDX) facility the interfacial region between the HgCdTe and CdTe was located, and the

defect properties exhibited in this LPE heterojunction suggest that an unusual interface kinetics and/or chemistry exist in this system. In light of the results mentioned above, a question may be raised as to the importance of lattice match at the HgCdTe/CdTe interface. Instead, questions of chemical driving forces across the interface may be critical. For example, the unusual bonding of HgCdTe provides a possible driving force for moving Cd from CdTe into HgCdTe [7,8]. Many scientific clues into the mechanisms of the bonding in the alloy may exist in this heterojunction. By studying this heterojunction in depth, it is hoped that a more fundamental understanding into the nature of the bonding in this alloy may be obtained.

Transmission electron microscopy (TEM) is a useful tool for direct defect structural visualization and X-ray compositional analysis. Preparation of TEM specimens requires thinning techniques such as ion beam milling. Ion milling is particularly useful on the preparation of cross-sectional samples, which are useful in studying defect structures at interfaces or defect distributions associated with ion implanted material. While cross-sectional TEM has been successfully employed to great effect in the elemental [9] and III-V [10] semiconductors, difficulties have been encountered in implementing this technique to the HgCdTe system due to the damage introduced into the crystals during ion milling. This induced damage tends to mask the original defect structure and hence impede native defect structural analysis. Insight into the nature of the bonding in the alloy might be gained, however, if the ion milling defects are studied.

Recently, progress in refining the ion milling technique for application to HgCdTe has been made, and preliminary reports indicate that this tech-

I. INTRODUCTION

In order to exploit the attractive electronic capabilities of the $\text{Hg}_{1-x}\text{Cd}_x\text{Te}$ alloy system, detailed defect structural characterization of this material must be undertaken. As outlined by Cheung [1] in these proceedings, numerous studies have shown that the electronic behavior of the alloy is linked to the mechanical defect structure introduced during the growth and processing of the material. Potential device performance is often impeded by the presence of this defect structure. Of extreme interest are those defects associated with interfaces, and in particular, the defect structure that arises at the liquid phase epitaxial (LPE) HgCdTe grown on CdTe heterojunction.

Some of the compositional and structural properties that characterize this heterojunction are unique among LPE heterojunction systems. The transition region width between the HgCdTe and the CdTe substrate has been shown to be primarily a function of the quality of the CdTe surface preparation; but even the best quality LPE $\text{HgCdTe}/\text{CdTe}$ heterojunctions are characterized by transition widths on the order of one micron [2,3]. What are the fundamental mechanisms leading to such a great transitional width? For comparison, typical LPE heterojunction widths, such as the $\text{AlGaAs}/\text{GaAs}$ system, are on the order of 100 Å [4]. The lattice mismatch in that system is roughly one-third of that on the $\text{HgCdTe}/\text{CdTe}$ system, but the LPE transition width is approximately 100 times less than that in the LPE $\text{HgCdTe}/\text{CdTe}$. In addition, analysis of the $\text{HgCdTe}/\text{CdTe}$ LPE heterojunction shows an integrated misfit dislocation intensity in the so-called misfit zone that is much greater than can be explained by lattice mismatch between the HgCdTe and CdTe [2,5]. These misfit dislocations are not completely confined to the $\{111\}$ growth plane in the HgCdTe side of the heterojunction [6]. The unique structural

Section III-IV

TEM INVESTIGATION OF THE DIFFERENCES IN ION MILLING INDUCED DAMAGE
OF $\text{Hg}_{1-x}\text{Cd}_x\text{Te}$ AND CdTe HETEROJUNCTIONS

G. P. Carey, S. Cole^a, T. Yamashita, J. A. Silberman^b, and W. E. Spicer^c

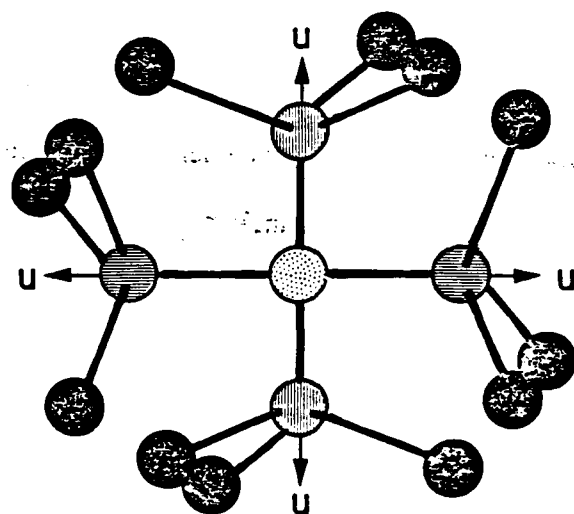
Stanford Electronics Laboratories
Stanford University, Stanford, CA 94305

J. A. Wilson

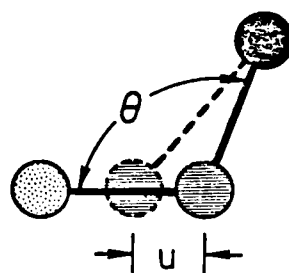
Santa Barbara Research Center
Goleta, CA 93017

Abstract

The lattice defects induced by ion milling at the liquid phase epitaxy (LPE) grown HgCdTe on CdTe heterojunction have been investigated using transmission electron microscopy (TEM). TEM analysis reveals that subjecting both materials to identical milling conditions results in much higher defect densities (2-3 orders of magnitude) in the CdTe than in the HgCdTe ($x = 0.30$). In addition, high resolution lattice images of both regions reveal that the stacking fault widths in the HgCdTe are much narrower than in the CdTe, which implies that the stacking fault energy is much higher in the HgCdTe as compared to the CdTe. These observed phenomena are shown to support the weakness and metallicity of the Hg-Te bond as proposed by theoretical considerations.



a)



b)

Figure Captions

Figure 1 (a) An Indium atom substitutes for Gallium in GaAs; the tetrahedral symmetry is preserved at the In atom.

(b) The displacement of As atoms, u , results in the Ga-As bonds being decreased by $u \cos \theta$. The In-As bond lengths are varied by $d_{\text{GaAs}} + u - d_{\text{InAs}}$

Acknowledgement

We thank Dr. Alex Zunger for valuable discussions.

References

1. J. C. Mikkelsen, Jr., and J. B. Boyce, Phys. Rev. B 28, 7130 (1983).
2. J. C. Mikkelsen, Jr., and J. B. Boyce, Bulletin of American Physical Society 29, #3, AB-1 (March, 1984).

$$E = 4 \left\{ \frac{k}{2} (d_{\text{GaAs}} - d_{\text{InAs}} + u)^2 + 3 \frac{k}{2} (u/3)^2 \right\}$$

By minimizing the energy with respect to u we obtain

$$u = 3/4(d_{\text{InAs}} - d_{\text{GaAs}}),$$

or the deviation of the In-As bond-length

$$\Delta d_{\text{InAs}} = 1/4 (d_{\text{GaAs}} - d_{\text{InAs}}).$$

Similarly the bond length deviation of dilute Ga-As in an InAs host is

$$\Delta d_{\text{GaAs}} = 1/4 (d_{\text{InAs}}^I - d_{\text{GaAs}}).$$

This predicts exactly Mikkelsen and Boyce's result [1]. Note that this displacement leaves all metallic atoms in their original sites; only the As atoms move. To a good approximation this is true in the concentrated alloy where the metal atoms form a face center cubic lattice of the weighted average lattice parameter and the As atoms move to fit local bond lengths.

One can apply this principle to the rocksalt structure systems; e.g. $\text{K}_{1-x}\text{Rb}_x\text{Br}$, and predict that the bond-length deviation of the solute in the dilute solution is half of the difference between the two components.

$$\Delta d_{\text{KBr}} = 1/2(d_{\text{RbBr}} - d_{\text{KBr}})$$

$$\Delta d_{\text{RbBr}} = 1/2(d_{\text{KBr}} - d_{\text{RbBr}})$$

However, because of the lattice geometry, the approximation that all the cations stay in their original sites might not be as good. In rocksalt structure, the restoring force on the displaced first neighbor results from the atom right behind the first neighbor; one would expect that the relaxation extends more than one interatomic distance and the value of the bond-length deviation would be somewhat smaller than what is predicted by this model. This agrees with the experimental result [2].

In calculating pseudo-binary alloy properties, the nearest neighbor distance is a very important parameter. For many years people have used the Virtual Crystal Approximation (VCA) which assumes that all atoms occupy the average lattice positions. In 1982 Mikkelsen and Boyce used Extended X-ray Absorption Fine Structure (EXAFS) to study the atomic scale structure of the $\text{Ga}_{1-x}\text{In}_x\text{As}$ system [1]. They found that the Ga-As and In-As bond lengths did not follow the VCA; instead, they only slightly deviated from their natural bond lengths even in the dilute solutions, and the magnitude of the bond-length deviation at the dilute limit was about a quarter of the difference of the natural bond lengths of the two components (GaAs and InAs). These results can be explained by a simple radial force constant model in which the weaker angular forces are neglected.

Consider a compound GaAs in which one of the Ga atoms is replaced by an In atom. This configuration represents the dilute limit of In-As in a GaAs host (see Figure 1). In this configuration, four In-As bonds are identical and the tetrahedral symmetry is preserved at the In atom. We regard any difference between Ga and In as a first order difference. Let us call d_{GaAs} the natural bond length of the host and K the stretching force constant for the host. Adding In will change K by an amount we regard as first order, but that alone will not give the distortion. However, because the natural bond length of InAs, d_{InAs} , is larger than d_{GaAs} by a first order amount the As atoms around the In impurity move outward by a first order distance; we hold the second neighbors fixed and to first order can take K to be the value for the host. Let us call u the outward relaxation displacement of the As: Then Δd_{InAs} , the amount that the final In-As bond length deviates from d_{InAs} , is $d_{\text{GaAs}} - d_{\text{InAs}} + u$. The bond lengths of the neighboring Ga-As are decreased by $-u \cos \theta$ equal to $-u/3$ to first order. The energy associated with this distortion is

BOND-LENGTH RELAXATION IN PSEUDO-BINARY ALLOYS†

C. K. Shih
W. E. Spicer*
W. A. Harrison

Stanford University, Stanford, CA 94305

Arden Sher

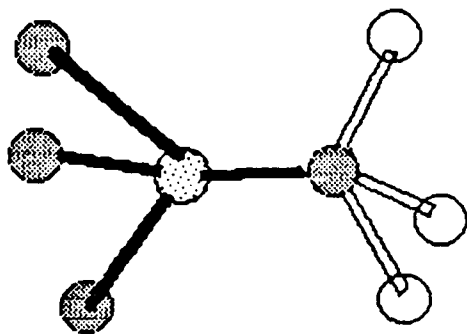
SRI International, Menlo Park, CA 94025

ABSTRACT

The bond-length relaxation in pseudo-binary alloys can be predicted by a simple radial force model. In tetrahedral structure alloys the bond length deviation of the solute in the dilute solution is a quarter of the bond-length difference between the two components. This result agrees with the experimental work done on the $\text{Ga}_{1-x}\text{In}_x\text{As}$ system performed by Mikkelsen and Boyce.

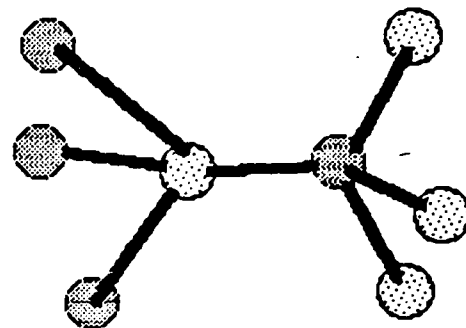
† This work was supported by DARPA under contract 800989-88

* Stanford Ascherman Professor of Engineering



Hg-Te in MCT

Figure 1a



Hg-Te in pure HgTe

Figure 1b

Figure Captions

Figure 1a,b Dark circles represent Te atoms, circles with dots in them
 represent Hg atoms, and open circles represent Cd atoms.

in work done on CdTe [12], but the relatively low resulting damage to the HgCdTe lattice is quite unexpected. In fact, this low defect density is suggestive of a metallic-like recovery behavior in the HgCdTe. Cole et al. [18] showed that the room temperature hardness of HgCdTe ($x \approx 0.3$) and CdTe are similar, suggesting that the rate of glide of dislocations is similar in the two materials. Therefore the differences in the observed defect structures on either side of the junction is not attributed to the differences in the glide behavior.

The difference in the distribution of defects in this ion milled HgCdTe/CdTe heterojunction may be understood by considering the mechanism of climb in these two materials. The lattice images from both of these regions reveal that there is a smaller dissociation of the $1/6\langle 112 \rangle$ Shockley partial dislocations in the HgCdTe relative to the CdTe. Since climb occurs by a diffusion-controlled process in which vacancies or constituents must diffuse to the dislocation core, the climb of the narrower stacking faults and perfect 60° dislocation in the HgCdTe should be much easier. This implies that the rate of recovery would be much higher in the HgCdTe than in the CdTe, as is observed.

This recovery mechanism might also be aided by the large density of point defects present in the ion bombarded HgCdTe lattice arising from the weak Hg-Te bond [17] and the consequent ease of formation of the cation vacancy attributed to the weakly bound Hg [8,16]. Hence this "Hg vacancy" mechanism is consistent with these theoretical calculations. Thus it is possible that both materials undergo comparable damage during ion milling, but that the presence of a high density of induced "Hg vacancies" along with the narrower stacking faults in the HgCdTe enhance the recovery rate in this material over that of CdTe. One must also ask whether the ease

of movement of dislocations in HgCdTe may contribute to the extreme ($> 1 \mu\text{m}$) heterojunction width in the HgCdTe regions of the HgCdTe/CdTe heterojunctions.

V. SUMMARY

Preliminary analysis of the ion bombarded induced defects in HgCdTe/CdTe heterojunctions using XTEM yield interesting phenomena which manifest the differences in the cation-Te bonding occurring in HgCdTe and CdTe. Under identical ion milling conditions, the CdTe contains much higher resulting damage (2-3 orders of magnitude more defects) in the form of small interstitial or vacancy loops compared to HgCdTe. Lattice images reveal that the separation of the Shockley partials is in general much less in the HgCdTe than in the CdTe. These observations suggest that the HgCdTe undergoes a much higher rate of recovery than the adjacent CdTe, where the narrower stacking faults would tend to quicken the rate of climb of the defects and consequently lead to an increased rate of annihilation. This mechanism would be enhanced by the high density of point defects in the form of "Hg vacancies" that would be present in the ion bombarded HgCdTe due to the weak Hg-Te bond. Hence, these observations support the theoretical work which predicts a weak Hg-Te bond and consequent ease of formation of the "Hg vacancy" in the alloy.

Acknowledgements

This work supported by DARPA under contract No. 916610-B5. Use of the TEM of the Department of Materials Science is also greatly appreciated.

- a) Permanent Address: Department of Metallurgy and Materials, University of Birmingham, Birmingham, England
- b) Fannie and John Hertz Foundation Fellow
- c) Stanford Ascherman Professor of Engineering

References

1. D. T Cheung, J. Vac. Sci. Technol. A (these proceedings)
2. T. J. Magee, private communication.
3. P. M. Raccach, U. Lee, J. Vac. Sci. Technol. A 1, 1587 (1983).
4. C. M. Garner, C. Y Su, and W. E. Spicer, J. Vac. Sci. Technol. 16 (5) 1521 (1979).
5. S. Cole, G. P. Carey, W. E. Spicer, unpublished work.
6. G. R. Woolhouse, T. J. Magee, H. A. Kawayoshi, C. S. H. Leung, and R. D. Ormand, J. Vac. Sci. Technol. A (these proceedings).
7. W. E. Spicer, J. A. Silberman, I. Lindau, A.-B. Chen, A. Sher, J. A. Wilson J. Vac. Sci. Technol. A 1, (3) 1795 (1983).
8. A. Sher, A.-B. Chen, W. E. Spicer, and C.-K. Shih, J. Vac. Sci. Technol. (these proceedings).
9. A. G. Culles, H. C. Webber and N. G. Chew, Proc. 10th Ann. Congress on Electron Microscopy, Hamburg 385 (1982).
10. P. M. Petroff, J. Vac. Sci. Technol. 14, 973 (1977).
11. S. Wood, J. C. Gregg, Jr., R. F. C. Farrow, W. J. Takei, to be submitted to J. Appl. Phys.
12. T. Yamashita, Ph.D. thesis (to be published).
13. T. Yamashita, F. A. Ponce, P. Pirouz and R Sinclair, Philos. Mag. A 45, 693 (1982).
14. E. L. Hall and J. B. Vander Sande, Philos. Mag. A 37, 137 (1978).
15. J. W. Christian and V. Vitek, Rep. Prog. Phys. 33, 307 (1970).
16. W. A. Harrison, J. Vac. Sci. Technol. A 1, (3) 1672 (1983).
17. A.-B. Chen, A. Sher, W. E. Spicer, J. Vac. Sci. Technol. A 1, (3) 1674 (1983).
18. S. Cole, M. Brown, and A. F. W. Willoughby, J. Mater. Sci. 17, 2061 (1982).

Figure Captions

Figure 1(a) Conventional 2-beam image of the ion-milled HgCdTe, showing line defects (A) that were believed to be present in the LPE material, and small dislocation loops (B) that were introduced during ion milling.

(b) TEM micrograph of the CdTe substrate side adjacent to the heterojunction, showing large densities of small loops, and long-line native defects.

(c) 2-beam image of the interfacial region clearly showing the difference in ion beam milling damage in both sides of the metallurgical junction.

Figure 2(a) TEM high resolution lattice image taken on the CdTe side of the heterojunction. This representative area is seen to possess a high density of extrinsic stacking faults (ESF).

(b) Lattice image taken from a representative area on the HgCdTe side of the heterojunction showing no defects.

(c) Lattice image showing an almost perfect 60° edge dislocation in the HgCdTe side of the heterojunction. The arrow points down the extra half-plane.

(d) Lattice image showing ESF in the HgCdTe. The widths of the ESF in the HgCdTe were generally much less than in the CdTe.

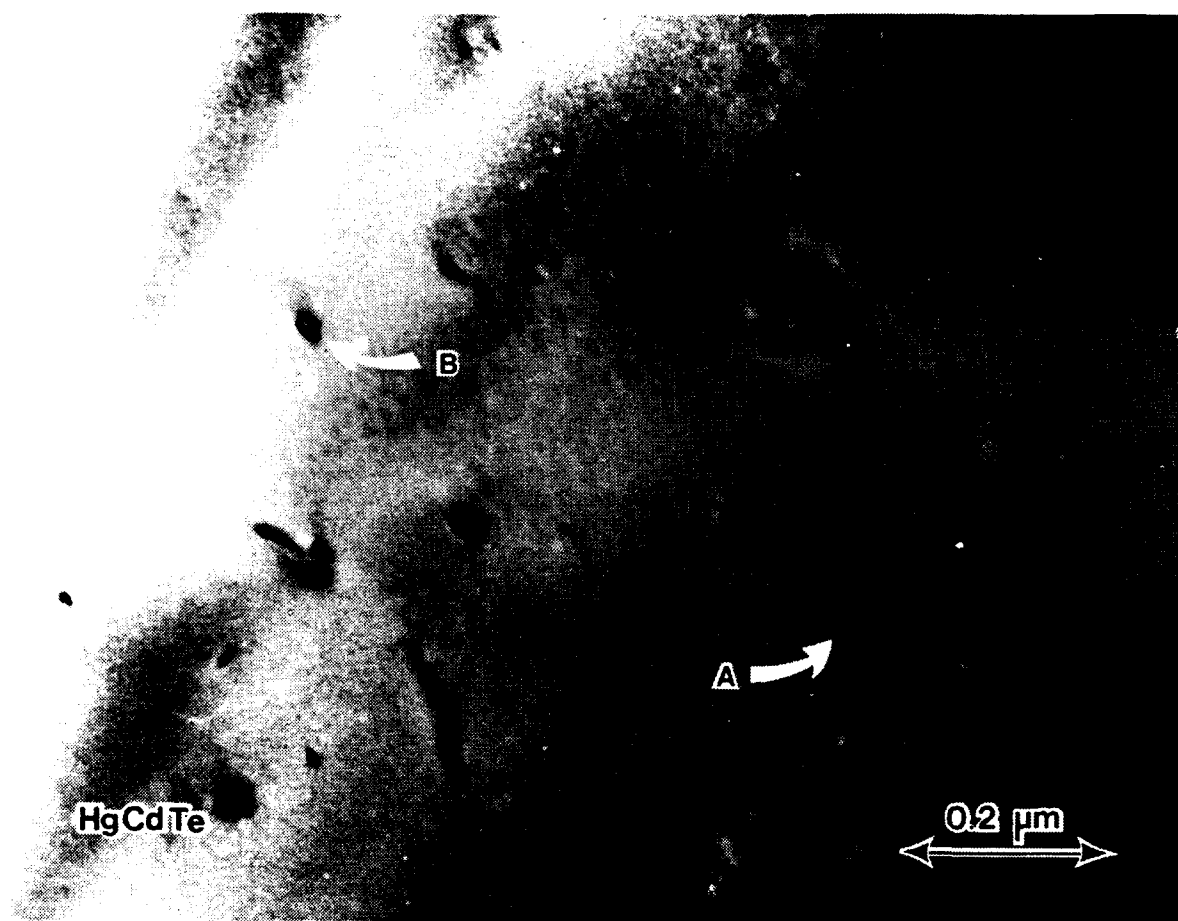


Figure 1a

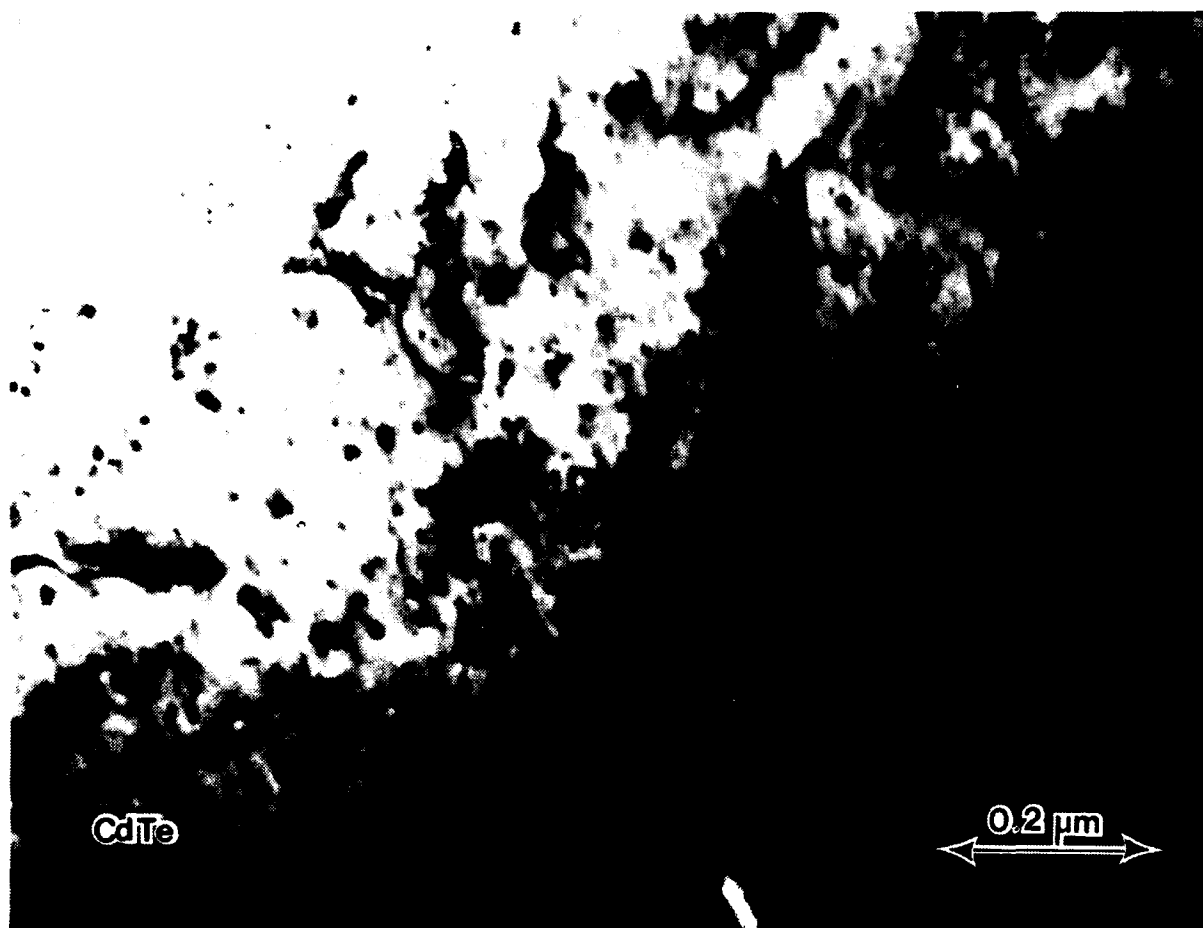


Figure 1b

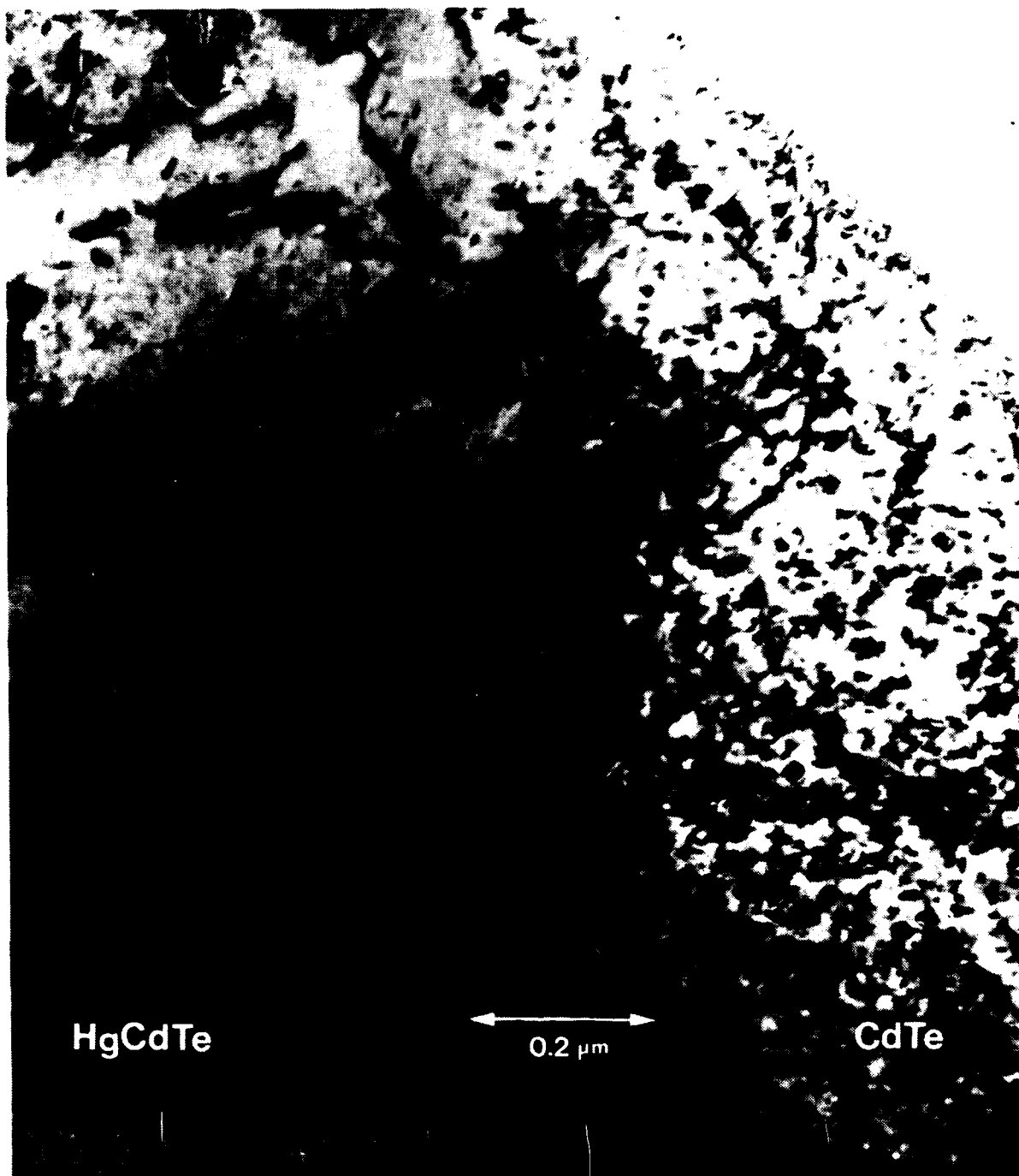


Figure 1c

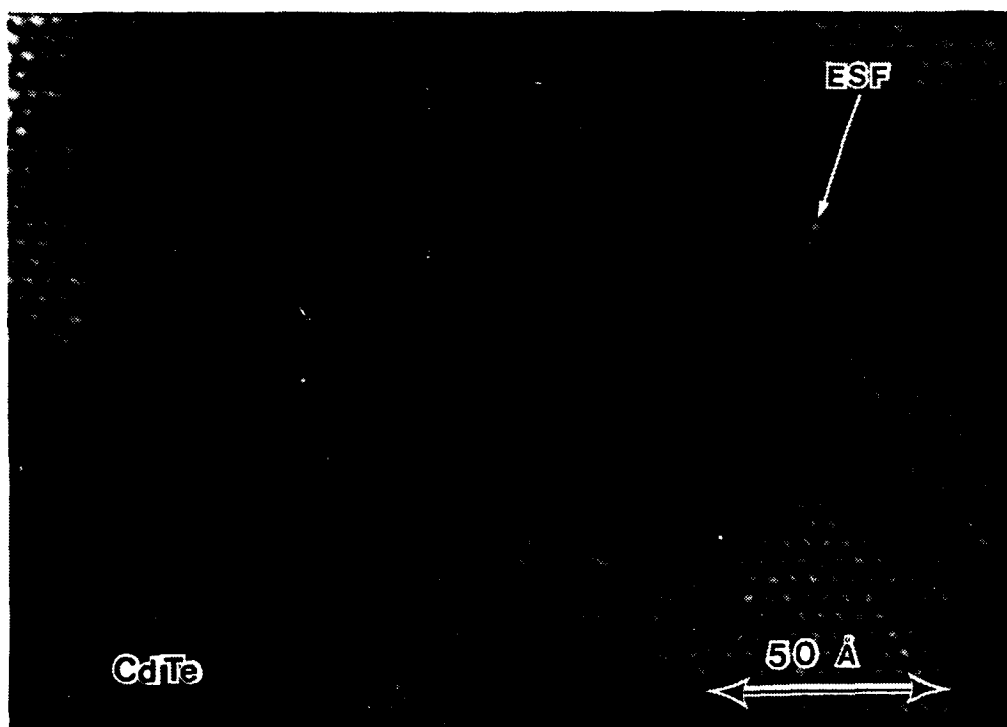


Figure 2a (layer area then original)

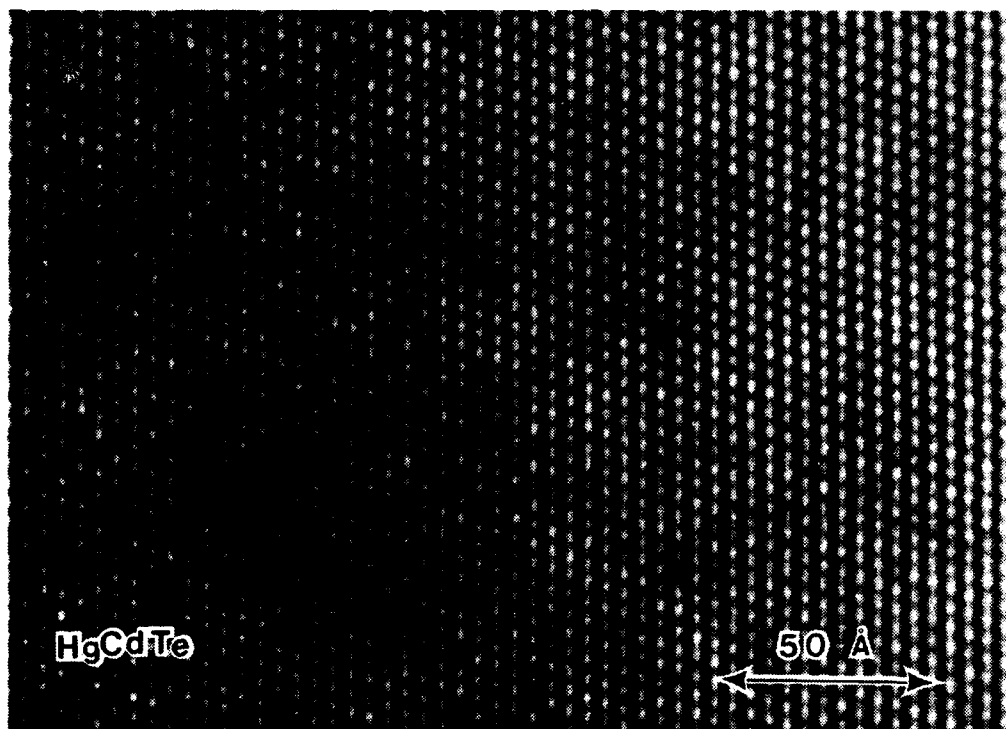


Figure 2b (layer area then original)

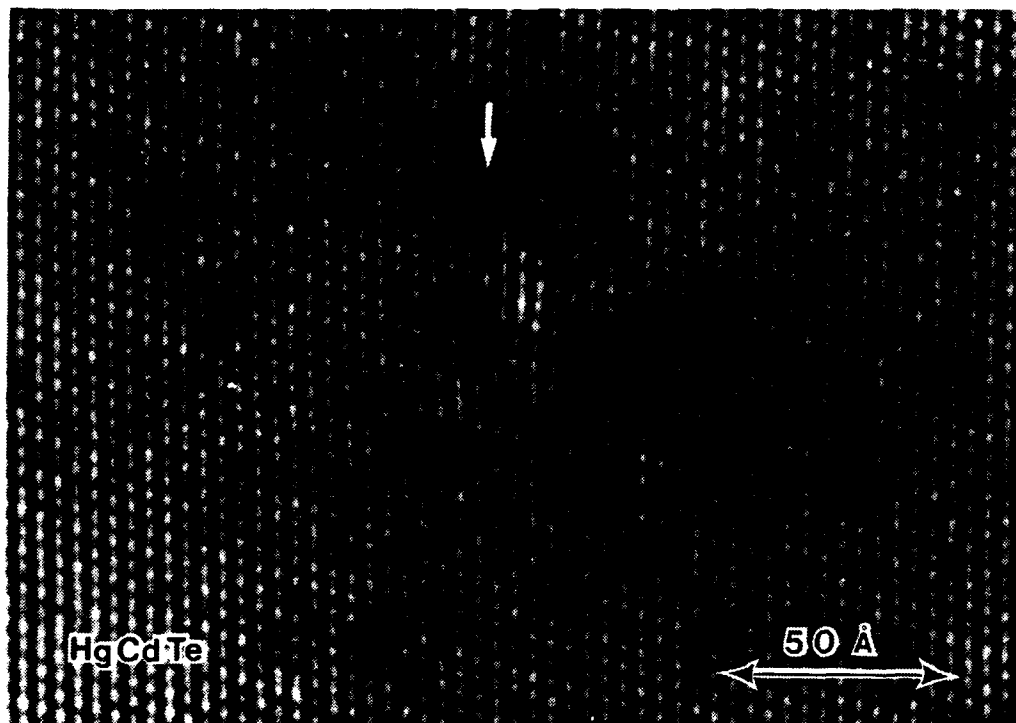


Figure 2c

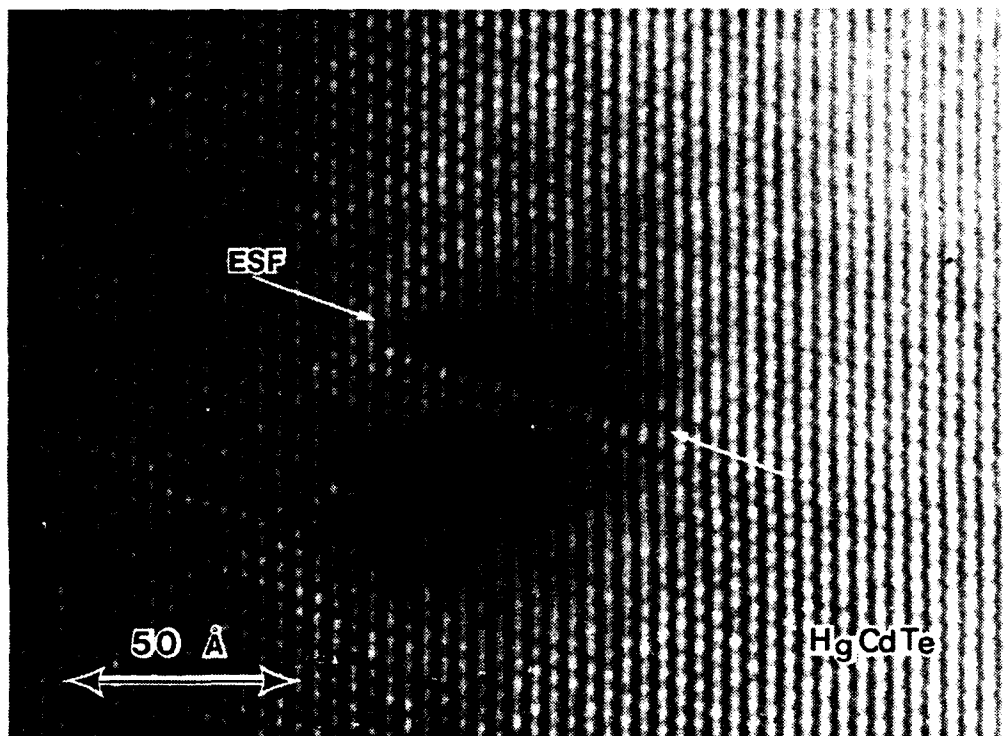


Figure 2d

Section III-V

COMPARATIVE STUDY OF ACTIVATED OXYGEN UPTAKE ON HgTe, $\text{Hg}_{0.69}\text{Cd}_{0.31}\text{Te}$, AND CdTe

J. A. Silberman,^a D. Laser^b, I. Lindau, and W. E. Spicer^c
Stanford Electronics Laboratory, Stanford University
Stanford, CA 94305

J. A. Wilson
Santa Barbara Research Center, Goleta, CA 93017

ABSTRACT

Soft-X-ray photoemission spectroscopy was used to monitor the uptake of oxygen on the (110) faces of HgTe, $\text{Hg}_{0.69}\text{Cd}_{0.31}\text{Te}$, and CdTe during the formation of roughly two monolayers of oxide. The oxidation was activated by a hot filament in line-of-sight of the sample surface. The oxides formed contain Cd and Te; whereas, Hg is lost from the surface during the initial stages of oxide formation. The rate of oxidation for the $\text{Hg}_{0.69}\text{Cd}_{0.31}\text{Te}$ sample was found to be 69% as great as that for the binary HgTe and lower than observed for CdTe. The scaling of oxidation rate with the number of Hg-Te bonds between HgTe and the $x = 0.31$ alloy together with the observed release of Hg upon oxidation suggests the importance of breaking the Hg-Te bond as a step in the oxidation process. Evidence for an unstable character of the oxide on the Hg containing compounds is also presented.

a) Fannie and John Hertz Foundation Fellow

b) Present address: Ministry of Defense, P. O. Box 2250, Haifa, Israel

c) Stanford W. Ascherman Professor of Engineering

I. Introduction

In addition to its relevance to passivation processes, study of the oxidation of $\text{Hg}_{1-x}\text{Cd}_x\text{Te}$ can afford insights into the manifestation of the alloy electronic structure in the chemical activity of the surface. Experimental [1] and theoretical [2] studies of the alloy electronic structure indicate distinct Hg and Cd contributions to the valence states 4 to 6 eV below the valence band maximum, implying a difference in the bonding of Cd and Hg in the lattice. The bond in HgTe is considerably more metallic and weaker than the bond in CdTe [3]. Upon alloy formation, a net charge transfer from Cd to Hg takes place, as evidenced by shifts in the binding energy of the Hg 5d and Cd 4d core level photoemission peaks [4] and chemical shifts measured as a function of composition in nuclear magnetic resonance data [5]. Such a charge rearrangement results in a higher electron density near the Hg and a stronger Cd-Te bond in the alloy at the expense of the bond of Hg to Te [4,6]. These features of the alloy electronic structure may be expected to influence the oxygen chemistry of the surface through modification of the kinetics of reactions which occur or by determining the nature of the oxide formed. A comparative investigation of the activated uptake of oxygen on atomically clean (110) surfaces for CdTe, HgTe, and $\text{Hg}_{0.69}\text{Cd}_{0.31}\text{Te}$ was undertaken to explore the effects of alloy formation on the surface properties of the binary constituents. A portion of this data will be presented here to illustrate central aspects of the oxidation, such as the observed instability of the oxide formed; a more complete exposition of the findings will be published separately.

II. Experimental

Samples of HgTe and $\text{Hg}_{0.69}\text{Cd}_{0.31}\text{Te}$, grown by solid state recrystallization, were transferred through an air lock into the vacuum system after

baking to avoid heating the specimens. Clean surfaces of these materials and a bar of CdTe (II-VI, Inc.) were prepared by cleaving in vacuum ($p \sim 5 \times 10^{-11}$ torr) prior to initiating the oxidation sequence.

The oxidation was carried out in the small evacuated volume from which the samples had been originally transferred after separately baking this portion of the apparatus to reduce the pressure and water content. In this respect the oxidation process was similar to that reported previously [7]. To stimulate the otherwise extremely slow uptake of oxygen [7] an unbiased hot thoriated iridium filament was positioned in line-of-sight of the sample surface during the exposure. The oxygen pressure was monitored by a millitor ionization gauge (Varian Associates) not in direct line-of-sight of the sample, and the pressure regulated at a fixed value of 5×10^{-5} Torr. Before beginning the oxidation study, it was ascertained that only the combination of oxygen and the hot filament in front of the sample resulted in the reactions reported; operation of the out-of-line-of-sight gauge in oxygen or use of the hot filament in the absence of an oxygen ambient produced no detectable change in the state of the surface.

The oxidation procedure in the present study is distinguished from an earlier one [7] in the establishment of a linear exposure scale. This was accomplished by repeatedly applying a fixed dose (5×10^{-5} Torr for 500 sec.) rather than manipulating the pressure to increase the exposure. In the latter procedure, the pressure variation of the surface reactions reflects both the dependence of the oxidation on exposure as well as the pressure dependent efficiency of the uptake activation process. By repetition of a fixed dose instead, a sample exposed twice to the activated oxygen received double the dose as one exposed once only. The linear

AD-A156 079

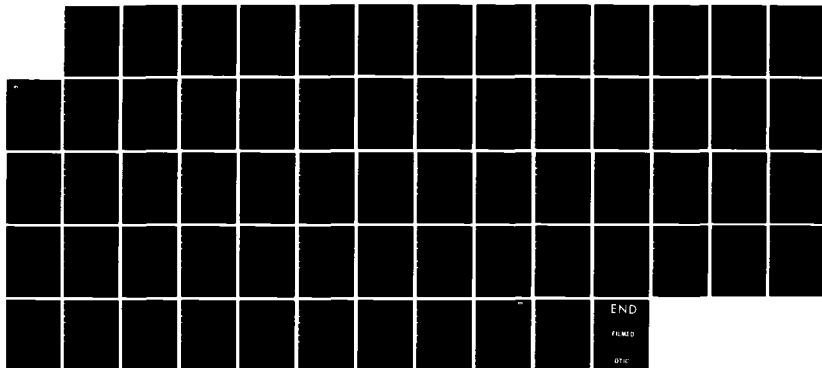
HQCDTE SURFACE AND DEFECT STUDY PROGRAM(U) SANTA
BARBARA RESEARCH CENTER GOLETA CALIF J A WILSON ET AL.
01 JUL 84 RPT50220 MDA903-83-C-0108

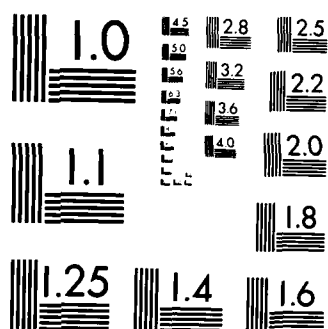
2/2

UNCLASSIFIED

F/G 20/12

NL





MICROCOPY RESOLUTION TEST CHART
NATIONAL BUREAU OF STANDARDS-1963-A

exposure scale established in this way facilitates preliminary analysis of the kinetics involved in the oxygen uptake.

Photoemission spectroscopy served to characterize the clean surface and monitor the effects of oxidation. To excite the photoelectrons, photon energies of 55 and 85 eV from a synchrotron source (Stanford Synchrotron Radiation Laboratory) were used for spectra of the Hg 5d and Cd 4d core levels and valence band and the Te 4d core lines, respectively. This choice provides high surface sensitivity and results in nearly the same kinetic energy and thus inelastic mean free path for the core level signals of all substrate constituents. The monochromator was operated with 0.2 eV resolution and the double pass cylindrical mirror analyzer used to energy analyze and collect the electron distribution gave an energy resolution of 0.18 eV. The spectra presented have been normalized to the incident beam intensity as monitored by the electron yield from an 80 percent transmitting copper-coated stainless steel mesh inserted into the beam.

III. Results and discussion

The chemistry and kinetics of the oxidation reactions are revealed in shifts in energy and changes in intensity of the core line emission as a function of activated oxygen exposure. The Cd 4d and Hg 5d core lines and valence band emission from the clean and oxygen exposed surface of $\text{Hg}_{0.69}\text{Cd}_{0.31}\text{Te}$, shown in Figure 1, illustrate key features of the alloy surface oxygen chemistry. As the number of doses increases, an oxygen 2p derived structure appears and systematically increases in strength near 46 eV, indicating the uptake of oxygen by the surface. As the oxygen coverage increases, the spin orbit split Hg 5d_{5/2} and 5d_{3/2} levels are

attenuated while the Cd 4d emission is substantially unchanged in intensity. The difference in the exposure dependence of the Hg and Cd signals indicate the oxide grows excluding Hg while incorporating Cd. The release of Hg from the growing film is similarly found to occur upon exposure of HgTe to activated oxygen [8]. In the limited number of exposures performed on CdTe, Cd is observed as a constituent of the oxide formed on this compound.

The Te 4d core level spectra as a function of exposure, presented in Figure 2, augment the information gained from the cation core lines in describing the oxidation process. Characteristic of oxidized Te [9], a doublet shifted by 3.6 eV to higher energy appears with the first dose and increases in strength with subsequent exposure (Figure 2). This chemical shift, the difference in energy between the peaks of the oxidized Te 4d_{5/2} signature and the corresponding emission from Te in the semiconductor lattice, is initially the same for HgTe and the alloy. Additional exposure results in a different chemical shift for the two materials and produces an oxidized Te signal broadened by 0.2 eV (full width at half maximum) for both samples (see Figure 2 for the alloy case.) These changes in peak position and width of the oxidized Te reflect a changing mixture of oxides, each component of which has an oxidized Te signal at somewhat different energy.

That the oxidized Te signal contains more than one contribution is more directly illustrated in Figure 3a, which also indicates the temporal stability of these compounds. The two spectra characterize the HgTe surface after the highest exposure used and were recorded immediately following the dose and 12 hours later. With the passage of time, the 4d peaks arising from Te in the oxide sharpen and appear at lower binding energy relative to the core level emission immediately following the

exposure. It thus appears that the oxide formed at the higher exposure levels includes a component (indicated by the higher binding energy contribution) which is unstable at room temperature. Interfacial reactions which convert one type of oxide into another have been predicted from thermodynamic data and observed between bulk compounds under moderate heating [10]; the oxides contributing to measured spectra (see Figure 3) must be identified before the predicted reactions can be verified in this case. The sharpening shown in Figure 3a has been observed in a previous study of the growth of thin native oxide layers on HgCdTe [7] but could not be assigned unambiguously to an oxide instability at that time. A similar narrowing and sharpening of the oxide signal was observed when the HgCdTe sample was re-examined 23 hours after completing the highest dose. This phenomena was not examined on CdTe.

Like the oxidized Te lineshape discussed above, the Te 4d emission near 40.8 eV in Figure 2 from the oxygen exposed surface also arises from more than one contribution. In the spectrum taken following the first exposure, the Te 4d signal at the bulk (clean surface) position is broadened asymmetrically to higher binding energy. This broadening is also apparent following additional exposure, particularly after doses 3 and 4, but tends to decrease overall with continued uptake. As illustrated in Figure 3b, the additional emission at higher binding energy can be accounted for by a replica of the clean surface peaks shifted by 0.6 eV to higher binding energy and added to the emission from the Te in the HgCdTe. The new state of Te has a binding energy characteristic of elemental Te [9] although a partially oxidized Te signal with the same binding energy would not be distinguished from elemental Te in these measurements. The Te signal at the elemental position was found in

varying amounts on all three compounds.

In addition to the chemical information derived from the photo-emission spectra, preliminary kinetic data can also be extracted.

Assuming an abrupt interface between the oxide film and the underlying semiconductor, an equal density of Te atoms in the two regions, and a constant inelastic mean free path in each case, the thickness of the overlayer may be estimated from the exponential attenuation of the substrate signal with oxide thickness and the increasing strength of the emission from oxidized Te (Figure 2). Working in this simplified model, the thickness, in units of the inelastic mean free path, λ , is given by

$$\frac{T}{\lambda} = \ln \left(\frac{[Te^{Ox}]}{[Te]} + 1 \right) ,$$

where $[Te^{Ox}]$ and $[Te]$ are the integrated intensities of the core level emission from the oxidized and unoxidized Te (including the signal at the elemental position). The results of such an analysis for the three samples studied is presented as a function of the number of standard doses applied in Figure 4. Based on this measure of thickness, the oxidation is found to proceed in proportion to the exposure in each case with no evidence in the data for saturation in the uptake for films grown in excess of at least two monolayers thick. The rate of oxidation, given by the slope of the lines, is found to be 69 percent as great for the $Hg_{0.69}Cd_{0.31}Te$ alloy as for the HgTe sample; i.e., the rate of oxidation scales as the number of Hg-Te bonds. This finding in conjunction with the result from the core level spectra that Hg is released and not incorporated in the initial stages of oxide growth suggests the importance of breaking the Hg-Te bond as a step in the oxidation process. If HgCdTe were to oxidize as merely a mixture of the binary compounds, the rate for the alloy would be an appropriate average of the rates for HgTe and

CdTe and the line for the alloy in Figure 4 would fall intermediate to those of the binaries. Instead, the rate of oxidation as determined from the change in thickness with exposure is greater for CdTe than the $x = 0.31$ alloy, implying a modification of the activity of the Cd-Te site in $\text{Hg}_{0.69}\text{Cd}_{0.31}\text{Te}$ compared to the binary.

IV. Conclusion

The spectra obtained during study of the activated oxidation of CdTe, HgTe, and $\text{Hg}_{0.69}\text{Cd}_{0.31}\text{Te}$ indicate the oxide which initially forms on the samples containing Hg does so with the release of this constituent; whereas, Cd is retained in the oxide of CdTe and the alloy. The observation of the release of Hg together with the rate limiting role of the Hg-Te bond are consistent with the lesser strength of this bond compared to that of Cd to Te. Similarly, the modification in the activity of the Cd-Te site in the alloy exemplified by the higher rate of oxidation for CdTe than the $x = 0.31$ sample is in line with the difference in electronic structure of the two materials which results in a stronger Cd-Te bond in the alloy than CdTe. It would be of interest to extend the measurements to higher x value, where the kinetics operative during the oxidation of CdTe may become dominant. Further study of the kinetics of oxidation is also warranted in as much as the oxide produced by the activated oxidation procedure on HgTe and HgCdTe exhibited unstable behavior indicative of nonequilibrium constitution or interfacial reactions.

Acknowledgment

We gratefully acknowledge Roger A. Cole, Santa Barbara Research Center, for growth of the material used. This work was supported by

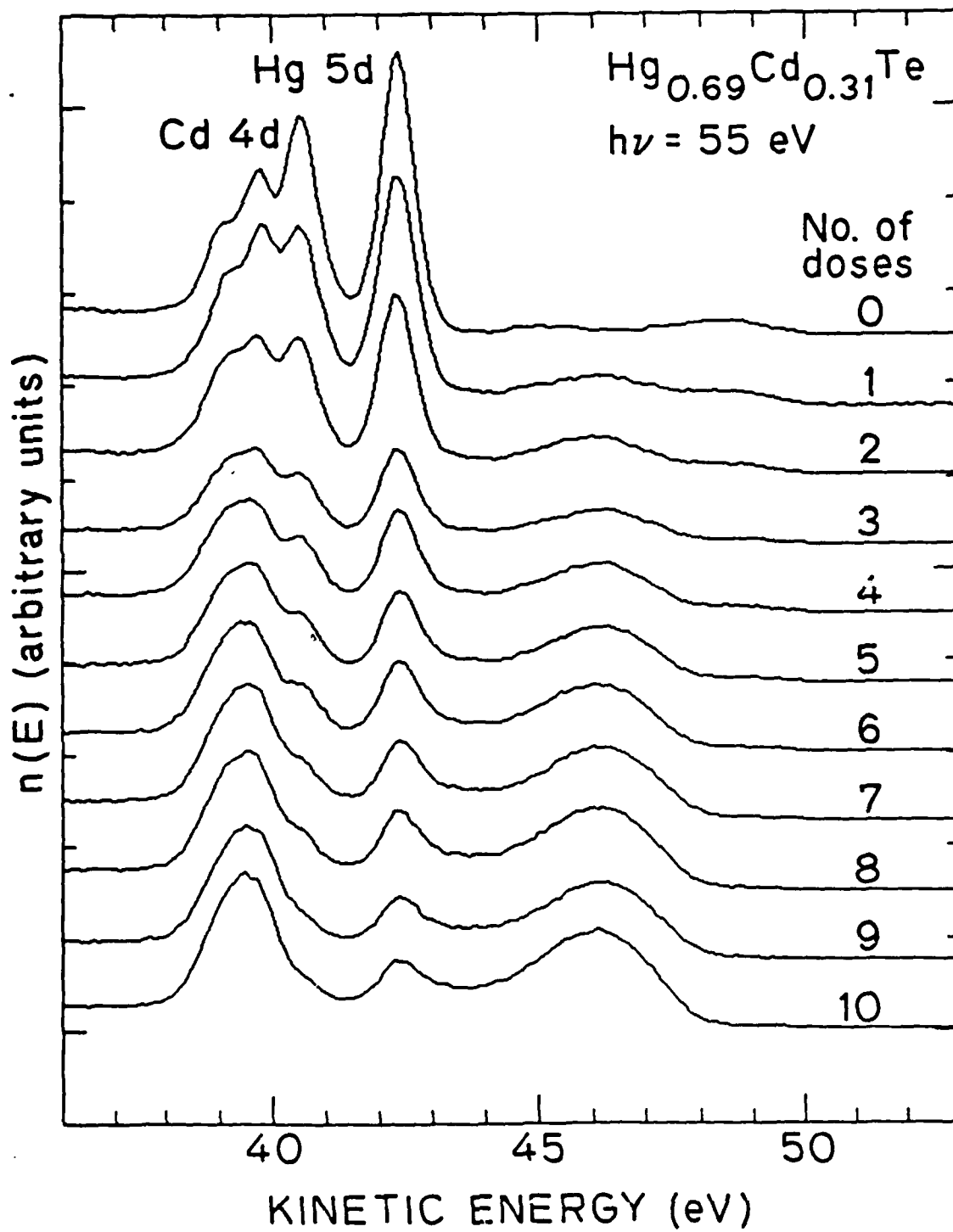
DARPA contract 916610-B5 and performed at the Stanford Synchrotron Radiation Laboratory which is supported by the Department of Energy, Office of Basic Energy Sciences; and the National Science Foundation, Division of Materials Research.

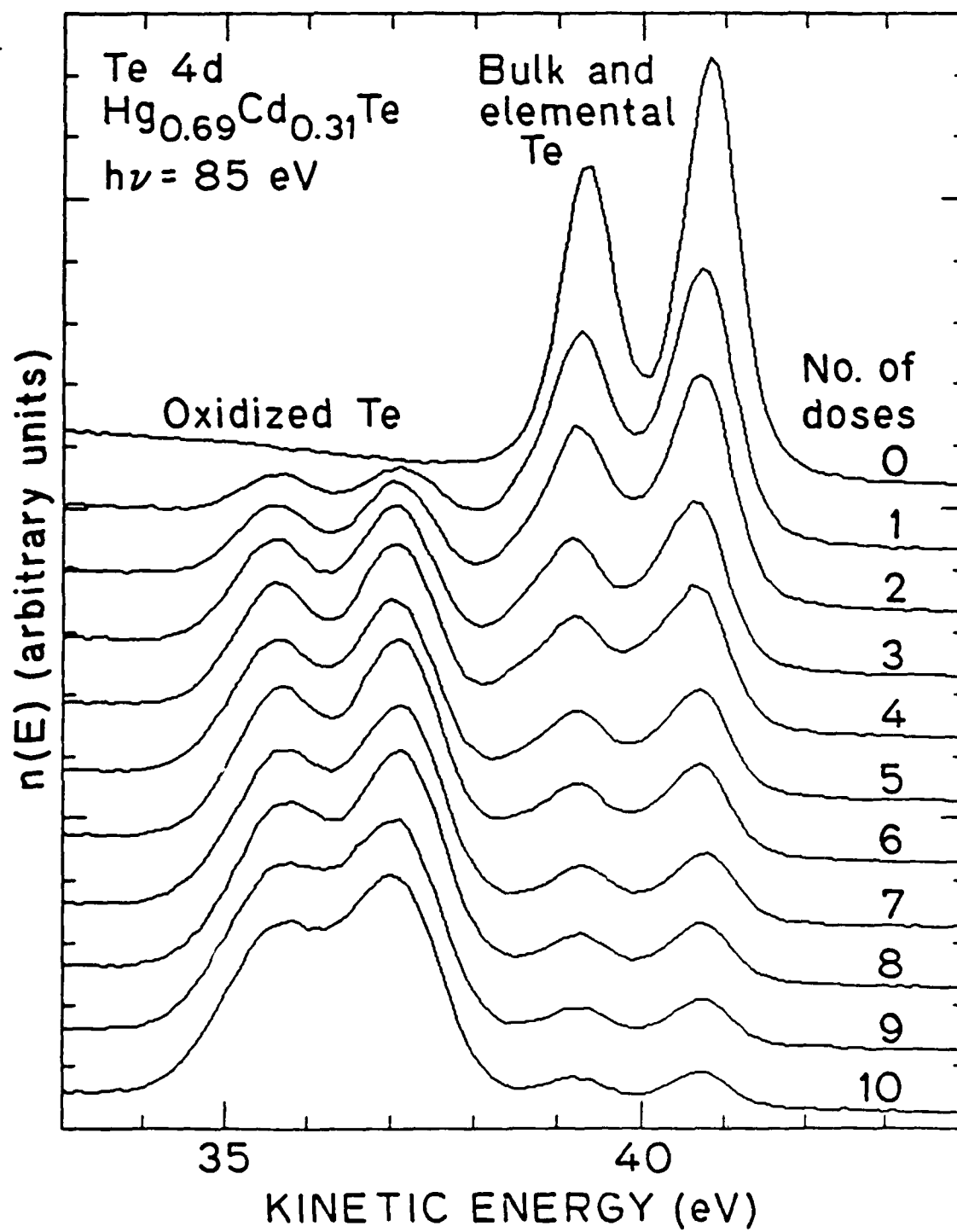
References

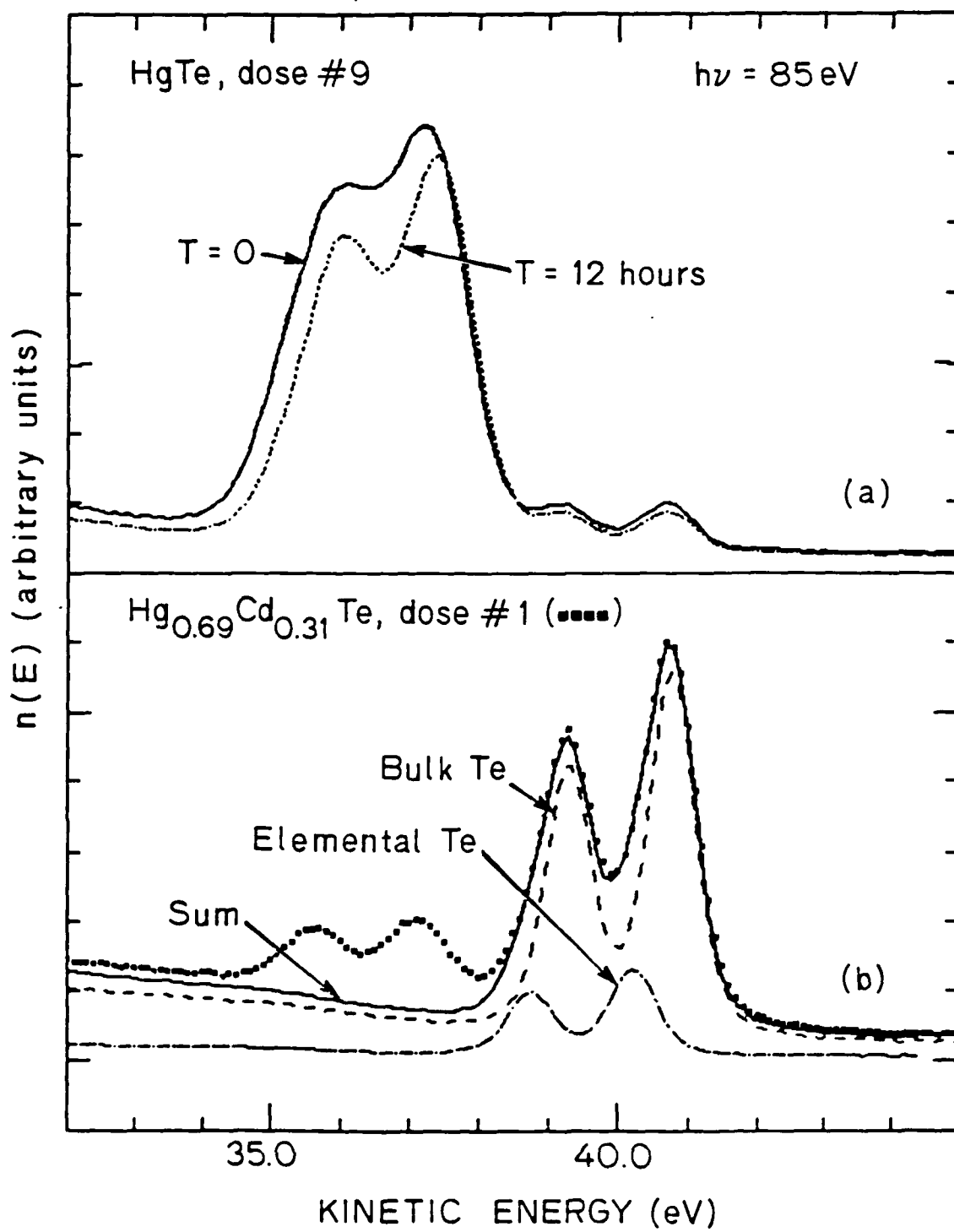
1. J. A. Silberman, P. Morgen, I. Lindau, W. E. Spicer, and J. A. Wilson, J. Vac. Sci. Technol. 21 (1982) 142.
2. An-Ban Chen and A. Sher, J. Vac. Sci. Technol. 21 (1983) 138; K. C. Hass, H. Ehrenreich, and B. Velicky, Phys. Rev. B 27 (1983) 1088.
3. W. A. Harrison, J. Vac. Sci. Technol. A 1 (1983) 1672.
4. W. E. Spicer, J. A. Silberman, I. Lindau, A.-B. Chen, A. Sher, and J. A. Wilson, J. Vac. Sci. Technol. A 1 (1983) 1735.
5. A. Willig, B. Sapoval, K. Leiber, and C. Verie, J. Phys. C 9 (1976) 1981.
6. A. Sher, A.-B. Chen, W. E. Spicer, and C. K. Shih, this proceedings.
7. J. A. Silberman, D. Laser, I. Lindau, W. E. Spicer, and J. A. Wilson, J. Vac. Sci. Technol. A 1 (1983) 1706.
8. Data will appear in a future publication.
9. David R. Rhiger and Robert E. Kvass, J. Vac. Sci. Technol. 21 (1982) 448.
10. David R. Rhiger and Robert E. Kvass, J. Vac. Sci. Technol. A 1 (1983) 1712.

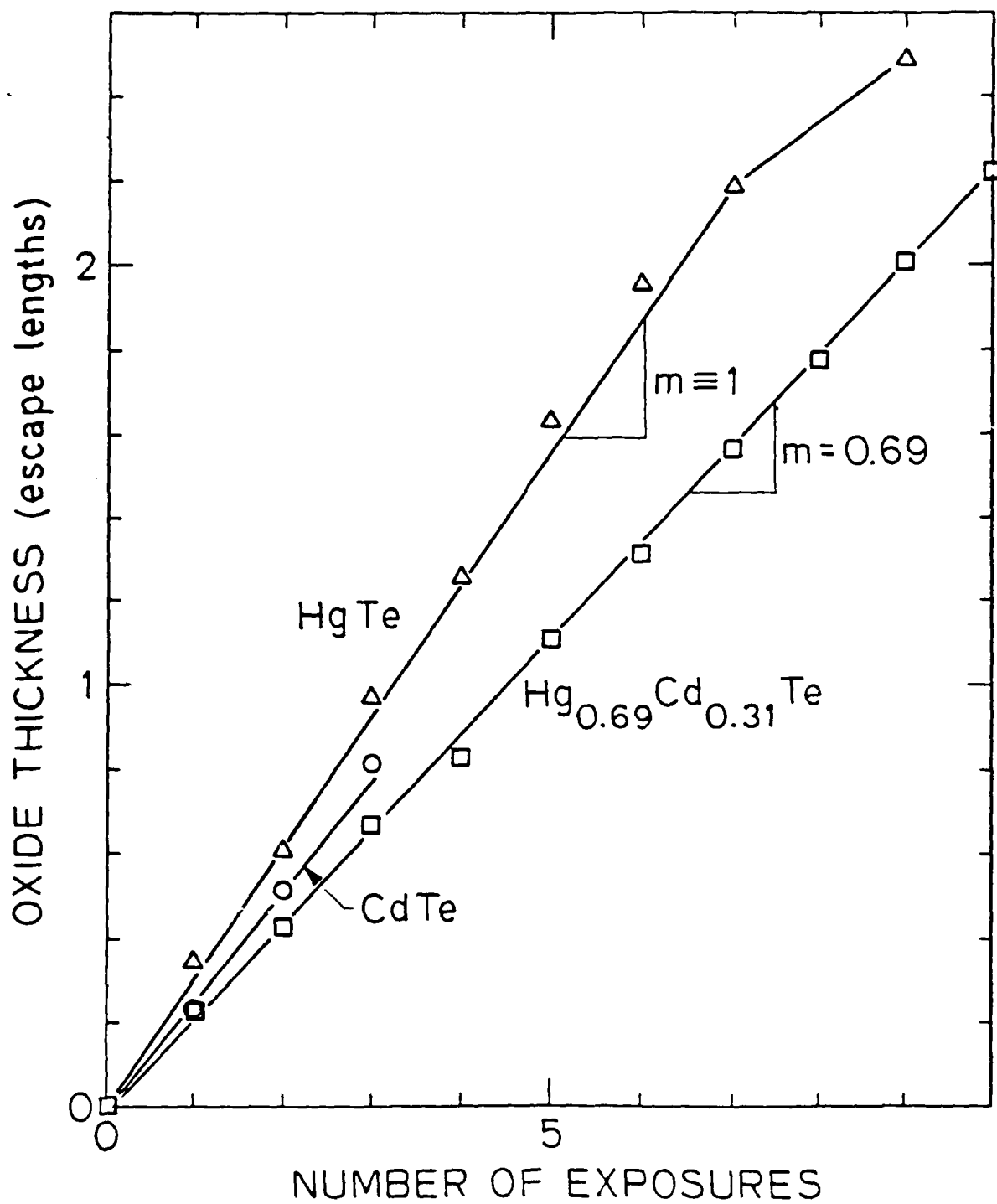
Figure Captions

- Figure 1 Photoemission spectra of the Cd 4d, Hg 5d and valence band emission of $\text{Hg}_{0.69}\text{Cd}_{0.31}\text{Te}$ cleaved in vacuum and exposed repeatedly to fixed doses of oxygen activated by a hot filament in line-of-sight of the sample surface.
- Figure 2 Photoemission spectra of the Te 4d lines on the clean and oxygen dosed surface. The details of the changes noted in the oxidized Te and unoxidized signal are discussed in the text.
- Figure 3a Illustration of time evolution at room temperature of the oxidized Te 4d signal following the highest exposure on HgTe. After 12 hours, the peaks sharpen, losing the high binding energy component. A similar result occurred for the $\text{Hg}_{0.69}\text{Cd}_{0.31}\text{Te}$.
- Figure 3b Decomposition of the Te 4d emission from $\text{Hg}_{0.69}\text{Cd}_{0.31}\text{Te}$ recorded following the first exposure into peaks at the energy of Te in HgCdTe and a contribution at the energy of elemental Te.
- Figure 4 Thickness of the oxide derived from the relative intensity of the oxidized and unoxidized Te emission as a function of the number of standard doses applied to the surfaces of CdTe, HgTe, and $\text{Hg}_{0.69}\text{Cd}_{0.31}\text{Te}$. One escape length, the unit of thickness, is equivalent to one to three monolayers.









$$\bar{d} = (1 - x)d_o(AC) + xd_o(BC) \quad (9)$$

where $d_o(AC)$ and $d_o(BC)$ are the pure crystal lattice constants. Then in an A(3)B(1) configuration [see Fig. 1(a)], the anion will be displaced along the BC bond. For definiteness, suppose $d(AC) > d(BC)$; then the anion will be shifted away from the tetrahedral site toward the B atom. Because $d_o(AC) \geq \bar{d} \geq d_o(BC)$, the $d(BC)$ bond will be elongated and the $d(AC)$ bonds will also be locally elongated in a strained configuration. We can for this case [see Fig. 1(a)] write

$$d(BC) = (1 - \delta)\bar{d} \quad (10)$$

and for the three AC bonds

$$d(AC) = \sqrt{1 + \frac{2\delta}{3} + \delta^2} \bar{d} \quad (11)$$

In an A(2)B(2) configuration [see Fig. 1(b)], we have for both BC bonds

$$d(BC) = \sqrt{1 - \frac{2}{3}\delta + \frac{1}{3}\delta^2} \bar{d} \quad (12)$$

and for both AC bonds

$$d(AC) = \sqrt{1 + \frac{2}{3}\delta + \frac{1}{3}\delta^2} \bar{d} \quad (13)$$

The values of δ are determined by the condition $dE_L/d\delta = 0$, or

$$\begin{aligned}
\Delta E_b^1 = & \frac{2[U_b^0 - U_a^1(BC)V_{1-}]^2}{\epsilon_b^0 - \epsilon_a^1(BC)} - \frac{2[U_b^0 - U_a^1(AC)V_{1-}]^2}{\epsilon_b^0 - \epsilon_a^1(AC)} \\
& + \frac{d\theta}{4\theta d} 2 \left\{ \frac{[U_b^0 - U_a^1(BC)V_{1-}]^2}{\epsilon_b^0 - \epsilon_b^1(BC)} - \frac{[U_b^0 - U_a^1(AC)V_{1-}]^2}{\epsilon_b^0 - \epsilon_a^1(AC)} \right. \\
& \left. + \frac{[U_b^1(BC)U_a^0 - V_{1-}]^2}{\epsilon_b^1(BC) - \epsilon_a^0} - \frac{[U_b^1(AC)U_a^0 - V_{1-}]^2}{\epsilon_b^1(AC) - \epsilon_a^0} \right\} \quad (7)
\end{aligned}$$

where the partial derivative is taken with respect to the central bond length (a term designated with a superscript o) and in this simple approximation

$$\Delta E_b^\eta = \eta E_b^1, \quad \eta = 0, 1, 2, 3 \quad (8)$$

The bond length shifts are found from Eq. (2). The modification of these expressions for an anion-substituted alloy follows from symmetry.

Method 2—A more realistic calculation includes strain and permits the lattice to fit together. The simplest non-self-consistent, near-neighbor version of this calculation proceeds as follows. In a cation-substituted alloy $A_{1-x}B_xC$ (e.g. $Hg_{1-x}Cd_xTe$ or $Zn_{1-x}Hg_xTe$), the cations are assumed to occupy their regular fcc sublattice sites, while the anions accommodate to their local configuration. The average lattice constant is taken to follow Vegard's rule:

fits together by having the metal sublattice nearly retain its f.c.c. structure with a lattice constant following Vegard's rule, and each As atom adjust its local position and accommodates to which metal atoms occupy its four neighboring sites. Thus there are five local arrangements; in the first an As atom is surrounded by four Ga atoms [a Ga(4)In(0) configuration], in the second there are three Ga atoms and one In [a Ga(3)In(1) configuration], and the last three configurations are Ga(2)In(2), Ga(1)In(3), and Ga(0)In(4). In a general cation $A_{1-x}B_xC$ alloy or anion $CA_{1-x}B_x$ alloy, the generalizations are obvious, and one can examine $A(4-\eta)B(\eta)$; $\eta = 1, 2, 3, 4$ configurations.

Method 1—The lowest level of approximation that takes account of these findings calculates [from Eqs. (1) and (2)] a given bond's energy and length shift when its surrounding bonds have different constituents. The calculation is done assuming that the surrounding bonds retain their pure crystal bond lengths. This model is somewhat unrealistic, in that it ignores the strains that must be present to allow the lattice to fit together. However, it is nonetheless useful because it treats the largest terms, viz. those arising from charge transfer between the substituted species in the alloy, and results in analytic expressions, while the successively more complicated treatments must be done numerically. It is also useful later because, taken together with the more complete calculations, it allows one to judge the relative contribution from different physical effects. From Eq. (1) in a cation-substituted alloy one can deduce an expression for the energy shift of an AC bond when η surrounding bonds are replaced by BC, ΔE as

Finally combining Eqs. (1) through (5), the bond energy is

$$E_b = -(1 + \alpha_p^2)(V_2^2 + V_3^2)^{1/2} - \frac{9}{8}(1 - \alpha_p^2)^2 \frac{(V_{1+}^2 + V_{1-}^2)}{(V_2^2 + V_3^2)^{1/2}} + |V_{1+} + V_{1-}| + \frac{\epsilon_{p+} - \epsilon_{p-}}{2} \quad (6)$$

Equation (6) was first derived by Harrison using a much simpler argument.¹ The bond energies quoted in Table I and on Fig. 5 are calculated from this expression, using as input the correlated term values from Table I and the experimental bond lengths.

B. Alloy Calculations

There are several layers of sophistication that can be used to compute the bond energy and length changes between pure compounds and their alloys. However, all the calculations are motivated by the EXAFS experimental result found first for $\text{Ga}_{1-x}\text{In}_x\text{As}$ and later in other compounds.⁵ It was found that, while the average bond length in the alloy follows Vegard's rule and varies linearly between those of the pure constituents, the individual bond lengths of GaAs and InAs are nearly the same as those of the pure materials--changing by only about 4 percent. The shorter GaAs bond increases its length when it is an impurity in an InAs host by about 4 percent, and the longer InAs bond shrinks by about 4 percent in the opposite extreme where it is the impurity in GaAs. The lattice

$$\equiv \sum_{i=0}^3 (T_{m+,n}^i + T_{m-,n}^i) \quad (4)$$

The last identity in Eq. (4) defines the indicated bond tensions. Collecting all the results from the earlier paragraphs, one finds (dropping the bond designation n):

$$T_{m+}^0 = -\frac{4}{d}[(1 + \alpha_p)\alpha_p + \frac{\alpha_c^2 \sqrt{V_2^2 + V_3^2}}{\epsilon_b^0 - \epsilon_a^1}] \epsilon_{m+}^0 \quad (5a)$$

$$T_{m+}^1 = T_{m+}^2 = T_{m+}^3 = \frac{4}{d}[(1 - \alpha_p)\alpha_p - \frac{\alpha_c^2 \sqrt{V_2^2 + V_3^2}}{\epsilon_b^1 - \epsilon_b^0}] \epsilon_{m+}^1 \quad (5b)$$

$$T_{m-}^0 = \frac{4}{d}[(1 - \alpha_p)\alpha_p - \frac{\alpha_c^2 \sqrt{V_2^2 + V_3^2}}{\epsilon_b^0 - \epsilon_a^1}] \epsilon_{m-}^0 \quad (5c)$$

$$T_{m-}^1 = T_{m-}^2 = T_{m-}^3 = -\frac{4}{d}[(1 + \alpha_p)\alpha_p + \frac{\alpha_c^2 \sqrt{V_2^2 + V_3^2}}{\epsilon_b^1 - \epsilon_a^0}] \epsilon_{m-}^1 \quad (5d)$$

Harrison has written Eq. (1) without explicit reference to the surrounding bonds. Equation (1) in its present form is rather easily used for alloy calculations by replacing host atom terms by one appropriate to the alloy.

The parameter γ for each compound is fixed by the condition that there is no net force on atoms at their equilibrium lattice positions. This condition is satisfied if the gradient of the total energy with respect to all the bond lengths vanishes:

$$V_{(d_n)} E_T = 0, \text{ where } E_T = \sum_n E_b^n.$$

This condition is equivalent to the requirement that the net bond tension $T_{on} + T_{mn}$ for the n th bond equals the repulsive force

$$T_{on} + T_{mn} - \frac{4\gamma_n}{d_n^5} = 0 \quad (2)$$

where

$$T_{on} \equiv \frac{\partial}{\partial d_n} [-2\sqrt{V_2^2 + V_3^2}] = 4\alpha_c \sqrt{V_2^2 + V_3^2} / d \quad (3)$$

$$T_{mn} \equiv 2 \frac{\partial}{\partial d_n} \sum_{i=0}^3 (\epsilon_{m+i,n}^i + \epsilon_{m-i,n}^i)$$

$$U_{b+} = \sqrt{(1 - \alpha_p)/2} = U_{a-}$$

$$U_{b-} = \sqrt{(1 + \alpha_p)/2} = U_{a+}$$

are the probability amplitudes of finding the cation and anion sp^3 -hybrid contributions to the bonding and antibonding states, e.g. U_{b+} is the probability amplitude of finding the cation³ hybrid in the bonding state, etc.,

$$\alpha_p \equiv V_3 / \sqrt{V_2^2 + V_3^2} \text{ is the polarity,}$$

$$\alpha_c \equiv |V_2| / \sqrt{V_2^2 + V_3^2} \text{ is the covalency,}$$

$$\epsilon_{\{b\}} = \frac{\epsilon_+ + \epsilon_-}{2} \{ \mp \} \sqrt{V_2^2 + V_3^2}$$

are the bonding and antibonding one electron energy states owing only to covalent and ionic interactions,

$$\epsilon_{\{b\}} \equiv \frac{(U_{b\{z\}}^i U_{a\{z\}}^o V_{1\{z\}})^2}{\epsilon_b^i - \epsilon_a^o}, \quad i = 1, 2, 3$$

are the contributions to the bond in question arising from its antibonding state interactions with a neighboring bonding state i , and γ is an adjustable coefficient chosen so the measured bond lengths are reproduced

transfer from the cation to the anion), the second term is the promotion energy per bond to form sp^3 hybrids on both atoms, the third term is the bond formation energy owing to the covalent and ionic terms, the fourth term is Harrison's metallization energy, and the fifth term is the repulsive overlap energy that prevents the bonds from collapsing. The various symbols are defined below:

$\epsilon_{p\{\pm\}}$ is the $\left\{ \begin{smallmatrix} \text{cation} \\ \text{anion} \end{smallmatrix} \right\}$ p-state correlated term values⁴

$V_{1\{\pm\}} \equiv (\epsilon_{p\{\pm\}} - \epsilon_{s\{\pm\}}) / 4$ are hopping integrals between two adjacent bonds coupled through a $\left\{ \begin{smallmatrix} \text{cation} \\ \text{anion} \end{smallmatrix} \right\}$

$\epsilon_{s\{\pm\}}$ are the $\left\{ \begin{smallmatrix} \text{cation} \\ \text{anion} \end{smallmatrix} \right\}$ s-state correlated term values

$V_2 \equiv -24.5/d^2$ [eV] is the covalent energy

d is the bond length

$V_3 \equiv (\epsilon_+ - \epsilon_-) / 2$ is the polar energy

$\epsilon_{\{\pm\}} \equiv (\epsilon_{s\{\pm\}} + 3\epsilon_{p\{\pm\}}) / 4$ are the sp^3 hybrid energies

$$\epsilon_{m\{\pm\}}^o \equiv \sum_{j=1}^3 (U_{b\{\pm\}}^o U_{d\{\pm\}} V_{1\{\pm\}})^2 / (\epsilon_b^o - \epsilon_d)$$

is the contribution to the reduction of the bonding state energy ϵ_s^o calculated by second-order perturbation theory of the bond in question (denoted by superscript o), owing to its interaction with the three neighboring ($i = 1, 2, 3$) antibonding states sharing the same $\left\{ \begin{smallmatrix} \text{cation} \\ \text{anion} \end{smallmatrix} \right\}$, where

expected, because the electron effective mass in a narrow-gap material is small; hence, the electron wave functions at Γ_{1c} are distributed over many atoms, with the result that alloy scattering rates are small at the band edge. The hole mobilities are large for a somewhat different reason: The valence band edge is mostly composed of Te p- states; however, there is also some cation p- state contribution. Because the p- state energies of Hg and Zn are nearly the same, the alloy scattering strength at the valence band edge is small. We conclude that, because of its structural advantage, HgZnTe may be superior to HgCdTe for infrared devices.

II ALLOY MODIFICATION OF THE BOND ENERGY AND LENGTH

A. *Pure Compounds*

The first task is to recast Harrison's bond energy and bond length formalism into a structure suitable for generalization to alloys. Focus attention on the n th bond of a pure zinc blende structured compound semiconductor; for the time being, suppress any notation identifying it. Then, in a II-VI compound, the bond energy is is:¹

$$E_b = \frac{\epsilon_{p+} - \epsilon_{p-}}{2} + V_{1+} + V_{1-} - 2(V_2^2 + V_3^2)^{1/2} + 2 \sum_{i=0}^3 (\epsilon_{m-}^i + \epsilon_{m+}^i) + \frac{\gamma}{d^4}$$

where the first term is the energy per bond needed to transfer two electrons from a p- state on the Group VI atom (the anion) to a p- state on ~~the~~ the Group II atom (the cation), so that both start with four electrons (ultimately in the final bonding arrangement there is a net electron

I INTRODUCTION

The objective of this work is to understand the microscopic mechanisms that govern the stability of $\text{Hg}_{1-x}\text{Cd}_x\text{Te}$ alloys, and then to suggest changes in the material that improve its strength without adversely affecting its electronic behavior. In pursuit of this goal we have extended Harrison's bonding theory,¹ which is applicable to all tetrahedral structured semiconductors, to calculate bond length and energy changes in an alloy—including charge shift and reconstruction effects—relative to their pure crystal values, vacancy formation energies, dislocation energies, and hardness.

In this paper, we review the experimental situation in several of these areas and compare some of the results with theory for all the Group IV, III-V compound, and II-VI compound semiconductors and their alloys. For example, the theory properly predicts the observed inverse ninth power bond length (d^{-9}) dependence of the hardness² of semiconductors and, with no adjustable parameters, their correct magnitude. We demonstrate that the weak HgTe bond is destabilized by alloying it with CdTe, HgS, or HgSe; however, the bond is stabilized by ZnTe. Moreover, because the bond length of ZnTe (2.406 Å) is 14 percent shorter than that of HgTe (2.797 Å) or CdTe (2.804 Å), the dislocation energy per unit length and hardness of the alloys $\text{Hg}_{1-x}\text{Zn}_x\text{Te}$ and $\text{Cd}_{1-x}\text{Zn}_x\text{Te}$ are predicted in agreement with some experiments to be significantly higher than those of the compounds with $x = 0$. Measurements indicate that the electron and hole mobilities of $\text{Hg}_{1-x}\text{Zn}_x\text{Te}$ with $x \sim 0.16$, corresponding to a 0.1-eV band gap, are comparable to those of $\text{Hg}_{1-x}\text{Cd}_x\text{Te}$ for $x = 0.2$.³ This is to be

improve the structural properties of HgTe and CdTe. Experiments that support these predictions are noted. The electronic transport properties of 0.1-eV band gap HgZnTe are about the same as those of HgCdTe, and the structural properties of the Zn compound are superior; thus, we conclude that HgZnTe is likely to be the better material for IR devices.

Section IV-I

EFFECTS INFLUENCING THE STRUCTURAL INTEGRITY
OF SEMICONDUCTORS AND THEIR ALLOYS*

Arden Sher

SRI International, Menlo Park, California 94025

An-Ban Chen

Auburn University, Auburn, Alabama 36489

W.E. Spicer†

C-K Shih

Stanford University, Stanford, California 94305

ABSTRACT

The bond length and energy changes of the constituents of alloys relative to their pure crystal values are calculated from an extension of Harrison's method. It is demonstrated that the already weak HgTe bonds are destabilized by adjacent CdTe, HgS, or HgSe, but are stabilized by ZnTe. It is also argued that dislocation energies and the hardness of semiconductors vary as a high inverse power of the bond length of the constituents. Hence, the shorter ZnTe bond as an additive should

This work was supported in part by AFOSR Contract F49620-81-K-0012 and by DARPA Contract MDA-903-83-C-0108.

†Stanford Ascherman, Professor of Engineering.

(This Page Intentionally Left Blank)



Section IV

July 1984

SRI/SBRC Cooperative HgCdTe Surface Studies Program
2nd Year - Mid-Term Progress Report

SRI Project 5302

Santa Barbara Research Center
74 Coromar Drive
Goleta, CA 93117
Attn: Dr. J. A. Wilson

The main results we have completed in this period are contained in two papers

- "Effects Influencing the Structural Integrity of Semiconductors and Their Alloys," A. Sher, An-Ban Chen, W. E. Spicer, and C. K. Shik (submitted for publication in the Proceedings of Mercury Cadmium Telluride"
- "Dislocation Energies and Hardness of Semiconductors," A. Sher, An-Ban Chen, and W. E. Spicer (submitted to Applied Physics Letters).

These papers are attached as appendices A and B.

SRI International

333 Ravenswood Ave. • Menlo Park CA 94025 • 415 326-6200 • TWX 910-373-2046 • Telex 334 486 • Facsimile 415 326-5512

$$\sum_{n=0}^3 (T_{an} + T_{mn} - \frac{4\gamma_n}{d_n^5}) \frac{\partial d_n}{\partial \delta} = 0 \quad (14)$$

Equation (14) is solved by:

- (1) Assigning the γ_n s their pure crystal values
- (2) Supposing that the four tetrahedrally configured anions are embedded in the virtual crystal [see Fig. 1(c)]
- (3) For each x , δ is varied and the bond tensions are calculated and inserted into Eq. (14) until a value of δ is found that satisfies this equation.

The computer outputs are δ and the AC and BC bond energies. This method can be extended to take explicit account of the bond length variations of larger clusters, and \bar{d} can be calculated explicitly (instead of using Vegard's rule) so the results can be made to be self-consistent. Also, effects arising from bond angle distortions can be included. The major effects that are currently included in the calculation arise from the bond length dependence of V_2 , and charge shifts driven by hybrid energy differences and coupled through the metallization terms. However, V_2 is also sensitive to bond angle distortions, and these effects are not included in the present results. We expect their inclusion will modify the quantitative results by 10 to 30 percent, but not the trends.

C. Results

The correlated atomic term values⁴ for the elements in the more common II-VI compounds are listed in Table I, along with the bond energies of their nine compounds. The valence s -state energies for Zn are large, become smaller as for Cd, and then (in an unusual occurrence) the

trend reverses and the Hg s- levels are deeper again. This is caused by the relativistic terms that become important in Hg. The p- state levels have a similar trend; however, the differences among the atoms are much smaller. The levels of the anions are deeper than those of the cations. Thus, there is a net electron transfer from the cations to the anions, which is responsible for the ionic contribution to the bonding. The polarity, also listed in Table I, reflects the relative contribution of ionic and covalent character to the bonds. Notice that α_p is small for ZnTe larger for CdTe, and smaller again for HgTe. By contrast, the metallic contribution E_m is large for ZnTe and HgTe and small for CdTe. In fact, HgTe would not be bound if it were not for the metallic contribution to the bond, not a terribly surprising result, because HgTe is a semimetal. The bond lengths of CdTe and HgTe are very nearly the same, but this is an accident resulting from the balance of contributions to their bonds: CdTe is dominated by the covalent and ionic contributions to its bond, while HgTe has bonds that are mostly covalent and metallic. We should therefore not be too surprised if their alloy displays some unusual bond length variations.

Figures 2 and 3 illustrate the $\text{Hg}_{1-x}\text{Cd}_x\text{Te}$ alloy concentration variations of the length and energy for the five configurations. These results were calculated using the second method discussed in Section II-B. In Fig. 2 we see the unexpected result that the shorter HgTe bond becomes still shorter in the alloy, while the CdTe bond length increases. Moreover, the changes are large compared to the original length difference. Thus one can expect to find local microstrains, even in this nearly lattice-matched material. The bond energy variations shown in Fig. 3 are

display an important result. The already weak HgTe bond is destabilized by the presence of Cd. The flat concentration variation of the bond lengths and energies is peculiar to HgCdTe; much more structured behaviors are exhibited by other compounds.

Several considerations to keep in mind when dealing with alloys are depicted schematically in Fig. 4 for a Hg(3)Cd(1) configuration. Due to the charge shift alone, the HgTe bond shrinks by 0.030 Å, the minimum in the configuration diagram moves to a smaller bond length and the depth of the well is decreased. Then the bond is stretched by 0.011 Å to its final length. Thus, the bond is not centered at a local minimum. For example, this implies that the force constant of local phonon modes will be related to the second derivative of this configuration diagram evaluated at the strained position away from the well minimum. This effect is even more pronounced for materials with a larger lattice mismatch. Notice that the CdTe bond is also stretched relative to its local minimum in this configuration.

The result for bond energy variations for all the II-VI compound alloys is gathered in Fig. 5. Here the energy shifts of an AC bond in a A(1)B(3) configuration $\Delta E_B^3 = 3\Delta E_B^1$ are presented as a percentage of the pure material bond energy for cation substitute alloys along with equivalent results for anion substantial alloys, e.g. $\text{HgS}_{1-x}\text{Te}_x$. The energy shifts are calculated following the first method presented in Section II-B. We have not had the opportunity to run all the compounds following the more sophisticated calculational procedure. The bond at the top of a column is the one whose energy shift is calculated, and the other

constituent is identified in the line that indicates the energy shift. A negative $3\Delta E_b/E_b$ is destabilizing and a positive one stabilizing. Focus on HgTe. It is destabilized by CdTe, HgS, and HgSe, but is stabilized by ZnTe. The CdTe destabilizes the HgTe bond by 18 percent according to the simple calculation and by 15 percent according to the better one. The difference between Zn and Cd occurs because in the Cd case there is a net electron transfer from the Cd to the Hg, while in the case of Zn there is practically no such transfer. These extra transferred electrons must occupy antibonding states, because the bonding states on the HgTe are full, so the net effect (including other energy state shifts) is to destabilize the HgTe bond. This predicted destabilization of the HgTe bond in HgCdTe alloys agrees with the d-state energy shift reported by Spicer et al. at last year's workshop,⁶ and by the oxygen uptake experiments presented by the same group at this conference.⁷

III DISLOCATION ENERGIES AND HARDNESS

The dislocation energies and hardness of semiconductor are calculated by an extension of Harrison's method.¹ It is demonstrated, in agreement with experiment, that dislocation energies per unit length, depending on the covalency, are proportional to d^{-9} , where d is the bond length and hardness is proportional to d^{-5} to d^{-11} . The low powers are for pure covalent materials. The hardness is related to the interaction energies among dislocations. The detailed theory will be published elsewhere.⁸

Figure 4 shows the theoretical hardness of several semiconductors plotted against experimental values.² The theory is calculated for two different dislocation configurations caused by the extra material pushed by the indenter into the crystal. The lower end of each vertical line is a realistic hardness for the minimum energy configuration, and the upper ends of the lines are the values found for a higher-energy configuration. In most cases, one would expect real configurations to have hardnesses lying somewhere between these two values, once the effect of heat generated by the indentation process is subtracted from the experimental numbers. This theory has no adjustable parameters, yet it predicts the right trends and magnitudes.

IV NATIVE IMPERFECTIONS GROWN INTO ALLOYS

There are two kinds of imperfections we shall discuss: vacancies and dislocations. At present, the conclusions are tentative, because the detailed theory is still incomplete. Vacancy formation energies and the melting temperature are both proportional to the bond energies of the constituents. Thus, one would expect the vacancy density just below the melting point to be about the same for all materials with a similar coordination number; in our semiconductor case, the coordination number is four. Dislocation energies are mostly owing to long-range bond angle distortions⁹ and accordingly are sensitive to the shear coefficients, which vary roughly as d^{-7} for many compounds.¹ Based on this general argument, one would expect to find fewer dislocations in materials with short bond lengths.

Dislocations appear in bulk grown materials through a sequence of steps.¹⁰ We shall only discuss the simplest case, where there are no mechanical stresses on the growing material. In the temperature gradient behind the growth front, there is usually a supersaturated vacancy content. These excess vacancies may diffuse to surfaces where they do no harm, or they may condense into vacancy clusters that can then organize into dislocation loops. If a loop is not parallel to the growth front, it can climb toward the front by absorbing more vacancies. If it climbs faster than the growth progresses, then the loop will reach the front. It can then spread and grow along with the crystal. Observed from the growth surface, such a loop will appear to be two edge dislocations. If this dislocation formation process can be inhibited in any of its steps, the resulting material will have fewer dislocations.

Zn in $\text{Zn}_{1-x}\text{Cd}_x\text{Te}$ or $\text{Zn}_{1-x}\text{Hg}_x\text{Te}$ will serve this function in two ways. The first is that Zn stabilizes the weaker bond in these alloys; accordingly, vacancy formation energies in the alloy should be larger than those in the pure constituent CdTe or HgTe. The melting temperature will also be raised somewhat, which effect "wins" is a matter still to be decided. The second effect is clear cut: The shorter bond lengths of the ZnTe will introduce stiff struts into the system that will increase the dislocation energies and thus should inhibit dislocation loop formation and subsequent climb. The large dislocation density reduction found by Bell and Sen in $\text{Zn}_{1-x}\text{Cd}_x\text{Te}$ with only 4 percent Zn supports this speculation.¹¹

V CONCLUSIONS

We have argued that, in an alloy, the bond energies and bond lengths are modified from their pure crystal values. Bond energies can be strengthened or weakened in an alloy depending on the relative sp^3 -state energies and the consequent net electron shift between the constituents. For most compounds, the average bond length modifications for each type of bond are generally small compared to those suggested by Vegard's rule, in agreement with experiment. However, HgCdTe is an exceptional case, because the bond lengths for HgTe and CdTe are nearly the same (by accident). The bond length and energy shifts also depend sensitively on the local configuration and the bonds are locally strained. These effects must be taken into consideration in a proper theory of alloy vacancy formation energies, phonon frequencies, dislocation energies, etc.

The conclusions most relevant to the initial question posed in the introduction are that for the narrow gap alloys:

- Cd destabilizes the already weak HgTe bond and has little effect on the dislocation energy.
- Zn both stabilizes the HgTe bond and increases the dislocation energy
- Zn also decreases dislocation density of CdTe to improve substrates
- HgZnTe electron and hole mobilities are about the same as those of comparable bandgap HgCdTe.
- HgZnTe is likely to be a superior material to HgCdTe for detectors operating in the 8 - 12 μm regime.

REFERENCES

1. W.A. Harrison, *Electronic Structure and the Properties of Solids* (Freeman, San Francisco, 1980); R.C. Sokel, Thesis, Stanford University (1978); W.A. Harrison, *Microscience*, Vol. 4 (limited-distribution SRI International publication, 1983) p. 34.
2. N.A. Goyunova, A.S. Borshchevskii, and D.N. Fretaiikov, *Semiconductors and Semimetals*, Vol.4, R.L. Willardson and A.C. Beer, eds., (Academic Press, New York) Chapter 1.
3. O. Mukhina, A.M. Gulyaev, A.S. Shnitnikov and I.V. Yamshchikova, *Tr. Mosk. Enprg. In-Ta*, Vol. 443, p. 16 (1980).
4. A.B. Chen, A. Sher, and W.E. Spicer, *J. Vac. Sci Technol*, Vol. A1, p. 1674 (1983).
5. J.C. Mikkelsen, Jr., and J.B. Boyce, *Phys. Rev. Lett.*, Vol. 19, p. 1412 (1982), and private communications.
6. W.E. Spicer, J.A. Silberman, I. Lindau, A.B. Chen, A. Sher, and J.A. Wilson, *J. Vac. Sci. Technol.*, Vol. A1, p. 1735 (1983).
7. J.A. Silberman, D. Laser, I. Landau, and W.E. Spicer "Comparative Study of the Uptake of the Activated Oxygen on HgTe, $\text{Hg}_{0.6}\text{Cd}_{0.4}\text{Te}$ and CdTe," 1984 U.S. Workshop on the Physics and Chemistry of Mercury Cadmium Telluride, San Diego, California.
8. A. Sher, A.B. Chen, and W.E. Spicer, submitted to *J. Appl. Phys.*

9. J.P. Hirth and J. Lothe, *Theory of Dislocations*, 2nd ed. (Wiley, New York, 1982).
10. G. Schoeck and W.A. Tiller, *Phil. Mag.*, Vol. 5, p. 43 (1960).
11. S.L. Bell and M. Sen, "Crystal Growth of $\text{Cd}_{1-x}\text{Zn}_x\text{Te}$ and Its Use as a Superior Substrate for LPE Growth of $\text{Hg}_{0.8}\text{Cd}_{0.2}\text{Te}$," 1984 U.S. Workshop on the Physics and Chemistry of Mercury Cadmium Telluride, San Diego, California.
12. R. Zallen, *Handbook of Semiconductors*, T.S. Moss and W. Paul, eds, Vol. 1 (North Holland Publishing Co., 1982) Ch. 1.

FIGURE CAPTIONS

Fig. 1 Schematic View of Various Bond Configurations.

- (a) A(3)B(1) configuration
- (b) An A(2)B(2) configuration
- (c) An A(3)B(1) configuration embedded in a virtual crystal.

Fig. 2 Bond lengths as a function of concentration x for the $\text{Hg}_{1-x}\text{Cd}_x\text{Te}$ alloy in different configurations.

The short dashed lines are for the CdTe bonds and the long-short dashed lines represent the behavior of the HgTe bonds.

Fig. 3 Bond energy as a function of concentration x for the $\text{Hg}_{1-x}\text{Cd}_x\text{Te}$ alloy in different configurations.

The short dashed lines are for the CdTe bonds and the long-short dashed lines represent the behavior of the HgTe bonds. The solid lines are the concentration weighted averages of the respective bond energies.

Fig. 4 Schematic picture of a potential configuration diagram for the HgTe and CdTe bonds in an Hg(3)Cd(1) configuration.

For the HgTe bond the energy and position of the bond center are calculated by Method 1 of Sec II-B and the final stretched position and energy by Method 2. The results quoted for the CdTe bond are those determined by Method 2

Fig. 5 AC bond energy shifts for the II-VI compounds in A(1)B(3) configurations expressed as a percentage of the pure crystal bond energy.

The B atom is designated in the line that shows the shift. The pure crystal AC bond energies and lengths are given at the top of the figure. These numbers were calculated by Method 1 in Sec. II-B.

Fig. 6 Theoretical versus experimental hardness.

The two values at the top and bottom of the vertical lines designated for each compound were calculated for two different possible dislocation arrangements. The lower one corresponds to the minimum energy configuration and the upper one to a likely higher energy configuration. The experimental numbers were taken from Ref. 2.

Table I

Correlated term values and bond energies
for three II-VI compounds.

The experimental bond lengths, polarity,
and metallic contribution to the bond energy
are also plotted.

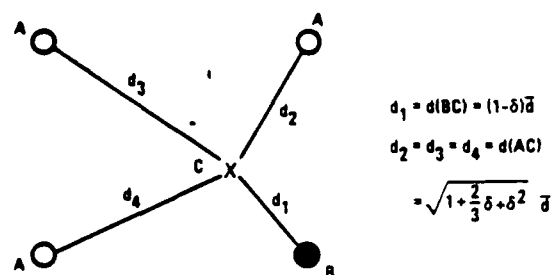
Correlated Term Values [eV]

Atom	s	p	sp ³
Zn	-10.224	-4.920	-6.246
Cd	-9.611	-4.784	-5.991
Hg	-10.946	-4.872	-6.391
Te	-19.620	-9.824	-12.273

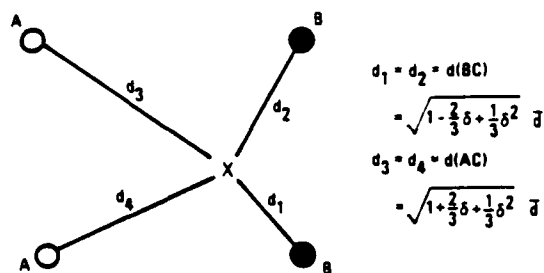
Bond Energies

Compound	d [Å]*	α_p	E_{metallic} [eV]	E_b [eV]
ZnTe	2.643	0.652	-0.625	-0.985
CdTe	2.805	0.710	-0.466	-0.944
HgTe	2.797	0.685	-0.614	-0.480

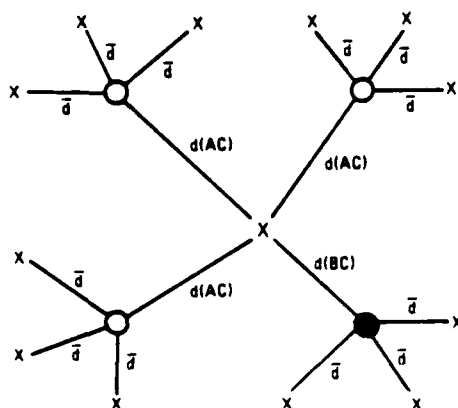
*Ref. 12



(a) A(3)B(1) CONFIGURATION



(b) A(2)B(2) CONFIGURATION



(c) A(3)B(1) EMBEDDED IN A VIRTUAL CRYSTAL

Fig. 1 Schematic View of Various Bond Configurations.

(a) A(3)B(1) configuration

(b) An A(2)B(2) configuration

(c) An A(3)B(1) configuration embedded in a virtual crystal.

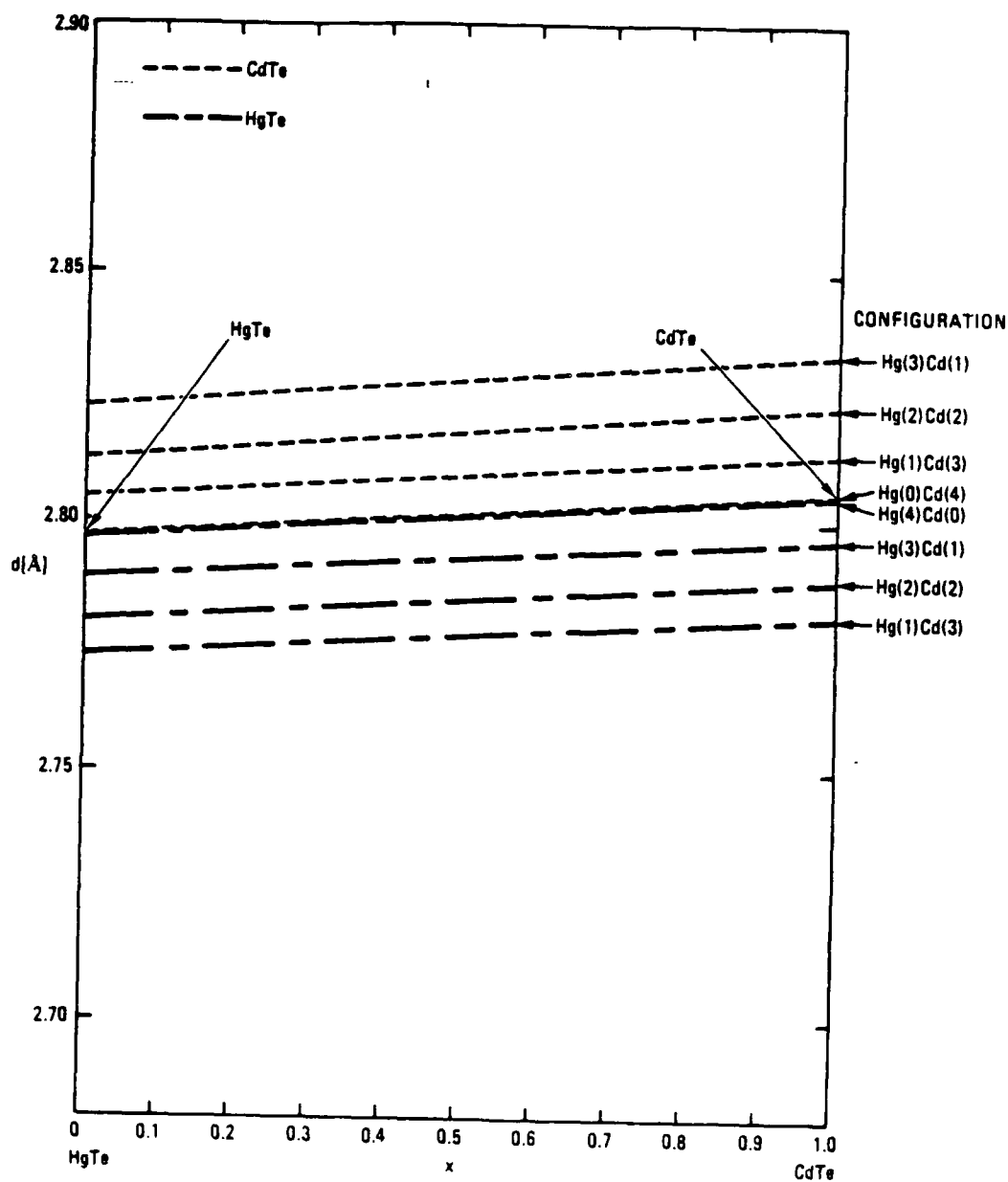


Fig. 2 Bond lengths as a function of concentration x for the $\text{Hg}_{1-x}\text{Cd}_x\text{Te}$ alloy in different configurations

The short dashed lines are for the CdTe bonds and the long-short dashed lines represent the behavior of the HgTe bonds.

orientation, probably lies somewhere between H_{\min} and H_1 . For an indenter with $\vartheta = \pi/4$, we have

$$H_{\min} = 0.0969 \frac{G}{1 - \nu} \quad (11)$$

and $H_1/H_{\min} = 2.39$. Harrison⁹ has shown that one contribution to the shear coefficient (actually $C_{11} - C_{12}$) is

$$G = 2.38 \frac{\hbar^2}{m} \frac{\alpha_c^3}{d^5} \quad \text{joules/m}^3 \quad (12)$$

where \hbar is Planck's constant over 2π , m is the free electron mass $\hbar^2/m = 1.220 \times 10^{-38}$ [joules-m²], α_c is the covalence, $\alpha_c = V_2/(V_{22}^2 + V_{31}^2)^{1/2}$, and d is the bond length. We will approximate G by this expression; however, we also have contributions from C_{44} ($> C_{11} - C_{12}$) for some crystal orientations. C_{44} should have a similar functional dependence on d , but a larger multiplicative constant factor.³ Combining Eqs. (10) and (12), using $\nu = 0.2$, and changing the dimensions to those in terms of which experimental hardness numbers are customarily quoted gives

$$H_{\min} = 2.38 \times 10^4 \frac{\alpha_c^3}{d^5} \quad \text{kgm/mm}^2 \quad (13)$$

where d is in Å. Values calculated from Eq. (13) and H_1 are plotted against experimental results in Fig. 2 for a number of semiconductors

for the minimum-energy configuration and a tetrahedrally bonded semiconductor. Finally, in the indicated configuration,

$$\varphi_{ij} = \varphi = \frac{\pi}{2} - \frac{\vartheta}{2} \quad \text{for all } i, \text{ and } j. \quad (8)$$

Inserting these expressions, Eqs. (5), (6), (7), and (8) into the sums in Eq. (3) and retaining only terms of order N^2 yields

$$H_{\min} = \frac{G \cot \vartheta}{6\pi(1-\nu)} \left[-\ln \left(\frac{\cot \vartheta}{\sqrt{2}} \right) + \frac{4}{3} + \sin^2 \frac{\vartheta}{2} \right] \quad (9)$$

One can also get a number for the hardness of a dislocation configuration in which all the material is pushed along the same glide plane, e.g. to the side, to the bottom, or normal to the face⁸ of the indenter (a possibility not depicted in Fig. 1). In this case, the factor of 2 in front of Eq. (3) is removed, $N = N_h$, and $\varphi = \pi/2 - \vartheta$. Then a higher nonequilibrium hardness in the context of this model (denoted H_1 , is obtained (remember that some terms have been neglected):

$$H_1 = \frac{G \cot \vartheta}{3\pi(1-\nu)} \left[-\ln \left(\frac{\cot \vartheta}{\sqrt{2}} \right) + \frac{4}{3} + \sin^2 \vartheta \right] \quad (10)$$

The proper answer for most materials, and depending on crystal

We now encounter our first surprise. As we can see from Eqs. (4) and (5), the energies per unit length E_{ij} and E_i have comparable magnitudes. Because there are approximately N^2 terms in the interaction energy sum, only N terms in the formation energy sum, and N is a large number ($N \gg 1$), the interaction energy completely dominates the hardness. In fact, N is typically of order 10^5 . Hence, terms owing to screw dislocations, core energies, heat dissipation as the dislocations propagate to their places, and other effects associated with the first term are unimportant. However, care must be taken with the interaction terms: Eq. (3) neglects a number of secondary interactions, some positive and others negative; these will be added later. The principal neglected terms are the interactions between the dislocations in the different regions on each side (positive), and the interactions between adjacent side and bottom regions (positive), and the interaction between the opposite sides in the bottom regions (negative). Comparison of the results with experiment will indicate how important these neglected terms are likely to be. The length L_i is:

$$L_i = W \left(\frac{N-i}{N} \right); \quad i = 1, 2, 3, \dots, N \quad (6)$$

This is the largest length of the side-inserted planes and its choice partially accounts for interactions between the otherwise neglected screw dislocations. The distance $r_{ij} = r_i - r_j$ is given by

$$r_{ij} = 2\sqrt{2b} |i - j|; \quad i, j = 1, 2, 3, \dots, N \quad (7)$$

$$E_i = \frac{Gb^2}{4\pi(1-\nu)} \ln \frac{R}{r_0} \quad , \quad (4)$$

the shear coefficient is G , the Burger's vector $b = d/3$ for an indentation along a $\langle 100 \rangle$ axis, the range of the elastic deformation of a dislocation R is taken equal to W (for want of a better approximation), $r_0 \sim d$ is the dislocation core radius, the Poisson ratio is $\nu \sim 0.2$ for most semiconductors, and L_i is the length of the i th dislocation. In the second term, E_{ij} is the interaction energy per unit length between dislocations i and j , assuming they have parallel glide planes and their Burger's vectors have the same sign. (This neglects terms that will be discussed presently.) The expression for E_{ij} is⁸:

$$E_{ij} = \frac{Gb^2}{2\pi(1-\nu)} \left[\ln(R/r_{ij}) + \cos^2 \varphi_{ij} \right] \quad , \quad (5)$$

where r_{ij} is the separation between dislocation i and j , and φ_{ij} is the angle that a line perpendicular to and joining the dislocations makes with the glide plane, as shown in Fig. 1. Because the various dislocations in a region have different lengths, the net interaction energy is approximated by multiplying the energy per unit length by the length of the shorter one. The one-half multiplying this term prevents double counting and the prime on the sum indicates that terms with $i = j$ are to be omitted. The upper limits on the sums N are the number of dislocations in one region (side or bottom) associated with one edge. For the minimum-energy configuration, $N = N_0/2$. The four that multiplies the bracket accounts for the four sides, and the two for the two regions for each side.

minimum-energy configuration. For the arrangement depicted in Fig. 1, it always costs energy to position a second dislocation on a parallel glide plane to one already present. However, the magnitude of this extra energy can be minimized and, for proper configurations of the dislocations, there are attractive forces along the glide planes that will tend to position the dislocations into the minimum-energy configuration. The minimum configuration arises when half the atoms from the indented volume go respectively to the side and below the indenter. Then, in both regions, the maximum angle made between successive close-spaced dislocation lines and their glide planes is $\varphi = \pi/2 - \vartheta/2$, as shown in the figure. This is the minimum realistic energy configuration. As we shall demonstrate shortly, the minimum-energy configuration is evidently established when soft materials are indented; however, hard ones are more apt to align in a configuration closer to a higher energy configuration where all the atoms go either to the sides or below the indenter. If the dislocations are separated more than shown in Fig. 1, then there is more volume of strained material and the interaction energy would be larger still.

An approximate expression for the energy required to indent the material is⁸:

$$\epsilon_T = 2 \cdot 4 \left[\sum_{i=1}^N E_i L_i + \frac{1}{2} \sum_{i,j=1}^N E_{ij} \{ \min(L_i, L_j) \} \right] \quad (3)$$

In the first term, using an isotropic medium approximation, the energy per unit length to form an edge dislocation is⁸

accommodate an indentation to depth h is

$$N_h = \frac{h}{b} = \frac{W \cot \vartheta}{2b} \quad (2)$$

where ϑ is the angle between the normal to the tip of the indenter and a side. Figure 1 also shows a model of one possible configuration of the dislocations. The edges of the extra atom planes that are driven from the indented volume into the bulk of the semiconductor are shown as lines terminated by dots. The dotted ends of these lines are the positions of the dislocations, which are perpendicular to the plane of the figure. The planes driven to the sides each have a finite extent and a trapezoidal shape. The planes driven down under the indenter have a square shape.

We shall argue that much of the work done on the indenter goes into the energy to form the indicated dislocation configuration, although some certainly goes into heat. There are two major contributions to this formation energy. The first is the energy needed to generate each dislocation as an isolated entity, and the second is the interaction energy among these dislocations.⁸ Because the interaction term dominates H , approximations made to simplify the first term are relatively unimportant. The extra planes driven to the sides of the indentation have a finite extent; accordingly (in this idealized picture), there are both edge dislocations at their base and screw dislocations associated with their termination. The square planes driven below the indentation have edge dislocations around the sides and screw dislocations at the corners to make the turns. Moreover, there are interactions among the dislocations, which can produce a

arising from an integral over the energy of small bond angle distortions distributed over many sites.⁸ The elastic contribution is typically several times larger than the core energy; therefore, we neglect the core terms in this treatment, where the major trends are being sought. The dislocation energy per unit length, E_D is proportional to the product of a shear coefficient and the square of the Burger's vector.⁸ The magnitude of the Burger's vector is proportional to the lattice constant⁸; hence,

$$E_D \propto \frac{V_2^3}{d^3(V_2^2 + V_3^2)^{3/2}}$$

Hardness is determined by applying a known force, F , to a probe of a prescribed shape driving it into the surface of the sample.⁸ The area, A , of the resulting indentation is measured, and the hardness is the force per unit indented area. Many dislocations must be formed to allow the probe to indent the semiconductor. If the indenter is a rectangular pyramid, then the hardness is

$$H = \frac{F}{A} = \frac{Fh}{Ah} = \frac{\epsilon_T}{Ah} \quad (1)$$

where ϵ_T is the work required to cause the indenter to penetrate to a depth h . A side view of the indentation in a cut through its center is illustrated schematically in Fig. 1. The top of the indentation has side length W ; thus, $A = W^2$. The Burger's vector has magnitude b , proportional to the bond length d . The number of dislocations N_h required to

metallic contribution to the bond energy in semiconductors is also bond-angle-dependent³.

The shear coefficients (combinations of C_{44} and $C_{11} - C_{12}$ in the Schoenflies notation)⁸ depend on crystal orientation and (in Harrison's notation⁹) are proportional to $V_2^3/d^5(V_2^2 + V_3^2)^{3/2}$, where $V_2 \propto d^{-2}$ is the covalent and V_3 is the ionic energy. The metallic interaction modifies the functional dependence of the shear coefficient on V_2 and V_3 , but introduces no explicit dependence on the hopping integrals, denoted V_1 by Harrison.^{3,9} The actual independent variables that determine the properties of solids are the valence electron atomic energy levels and wave functions. Although the wave functions are complicated, their essence for treating many bonding properties is captured in the bond lengths. Thus the atomic energies and bond lengths can be used as the effective independent variables of the problem.³ The ionic energy V_3 and the hopping integrals V_1 are functions only of the atomic energies, while the covalent energy V_2 is a function only of the bond length. Thus, in a case where the covalent energy dominates ($V_2 \gg V_3$) the shear coefficients are proportional to d^{-5} ; in the other limit, they are smaller and proportional to d^{-11} . This sharp dependence on bond length results from the fact that the shear coefficients are roughly the covalent bond energy contribution per unit bond volume. In a pure covalent material, the bond energy is proportional to V_2 (or d^{-2}), and the bond volume is $\propto d^3$; hence, in this case, the shear coefficient varies as d^{-5} .

There are two contributions to the dislocation energy per unit length: a short-ranged core energy and an elastic long-range energy

Dislocations in semiconductors are detrimental to device function; they serve as channels for impurity migration and trapping, which causes nonuniform doping and degrades p-n junctions.¹ They also decrease the material's resistance to plastic deformation. The aim of this paper is to provide insights into the underlying physical mechanisms controlling dislocations and semiconductor hardness, and then to suggest strategies for decreasing dislocation densities. It is well-established that the hardness of tetrahedrally coordinated semiconductor materials—Group IV, III-V, and II-VI compounds—exhibits a sharp variation with their near-neighbor distance d , approximately proportional to d^{-9} for one group of seven compounds.² (The lattice constant, a , and d are related by $d = a\sqrt{3}/4$.) Thus, semiconductors with small lattice constants tend to be harder materials. These same materials have larger stiffness coefficients³ and have fewer dislocations in as-grown crystals.⁴⁻⁶ We now interrelate these observations and some other more recent measurements, through an extension of Harrison's theory of the bonding of these semiconductors.³

The major reason for the properties just described can be understood qualitatively as follows. These materials have a low coordination number with only four near neighbors. There are three contributions to their bond energies. The most important one is the covalent energy that results from the interactions between the sp^3 hybrids pointing toward one another on adjacent sites. The strength of this interaction is directionally dependent and energy is required to cause a bond angle distortion. Secondly, the direct ionic contribution to the bond tension is radial (i.e. nondirectional) and adds little to the shear coefficients. Thirdly, the

Section IV-II

DISLOCATION ENERGIES AND HARDNESS OF SEMICONDUCTORS

A. Sher, SRI International, Menlo Park, CA 94025

A.-B. Chen, Auburn University, Auburn, AL 36849

W.E. Spicer, Stanford University, Stanford, CA 95305

ABSTRACT

The dislocation energies and hardness of semiconductors are calculated by an extension of Harrison's method. It is demonstrated in agreement with experiment that dislocation energies per unit length are proportional to d^{-3} to d^{-9} , where d is the bond length, and hardness is proportional to d^{-5} to d^{-11} . The hardness is related to the interaction energies among dislocations. It is argued that dislocation densities of semiconductors will be reduced if they are alloyed with a second constituent that has a shorter bond length. Experimental evidence supporting this strategy is noted.

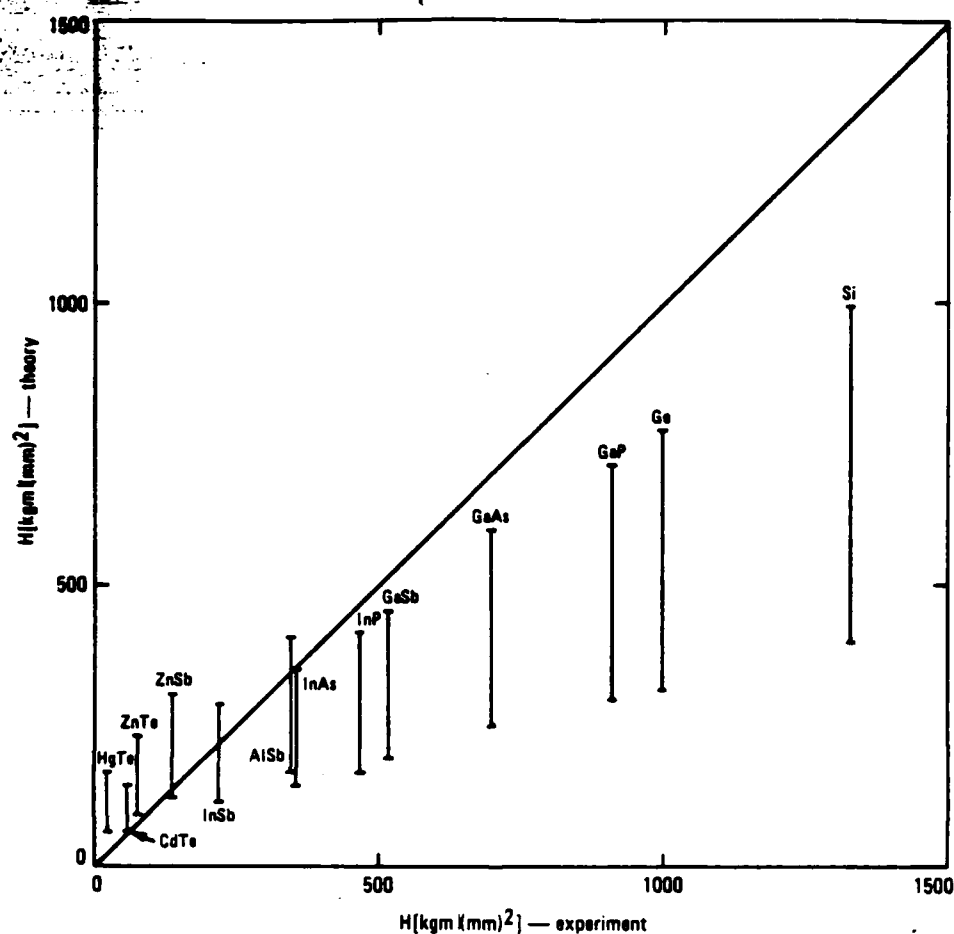


Fig. 6 Theoretical versus experimental hardness.

The two values at the top and bottom of the vertical lines designated for each compound were calculated for two different possible dislocation arrangements. The lower one corresponds to the minimum energy configuration and the upper one to a likely higher energy configuration. The experimental numbers were taken from Ref. 2.

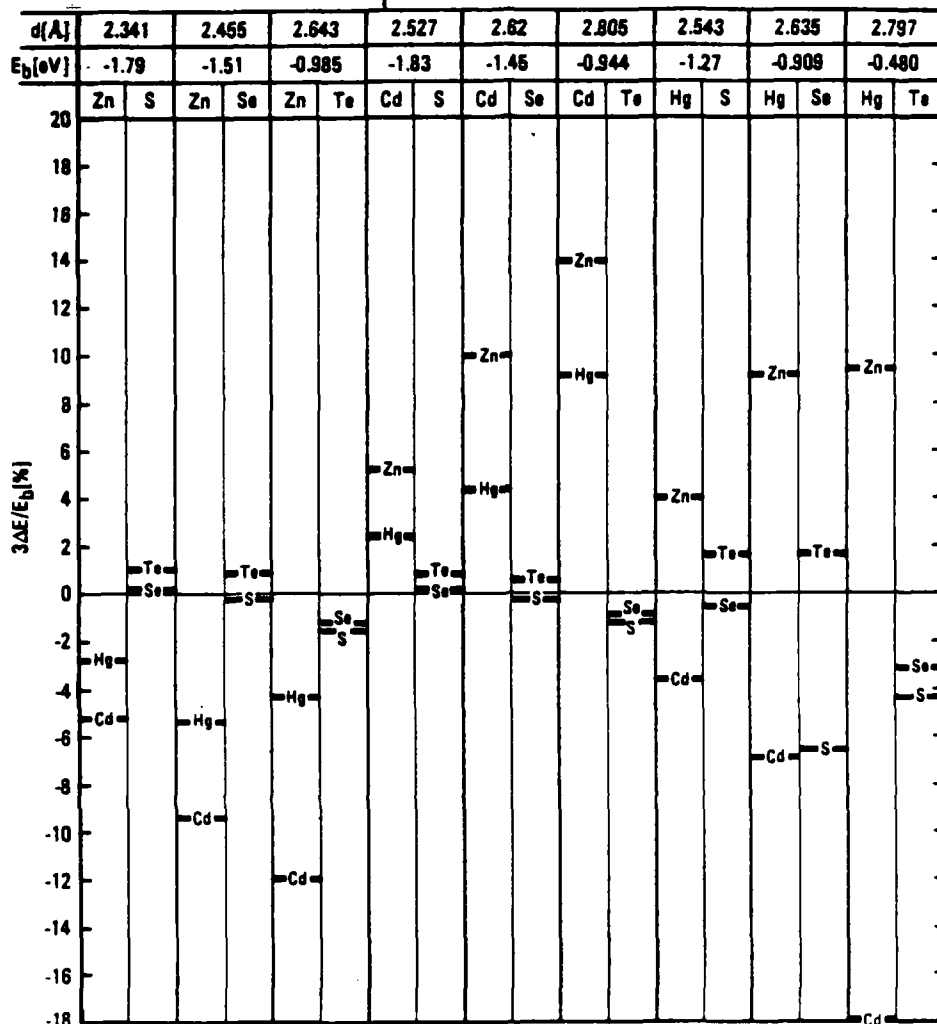


Fig. 5 AC bond energy shifts for the II-VI compounds in A(1)B(3) configurations expressed as a percentage of the pure crystal bond energy.

The B atom is designated in the line that shows the shift. The pure crystal AC bond energies and lengths are given at the top of the figure. These numbers were calculated by Method 1 in Sec. II-B.

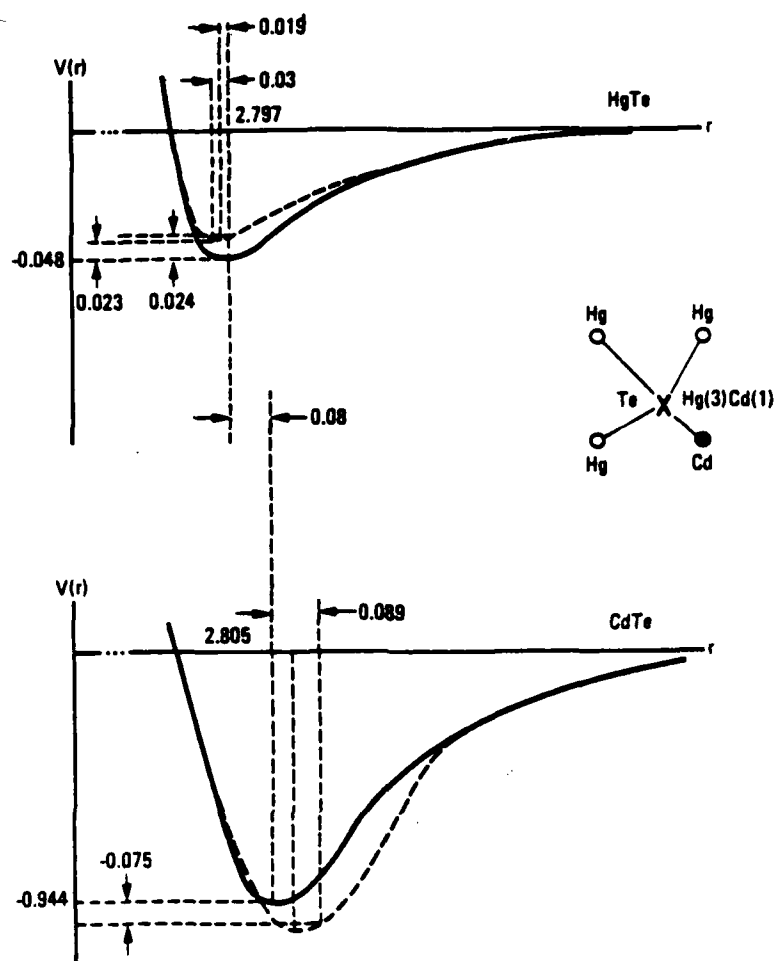


Fig. 4 Schematic picture of a potential configuration diagram for the HgTe and CdTe bonds in an Hg(3)Cd(1) configuration.

For the HgTe bond the energy and position of the bond center are calculated by Method 1 of Sec. II-B and the final stretchal position and energy by Method 2. The results quoted for the CdTe bond are those determined by Method 2.

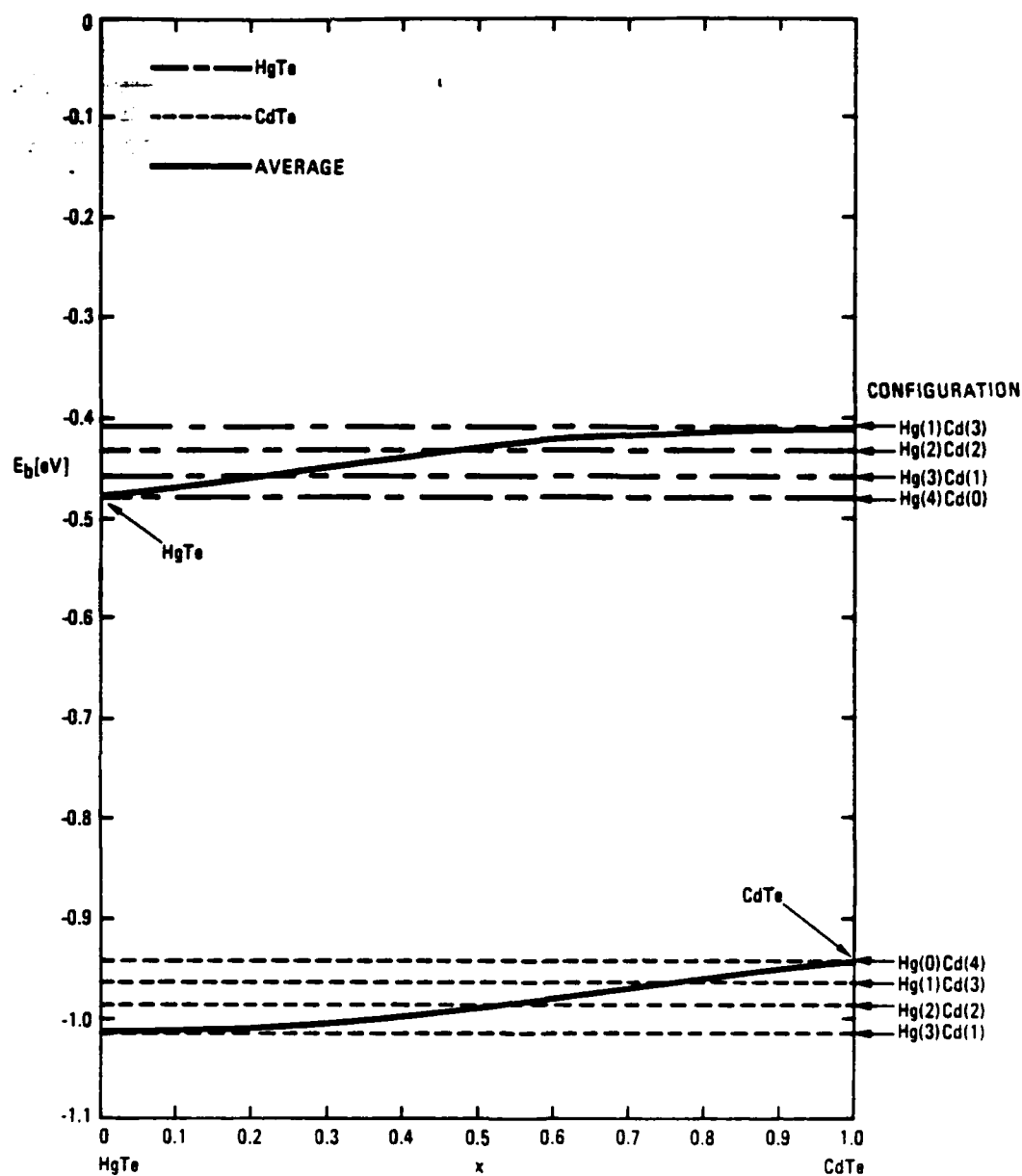


Fig. 3 Bond energy as a function of concentration x for the $\text{Hg}_{1-x}\text{Cd}_x\text{Te}$ alloy in different configurations.

The short dashed lines are for the CdTe bonds and the long-short dashed lines represent the behavior of the HgTe bonds. The solid lines are the concentration weighted averages of the respective bond energies

Figure 2 has the theoretical H_{\min} and H_1 values connected by arrows from H_{\min} to H_1 for each compound, plotted as a function of the corresponding experimental values.^{2,10} If the theory were perfect and the experimental values were accurate, the points would fall on the indicated unity slope line. Several conclusions can be drawn. First, the order of magnitude of the predicted and measured values are the same, a result obtained with no adjustable parameters in the theory. Secondly, the trends from one compound to another are properly given by the theory. Although the H_{\min} values are generally too small, they fit the soft materials better, and the H_1 values fit the harder materials better. As we have pointed out, some terms have been neglected that will very likely increase H_{\min} (and H_1), but they should be smaller than those retained. Thirdly, from Eqs. (1) and (3), H is given in a rough but revealing approximation by $4N^2\bar{E}_{ij}L/Ah$, where the average dislocation length $L = W/2$ and \bar{E}_{ij} is the average dislocation pair interaction energy per unit length. Notice that N (or W) cancels from this expression; thus, H is independent of W (or F) and therefore, H is truly a measure of the properties of the material. This result would not be found if the dislocation energies ($\propto N$) were to dominate H rather than the pair interaction energy ($\propto N^2$). Finally, the Berger's vector cancels from the leading term and appears only in the argument of the logarithm in Eq. (5). Thus, the answers are also insensitive to its choice.

Dislocations are often found in materials as they are grown. Their density is determined by the thermal and mechanical stresses to which they are subjected in the growth process. A dislocation constitutes a metastable excitation relative to the perfect crystal ground state. At the

elevated growth temperatures and temperature gradient behind the growth front, the number of dislocations present is controlled by the relative rate at which vacancies anneal or condense into dislocations.¹¹

The dislocation formation rate will be slower in a material grown at the same temperature if E_D is higher. If an alloy is formed from a material of interest and a second constituent with a shorter bond length, one expects the average bond energy (and thus both the melt temperature and vacancy formation energy) to increase proportional to a low inverse power of the average bond length.⁹ Hence, the equilibrium vacancy density just below the melting point tends to be the same in lowest order for all materials, independent of the bond lengths of the constituents. However, the shear coefficient and dislocation energy per unit length will increase with much higher inverse powers of the bond length. Consequently, dislocation densities should be reduced in such alloys relative to those found in the longer bond length pure constituent. This expectation is confirmed in the recent work reported on $Zn_{1-x}Cd_xTe$ bulk material.⁴ The best CdTe that has ever been grown has dislocation densities in excess of $5 \times 10^5 \text{ cm}^{-2}$. The addition of only 4% Zn reduced the dislocation count to less than $5 \times 10^4 \text{ cm}^{-2}$. The ZnTe bond length is 2.643 Å, while the CdTe bond length is 2.805 Å, a 6% difference. This 6% difference in bond length translates into a 2% difference in the dislocation energy per unit length for $1-x = 0.04$. Dislocation energies per unit length are typically 10 eV per lattice spacing; accordingly, a 2% increase can be expected to slow their formation rate considerably.

The argument just presented naturally leads to a strategy for decreasing dislocations in other semiconductors. If an alloy is made of the material of interest with another compound with a shorter bond length, then the dislocation density should be reduced. For example, this suggests that the addition of a small amount of GaP ($d = 2.359 \text{ \AA}$) may significantly reduce the dislocation density of bulk grown GaAs ($d = 2.448 \text{ \AA}$). It has been demonstrated that the addition of approximately 1% GaN ($d = 1.946 \text{ \AA}$)^{5,6} or of a 10^{18} cm^{-3} BAs ($d = 2.069 \text{ \AA}$) concentration¹² to GaAs can yield a large volume of dislocation-free material. An InAs additive with its longer bond length ($d = 2.623 \text{ \AA}$) serves the same function indirectly, by causing GaAs bonds in its neighborhood to be compressed. This indirect mechanism should be less effective than substituting short-bond-length additives.

We have demonstrated that the dislocation energies and hardness of tetrahedrally bonded semiconductors are rapid functions of the reciprocal of the bond length. This rapid d dependence of dislocation energies provides a rationale for the dramatic decrease of the dislocation density in bulk grown $\text{Zn}_{0.04}\text{Cd}_{0.96}\text{Te}$ material relative to that found in CdTe, and suggest means for accomplishing the same ends in other materials.

Acknowledgments

The authors are indebted to J.P. Hirth, W.A. Harrison, and T.N. Casselman for helpful comments. This work was supported in part by DARPA Contract MDA 903-83-C-0108 and AFOSR Contract 49620-81-K-0012.

REFERENCES

1. E.M. Swiggard, *Proc. GaAs IC Symposium, Phoenix, Arizona* (1983), p. 26.
2. N.A. Groyunova, A.S. Borshchevskii, and D.N. Fretiakov, *Semiconductors and Semimetals*, Vol. 4, R.K. Willardson and A.C. Beer, eds. (Academic Press, New York 1968) Ch. 1.
3. W.A. Harrison, *Electronic Structure and the Properties of Solids* (Freeman, San Francisco, 1980); R.C. Sokel, Thesis, Stanford University, 1978; W.A. Harrison, *Microscience*, Vol. 4 (limited distribution SRI International publication, 1983), p. 34.
4. S.L. Bell and S. Sen, presented at IRIS Detector Specialty Group Meeting, Boulder Colorado, 1983; T.W. James and B.F. Zuck, *ibid*.
5. Y. Seki, H. Watanabe, and J. Matsui, *J. Appl. Phys.*, **42**, 822 (1983).
6. G. Jacob, *J. Crystal Growth*, **59**, 669 (1982).
7. In noncovalent crystals with higher coordination, the ionic contribution to shear coefficients is more important because there are some bond length changes inherent in a shear strain. In metals (usually fcc or bcc structures) with high coordination numbers, the metallic term dominates the shear coefficients.
8. J.W. Christian, *Theory of Transformations in Metals and Alloys*, 2nd Ed. (Pergamon, New York, 1975), Ch. 7. For a discussion of the interaction energies, see J. P. Hirth and J. Lothe, *Theory of*

Dislocations, 2nd ed. (Wiley, New York, 1982), pp. 262-263.

9. W.A. Harrison, *Phys. Rev. B.*, **27**, 3592 (1983).
10. S. Cole and A.F.W. Willoughby, *J. of Crystal Growth*, **59**, 370 (1982).
The HgTe value $H = 26 \text{ kgm/mm}^2$ was taken from this paper.
11. G. Schoeck and W.A. Tiller, *Phil. Mag.*, **5**, 43 (1960).
12. S. Miyazawa, 1983: European Patent Application 833021652, filing date 4/18/83, and references therein.

FIGURE CAPTIONS

Fig. 1 A schematic representation of an idealized minimum-energy dislocation configuration produced by a square-cross-section indenter in a hardness measurement.

W is the side length and h is the depth of the indentation. In this ideal case, half the material from the indented region is displaced along the glide planes (indicated by the dashed arrows) to the sides and half is displaced below the indenter.

Fig. 2 The theoretical vs. experimental^{2,10} hardness of several semiconductors.

The two theoretical values for each semiconductor are connected by an arrow from H_{\min} to H_1 . Perfect agreement would correspond to points being on the unity-slope solid line.

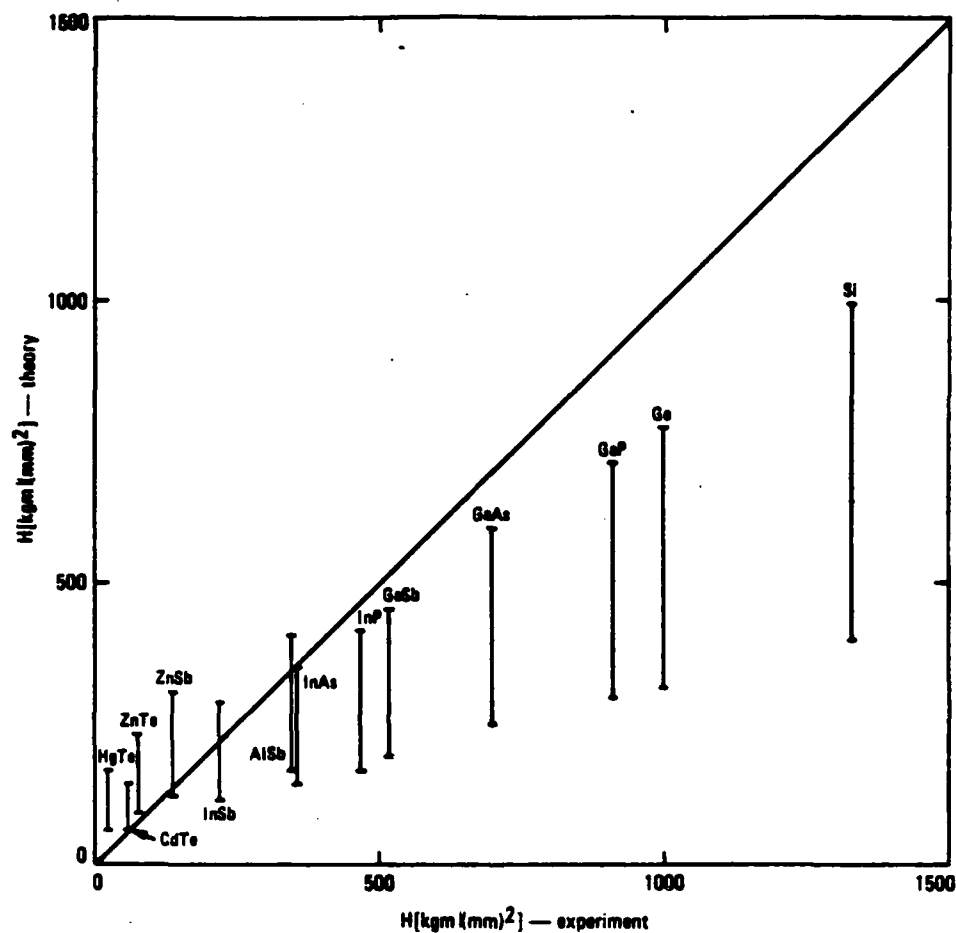


Fig. 2 The theoretical vs. experimental^{2,10} hardness of several semiconductors.

The two theoretical values for each semiconductor are connected by an arrow from H_{min} to H_1 . Perfect agreement would correspond to points being on the unity-slope solid line.



SANTA BARBARA RESEARCH CENTER
a subsidiary

Acknowledgments

We wish to acknowledge many helpful discussions with T.N. Casselman, C.E. Jones and K. Kosai. We especially acknowledge the technical assistance of R.E. Cole and C.R. Curtis for bulk crystal growth and M.S. Langell for wafer preparation and MIS fabrication as well as many helpful comments.

We are also appreciative of the many collaborations which have aided this work, specifically; W.A. Harrison, A.B. Chen, F. Pollak and S. Perkowitz. Finally we are grateful for the support and encouragement of the program sponsor R.A. Reynolds and the technical monitor R.A. Graft.

(This Page Intentionally Left Blank)

END

FILMED

8-85

DTIC